




SPATIAL VARIATIONS OF SEISMIC ATTENUATION IN METROPOLITAN FRANCE FROM OBSERVATION AND MODELING OF THE SEISMIC CODA

| AUTHORS | | | REVIEW | | | APPROVAL | | |
|------------------------------------|------|------|-----------------------|------|------|-------------|------|------|
| NOM | DATE | VISA | NOM | DATE | VISA | NOM | DATE | VISA |
| J. MAYOR (IRAP) | | | T.CAMELBEECK (ORB) | | | P. Traversa | | |
| L. MARGERIN M. CALVET (IRAP) | | | PY. BARD (ISTerre) | | | G. Senfaute | | |

| | | |
|--|--|---|
|  | <p style="text-align: center;">Research and Development Programme on Seismic Ground Motion</p> <p style="text-align: center;">CONFIDENTIAL <i>Restricted to SIGMA scientific partners and members of the consortium, please do not pass around</i></p> | <p>Ref : SIGMA-2014-D2-113 Version : 01</p> <hr/> <p>Date : 2014-06-05 Page :</p> |
|--|--|---|


DISSEMINATION: Authors; Steering Committee; Work Package leaders, Scientific Committee, Archiving.

Executive Summary

This PhD project is an action of SIGMA-WP2 which focuses on predictive models of the ground motion. A number of predictive models are based on so-called Ground Motion Prediction Equations (GMPE) developed empirically with a large dataset of accelerometric waveforms. However, in a region of moderate seismicity like Metropolitan France, the elaboration of GMPE remains difficult because catalogs of strong motion data are incomplete. This deficiency can be partly remedied by combining data from various regions of the world with similar tectonic settings, but at the expense of masking all the small-scale variations of the ground motion within the uncertainties of the model. Stochastic models constitute a viable alternative to GMPE but their predictions are highly dependent on seismic attenuation, which must therefore be determined beforehand. Unfortunately, seismic attenuation is still poorly known in Metropolitan France and a detailed map of its spatial variations is badly needed. There are two main causes for attenuation: absorption (dissipation) and scattering, which have different impacts on the amplitude and duration of the ground motion. Hence, the two broad objectives of the present study are (1) to provide maps of shear wave attenuation in France, (2) to estimate the relative contribution of absorption and scattering to the total attenuation. Absorption and scattering cannot be separated from the analysis of the amplitude of direct S waves only. Therefore, we propose to evaluate seismic attenuation from the modeling of both ballistic and coda waves, with an emphasis on the later.


This report presents both experimental and theoretical results on the attenuation of coda waves in the Alpine range. Various procedures to estimate the coda quality factor (Q_c) are reviewed and compared on real data. A robust experimental procedure to map lateral variations of coda attenuation is presented, and illustrated with preliminary maps which show that the typical scale of the spatial variations of Q_c is of the order of 100 km. This result is a strong argument in favor of rapid lateral variations of attenuation properties in the crust. The maps of Q_c delineate the main geological features such as the Appenines, the Po Valley and the Provence with high attenuation, and the Upper Rhine Graben and eastern Alps with low attenuation. We also present a theoretical study on the sensitivity of coda waves to spatial variations of scattering and absorption properties. These theoretical results will serve as a basis to develop a genuine tomographic approach to map lateral variations of scattering (Q_{sc}) and absorption (Q_i) from seismogram energy envelopes.

The maps of shear wave attenuation that will be delivered at the end of our project will be useful for other actions in WP2 and WP1. In the context of seismic ground motion prediction, attenuation maps may lead to reconsider the classical regionalization approach which is currently based mostly on geological arguments. Moreover GMPE or stochastic prediction models for France, or at regional scale, may be also improved through a better estimation of shear-wave attenuation. For the

| | | |
|--|--|---|
|  | <p style="text-align: center;">Research and Development Programme on Seismic Ground Motion</p> <p style="text-align: center;">CONFIDENTIAL <i>Restricted to SIGMA scientific partners and members of the consortium, please do not pass around</i></p> | <p>Ref : SIGMA-2014-D2-113 Version : 01</p> <hr/> <p>Date : 2014-06-05 Page :</p> |
|--|--|---|


deterministic evaluation of seismic hazard, lateral variations of shear wave attenuation may also be included in direct numerical simulations of the ground motion based on the elastodynamic equation. A better knowledge of the attenuation should also improve the evaluation of the source parameters, as for example the seismic moment and the corner frequency of small earthquakes. Finally, the empirical relations between the magnitude and the macroseismic intensity, used to estimate the magnitude of historical earthquake, may be re-evaluated in the light of a new estimation of the attenuation in France.

DRAFT

| | | |
|--|--|---|
|  | <p style="text-align: center;">Research and Development Programme on Seismic Ground Motion</p> <p style="text-align: center;">CONFIDENTIAL <i>Restricted to SIGMA scientific partners and members of the consortium, please do not pass around</i></p> | <p>Ref : SIGMA-2014-D2-113 Version : 01</p> <hr/> <p>Date : 2014-06-05 Page :</p> |
|--|--|---|

SUMMARY

| | |
|--|-----------|
| Executive summary | 2 |
| 1. Introduction | 5 |
| 1.1 Ground motion attenuation..... | 5 |
| 1.2 Attenuation quality factor..... | 5 |
| 1.3 Seismic coda..... | 6 |
| 1.4 Objectives..... | 7 |
| 2. Measurement of Q_c | 9 |
| 2.1 Methods..... | 9 |
| 2.1.1 Standard method of Aki & Chouet [1975]..... | 9 |
| 2.1.2 Method of Nakahara & Carcolé [2010]..... | 9 |
| 2.1.3 Method of Xie & Nuttli [1988]..... | 14 |
| 2.2 Comparison of the methods..... | 15 |
| 2.3 Conclusion..... | 16 |
| 3. Lateral variations of Q_c | 17 |
| 3.1 Attenuation of crustal phases in France..... | 17 |
| 3.2 Data and networks..... | 19 |
| 3.3 Coda window definition..... | 20 |
| 3.4 Q_c maps..... | 22 |
| 3.5 Conclusion..... | 25 |
| 4. Sensitivity of coda waves to spatial variations of scattering and absorption | 25 |
| 4.1 Observations..... | 25 |
| 4.2 Theory..... | 26 |
| 4.3 Results..... | 29 |
| 4.4 Conclusion..... | 31 |
| Conclusions and Outlook | 33 |
| References | 35 |
| Appendix 1 : Poster presentation at EGU..... | 39 |
| Appendix 2 : Summary of the oral presentation at EGU..... | 40 |
| Appendix 3 : Paper - Mayor et al., [2014]..... | 41 |

| | | |
|--|--|---|
|  | <p style="text-align: center;">Research and Development Programme on Seismic Ground Motion</p> <p style="text-align: center;">CONFIDENTIAL <i>Restricted to SIGMA scientific partners and members of the consortium, please do not pass around</i></p> | <p>Ref : SIGMA-2014-D2-113 Version : 01</p> <hr/> <p>Date : 2014-06-05 Page :</p> |
|--|--|---|

1. Introduction

1.1 Ground motion attenuation

Different contributions control the amplitude of a seismological signal. Signal amplitude can be described as the result of the convolution between a source term, a propagation term and a site response. The propagation term includes (1) geometric effects such as geometrical spreading (focusing/defocusing) or multipathing and (2) attenuation. Attenuation plays an important role in the observed variability of ground motion duration and amplitude. Anelastic and elastic processes, referred to as absorption and scattering respectively, control seismic attenuation but these two processes have distinct impacts on the ground motion. If we consider an absorption anomaly in an otherwise elastic medium, the seismic energy which propagates through this anomaly will be lost resulting in an overall decrease of ground motion amplitudes. By contrast, if we consider a scattering anomaly, the seismic energy which propagates through the anomaly will be redistributed into the medium. This phenomenon will entail a decrease of the direct wave amplitude, accompanied by an increase of the ground motion duration.

Hence, if we are interested in the amplitude and duration of ground motions, it is important to estimate the total seismic attenuation but also to evaluate the relative contribution of scattering and absorption.

1.2 Attenuation quality factor

In seismology, attenuation is usually quantified by a quality factor Q . The amplitude of direct waves filtered in a narrow frequency band decreases with the hypocentral distance r as follows:

$$\exp\left(-\frac{kr}{2Q}\right) \quad (1)$$

where k is the wave number at the central frequency. The attenuation quality factor Q is related to the intrinsic or absorption quality factor Q_i and the scattering quality factor Q_{sc} through the formula:

$$\frac{1}{Q} = \frac{1}{Q_i} + \frac{1}{Q_{sc}} \quad (2)$$

Equation (2) reveals that it is impossible to distinguish between absorption and scattering from the observation of direct waves only. Additionally, even the estimation of the total Q from the amplitude of direct waves requires corrections of source -focal mechanism, magnitude-, path, and site effects, which are difficult to perform in practice. This motivates us to develop alternative approaches to evaluate the attenuation properties of the Earth based on the analysis of coda waves. In the next section we will argue that the analysis of coda waves is a better seismological approach to the evaluation of attenuation properties.

1.3 Seismic coda

S-wave coda refers to the wave trains which follow the direct S-wave, whose average amplitude decreases smoothly with increasing lapse time. After the pioneering study of Aki [1969], it has been widely accepted that coda waves are composed of incoherent waves scattered by distributed heterogeneities in the lithosphere. The most important properties of coda waves, as described in the seminal papers of Aki & Chouet [1975] and Rautian & Kalturin [1978], are briefly summarized hereafter. These authors observed that, contrary to direct S-wave amplitudes, coda envelopes of local earthquakes exhibit a common smooth decay curve with increasing lapse time, irrespective of travel distance. They also observed that the coda decay is independent of the magnitude. Moreover, since coda waves are mostly scattered waves, their take-off angle samples uniformly the sphere of space directions at the source, which explains why the amplitude of coda waves is independent from the focal mechanism. Finally Phillips & Aki [1986], have shown that site effects manifest themselves as an overall increase of coda amplitude but leave no imprint on the coda decay.

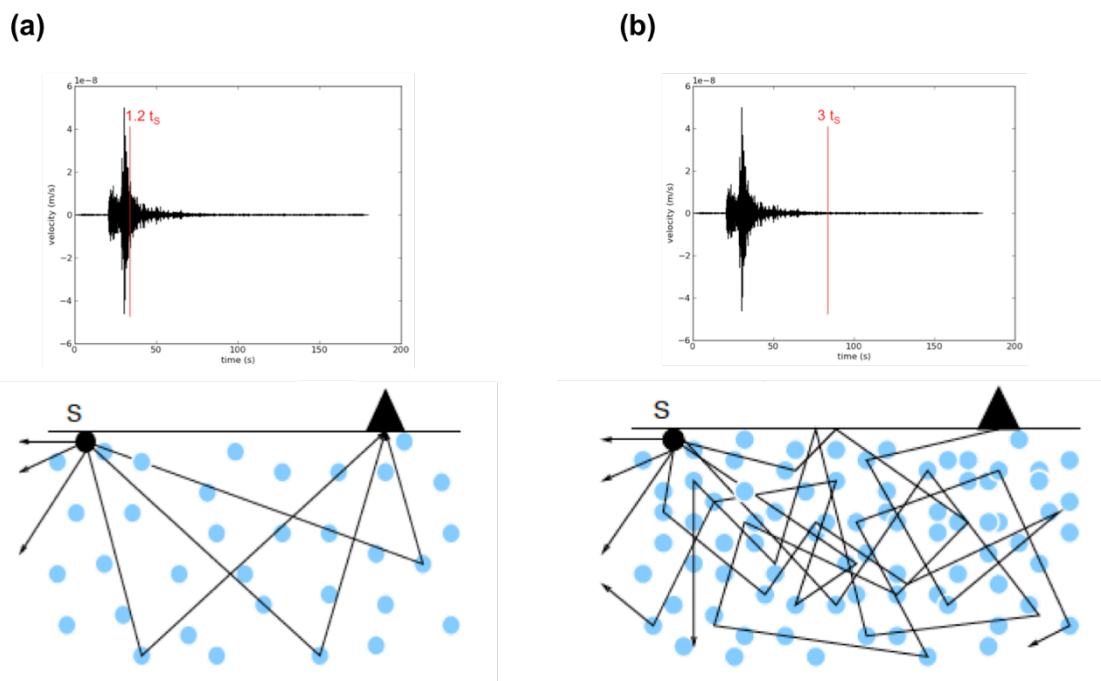



Figure 1: Schematic view of propagation models of coda waves at (a) short lapse time and (b) long lapse time in the coda. Black lines show wave paths between source (black triangle) and receiver (black point). Waves can be scattered off the direct source-receiver trajectory by heterogeneities (blue points) located in the medium.

From these observations, Aki & Chouet [1975] concluded that the decay of the energy in the coda can be conveniently parameterized as follows:

$$E(t, \omega) \propto \frac{1}{t^\alpha} e^{-\frac{\omega t}{Q_c(\omega)}} \quad (3)$$

| | | |
|--|--|---|
|  | <p>Research and Development Programme on Seismic Ground Motion</p> <p>CONFIDENTIAL <i>Restricted to SIGMA scientific partners and members of the consortium, please do not pass around</i></p> | <p>Ref : SIGMA-2014-D2-113 Version : 01</p> <p>Date : 2014-06-05 Page :</p> |
|--|--|---|

where Q_c is the coda quality factor characterizing the coda attenuation, ω is the angular frequency, and t^α is an algebraic term which accounts for the effect of geometric attenuation.

The physical interpretation of Q_c depends on the lapse time. For example, at short lapse time in the coda (when t tends to the S-wave ballistic time t_s), coda waves can be described by the single scattering model [Sato et al., 1977, 2012]. In this model, the coda is composed of waves that have been scattered only once on their way from source to station (Fig. 1.a). This implies that the energy decay in the coda can be expressed as follows [Aki and Chouet, 1975]:

$$E(t, \omega) \propto \frac{1}{t^2} e^{-\omega t \left(\frac{1}{Q_i(\omega)} + \frac{1}{Q_{sc}(\omega)} \right)} \quad (4)$$

Eq. (4) agrees with the parameterization (3) with $\alpha = 2$ and $1/Q_c = 1/Q_i + 1/Q_{sc}$. At long lapse time ($t \rightarrow +\infty$), coda waves are composed of multiply-scattered waves and enter in the diffusive regime as illustrated in Figure 1.b. In the diffusive regime, the decay of the energy in the coda can be expressed as:

$$E(t, \omega) \propto \frac{1}{t^{3/2}} e^{-\frac{\omega t}{Q_i(\omega)}} \quad (5)$$

which agrees with the parameterization (3) with $\alpha = 3/2$ and $Q_c = Q_i$. From this simple analysis, we conclude that, depending on the lapse time, coda waves are sensitive to both scattering and absorption (short lapse-time), or to absorption only (long lapse-time). This in turn implies that the effects of scattering and absorption can be easily separated through a lapse-time analysis of the coda decay. However the applicability of the single-scattering and diffusion models to real data is rather limited [Gusev & Abubakirov 1987; Hoshiya, 1991] and a more rigorous multiple-scattering approach is necessary, [Felher et al., 1992; Hoshiya, 1993]. Besides multiple-scattering effects, scattering anisotropy is yet another factor controlling the shape of the coda, in particular at short lapse-time [Hoshiya, 1995; Gusev & Abubakirov, 1996]. Calvet & Margerin [2013] argue that scattering anisotropy is responsible for most of the observed lapse-time dependence of Q_c reported in the literature, and confirm that the decay of the late coda is mostly sensitive to intrinsic attenuation. Their conclusions are summarized in Figure 2.

In conclusion, while effects of scattering and absorption can in principle be distinguished from a lapse-time analysis of coda waves, the early coda is sensitive to fine details of the medium and requires a detailed physical model incorporating scattering anisotropy. Therefore, in the first part of this work, we focus on the analysis of the late part of the coda.

1.4 Objectives

The two broad objectives of my thesis are as follows:

- (1) To provide maps of the attenuation quality factor of shear waves (Q) in France in the high-frequency band (>1 Hz).

(2) To estimate the contribution of intrinsic and scattering attenuation (Q_i and Q_{sc}) to the total quality factor.

Following the discussion 1.3, we adopt a two-step approach: (1) estimate Q_i from the rate of decay of the late coda and (2) estimate Q_{sc} from the early coda, after correcting for the effects of intrinsic attenuation and scattering anisotropy. Scattering anisotropy will be estimated based on the work of Calvet and Margerin [2013].

The report is organized as follows: in section 2, we compare three methods of estimation of Q_c found in the literature and discuss their advantages/disadvantages. In section 3, we present a method to map lateral variations of coda wave attenuation, with application to the French Alps and surrounding regions. We present maps of Q_c in four frequency bands ranging from 1 to 16 Hz, which reveal clear lateral variations of coda wave attenuation. In section 4, we develop a physical model of multiply-scattered waves which allows us to interpret the spatial variations of coda wave attenuation in terms of spatial variations of attenuation properties (Q_i , Q_{sc}).

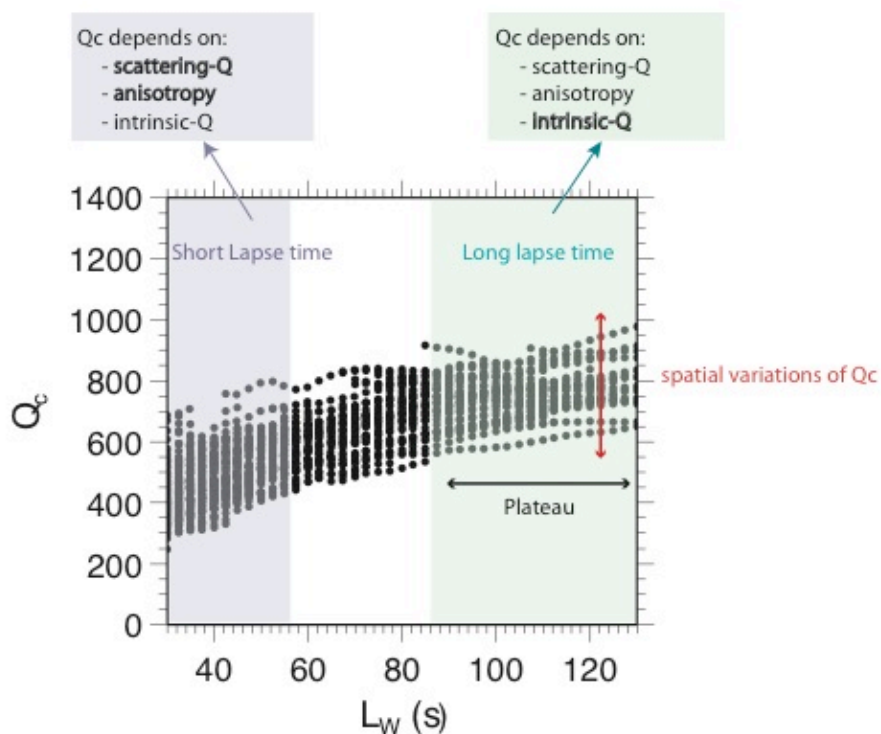



Figure 2: Q_c as a function of coda window duration L_w in the 4-8 Hz frequency band. The estimation of Q_c has been performed in the 50-80 km epicentral distance range in the Pyrenees. We observe a transient increase of Q_c with lapse time followed by a stabilization around a plateau (black arrow) whose average is about 800. The fluctuations of Q_c around the mean plateau value (red arrow) reflect the spatial variations. At short lapse time (purple area), Q_c is predominantly sensitive to scattering and anisotropy while at long lapse time (green area) Q_c mainly depends on intrinsic absorption [Calvet et Margerin, 2013].

| | | |
|--|--|---|
|  | <p style="text-align: center;">Research and Development Programme on Seismic Ground Motion</p> <p style="text-align: center;">CONFIDENTIAL <i>Restricted to SIGMA scientific partners and members of the consortium, please do not pass around</i></p> | <p>Ref : SIGMA-2014-D2-113 Version : 01</p> <hr/> <p>Date : 2014-06-05 Page :</p> |
|--|--|---|

2. Measurement of Q_c

In this section, we propose to study three different classical methods of estimation of the coda quality factor Q_c . The techniques differ in their domain of analysis (spectral or temporal) and in their statistical assumptions on the fluctuations of coda envelope. The estimates of Q_c obtained for four seismograms recorded in the Alps will be compared and discussed.

2.1 Methods

To facilitate the comparison of the three methods, we present the main steps of the signal processing using a sample seismogram recorded in the Alps. The magnitude of the earthquake is 3.6 and the epicentral distance is 50 km. Q_c is estimated on a coda window with onset time $t_w=70$ s and duration $L_w=50$ s.


The first step of the signal processing is common to the three methods and consists in deconvolving the waveform from the station response. Acceleration and displacement data are converted to velocities. The parameters α and Q_c of equation 3 cannot be estimated independently [Rautian & Kalturin, 1978]. Hence, the three methods require that the coda decay be corrected from the algebraic term t^α in equation 3 where the value of the exponent α must be fixed a priori. Because the role of multiple scattering becomes more pronounced as the lapse time increases, we take $\alpha=3/2$, which physically corresponds to a diffusion process in 3-D space.

2.1.1 Standard method of Aki & Chouet [1975]

The data are filtered in four frequency bands [1-2], [2-4], [4-8] and [8-16] Hz (Fig. 3.a). On the filtered waveform, we define the noise level as the average of the squared velocity in a window of 10 seconds duration starting at the beginning of the record. The noise window is free from any P-wave arrival thanks to a STA/LTA detection. The intensity envelop of the signal $E(t,\omega)$ is defined as the squared velocities. To smooth the intensity fluctuations, we apply a moving average window whose typical duration is of the order of 16 cycles (Fig. 3.b). The smoothed intensity envelop is corrected from the algebraic term $t^{-3/2}$ of equation 3 (Fig. 3.c). In each frequency band, a least-squares linear fit of the logarithm of $E(t,\omega)t^{3/2}$ as a function of time yields an estimate of Q_c (Fig. 3.c). The resulting value of Q_c is accepted when (1) the correlation coefficient of the linear regression is greater than 0.7 and (2) the signal to noise (SN) ratio over the entire duration L_w of the coda window is greater than 4. In this least-squares approach, it is implicit that the fluctuations of the smoothed intensity obey Gaussian statistics. This may not be the case in practice and the method we present next takes explicitly into account the statistical fluctuations of the envelope.

2.1.2 Method of Nakahara & Carcolé [2010]

The method developed by Nakahara & Carcolé [2010] is also based on a time-frequency analysis and assumes a more flexible statistical distribution of fluctuations of the coda envelope. Recently, it was found that the random fluctuations of high-frequency seismogram envelopes follow the Nakagami-m distribution [Carcolé & Sato, 2009], where the probability density function p is given by:

| | | |
|--|--|--|
|  | Research and Development Programme on Seismic Ground Motion CONFIDENTIAL <i>Restricted to SIGMA scientific partners and members of the consortium, please do not pass around</i> | Ref : SIGMA-2014-D2-113 Version : 01 Date : 2014-06-05 Page : |
|--|--|--|

$$p(r(t)) = \frac{2m^m}{E(t, \omega)^m \Gamma(m)} r^{2m-1} e^{-\frac{m}{E(t, \omega)} r^2} \quad (6)$$

where Γ is the gamma function, $E(t, \omega)$ is the intensity in the coda at time t and frequency ω , m is the Nakagami- m parameter and $r(t)$ is the analytic signal calculated from the original time series $u(t)$ and its Hilbert transform $H[u(t)]$ as follows:

$$r(t) = \sqrt{u(t)^2 + H[u(t)]^2} \quad (7)$$

Equation 6 shows that the Nakagami- m distribution depends on two parameters: (1) the m -parameter which defines the shape of the distribution and (2) the intensity envelop $E(t, \omega)$ parameterized following equation 3. By varying m from 0 to infinity, the Nakagami- m distribution is able to express different kinds of standard distributions. For example, $m=0.5$ describes a half-Gaussian distribution and $m=1$ matches a Rayleigh distribution. Moreover, Nakagami [1960] has shown that m is inversely proportional to the variance of r^2 . Therefore, m is an indication of fluctuations in the envelop: for larger fluctuations m becomes smaller and vice versa.

In the method of Nakahara & Carcolé [2010], $E(t, \omega)$ depends on two parameters: (1) a constant γ controlling the overall amplitude of the coda and (2) the coda quality factor Q_c :

$$E(t, f) = \gamma t^{-\alpha} \exp\left(-\frac{\omega}{Q_c} t\right) \quad (8)$$

Note that α is fixed a priori ($\alpha=3/2$).

Nakahara & Carcolé [2010] have derived a Maximum Likelihood (ML) method to simultaneously estimate the m -parameter and Q_c . They have introduced a log-likelihood function ($\log L$) assuming that the n sampled amplitudes of the analytic signal at time t_i ($i=1, \dots, n$) are mutually independent:

$$\log L \equiv \sum_{i=1}^n \log p[r(t_i)] \quad (9)$$

The parameters γ and Q_c controlling $E(t, \omega)$, and m , are estimated by finding the extrema of the log-likelihood function in the (Q_c, γ, m) space. The main steps of the data processing are summarized in figure 4. First, the data are filtered in the same four frequency bands as in the Aki & Chouet [1975] method. Next, the analytic signals are computed following equation 7 (Fig. 4.a). From the whole coda window ($t_w=70s$, $L_w=50s$), we have estimated the statistical m -parameter (Fig. 4.b) and the coda envelop parameters γ and Q_c with the ML method (eq. 9). The extremum of equation 9 was numerically found by using a bisection method, assuming that m ranges from 0.1 to 5 and that ω/Q_c ranges from 0 to 1.7. The lower and upper limits of m and ω/Q_c have been determined empirically by testing a large dataset and assuming that negative coda- Q is not physically reasonable. The extracted coda envelop $E(t, \omega)$ is shown in figure 4.c.

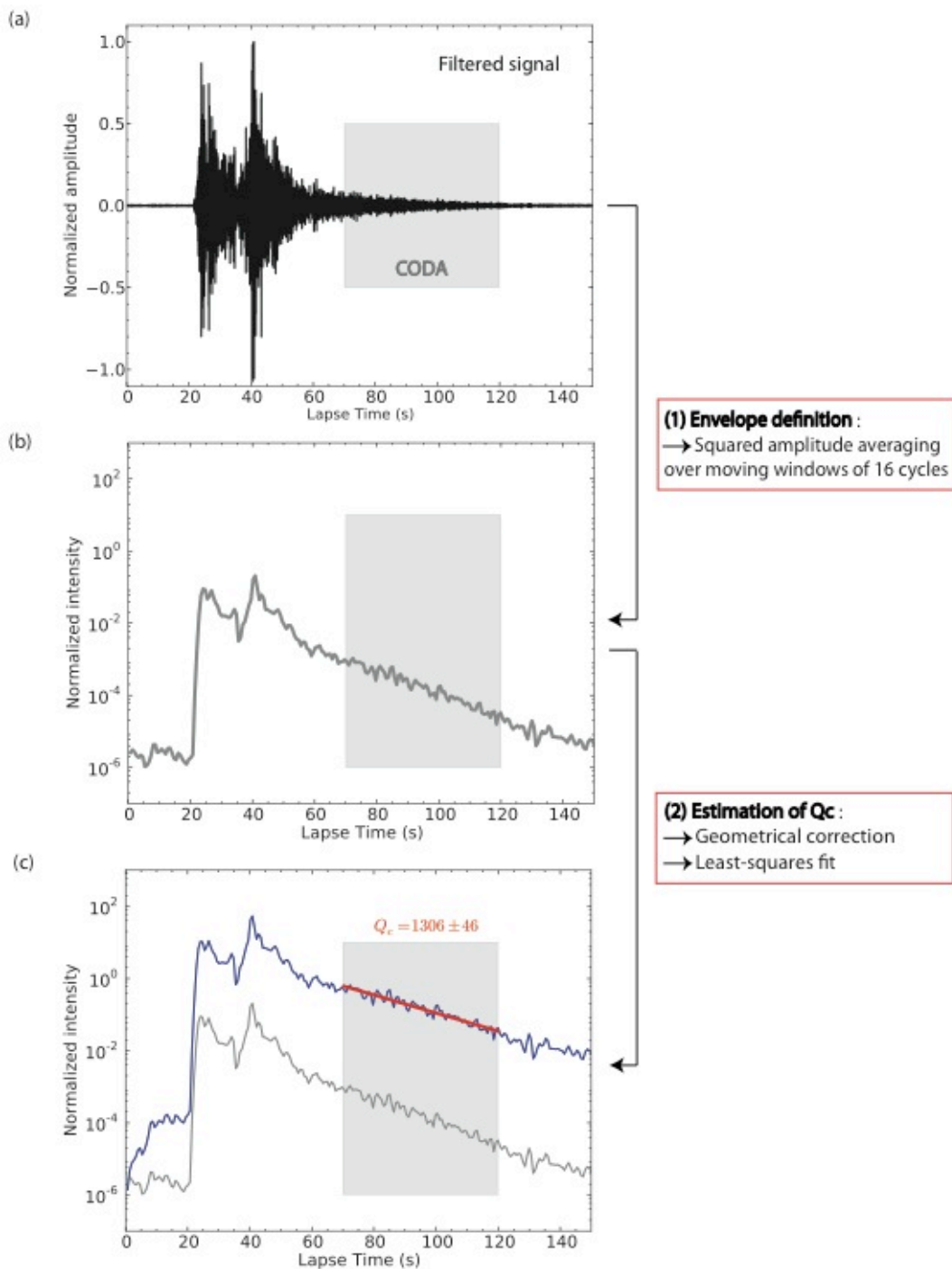


Figure 3: Illustration of the signal processing technique developed by Aki & Chouet [1975] to estimate Q_c in the 8-16 Hz frequency band. (a) Normalized vertical velocities as a function of time. The gray area indicates the coda window is indicated by a gray rectangle. (b) Normalized intensity of the seismogram as a function of lapse time. The intensities are obtained by averaging the squared velocities in a moving window of duration 16 cycles. (c) Estimation of Q_c by linear regression: the blue curve indicates the normalized smoothed intensity corrected from the geometrical term ($t^{3/2}$) as a function of lapse time. The red line shows the result of the least squares fit.

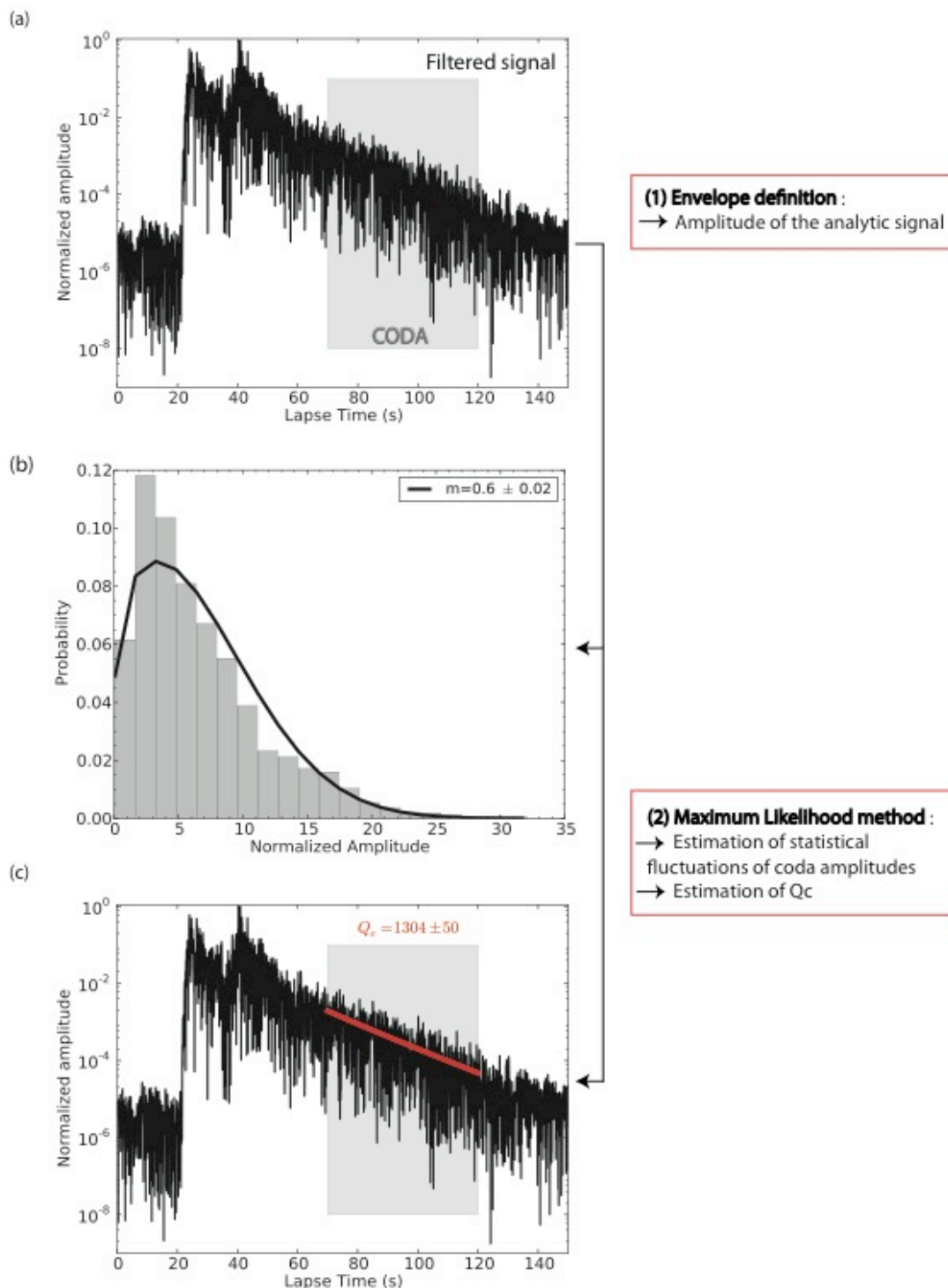


Figure 4: Illustration of the signal processing technique developed by Nakahara & Carcolé [2010] to estimate Q_c in the 8-16 Hz frequency band. **(a)** Normalized amplitude of the analytic signal as a function of time. The coda window is indicated by a gray area. **(b)** Probability distribution of the normalized amplitude ($A/\langle A^2 \rangle$) of the analytic signal in the coda window. The black line shows the probability density function of Nakagami for $m=0.6$, where m has been estimated with a ML method (see text). **(c)** Normalized amplitude of the analytic signal as a function of lapse time. Red line shows the estimated coda decay based on the ML method (see text).

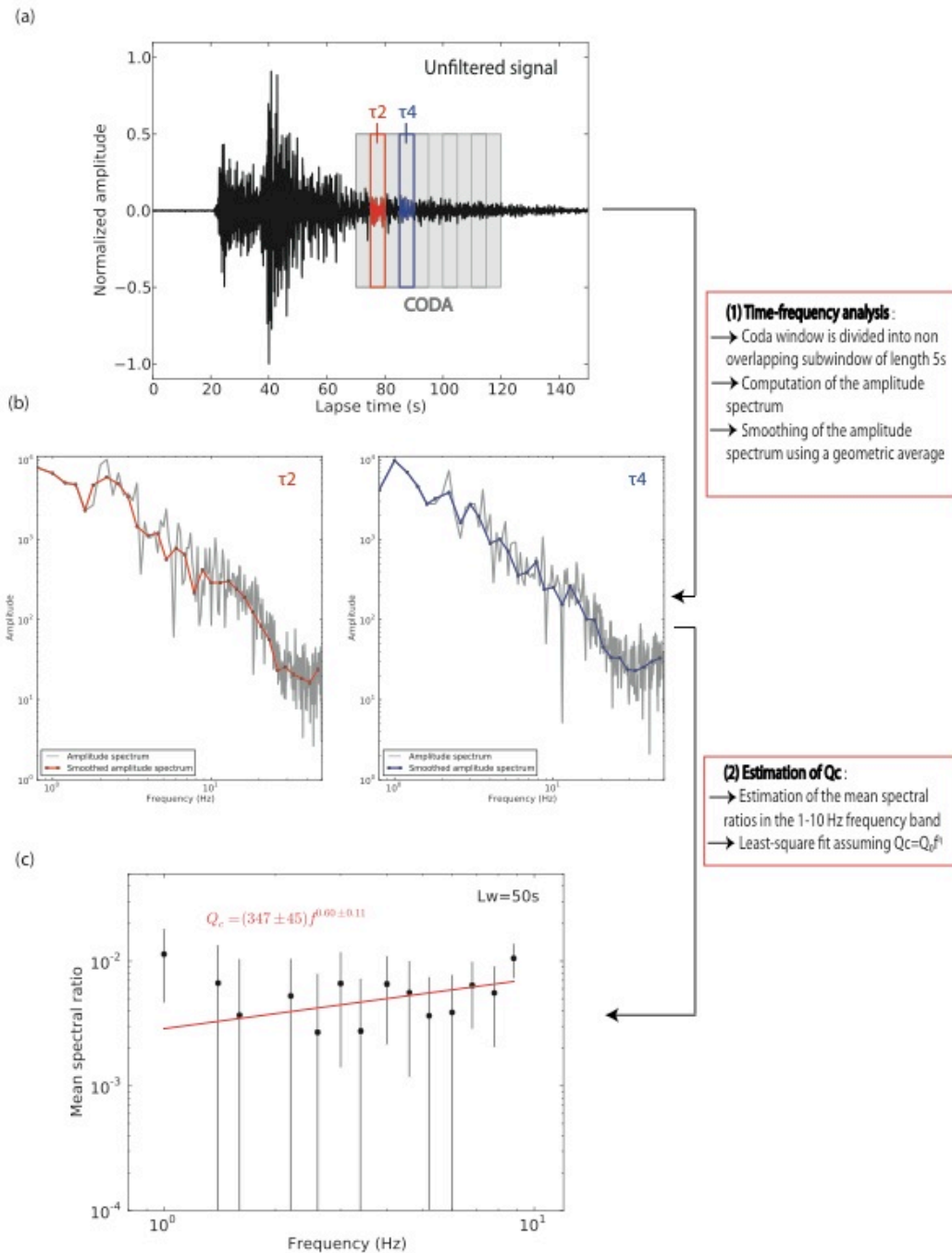



Figure 5: Illustration of the signal processing technique developed by Xie & Nuttli [1988] to estimate Q_c . **(a)** Normalized unfiltered vertical velocity as a function of time. The coda window (gray area) is divided into ten subwindows of length 5 seconds, with central time τ_i , where i is the subwindow index. **(b)** Plot of the amplitude spectra for two subwindows of central time τ_2 (left) and τ_4 (right) respectively. Each amplitude spectrum is subsequently smoothed by computing the geometric average in logarithmically spaced frequency windows (red and blue curves). **(c)** Mean spectral ratio $\langle A(\tau_i)/A(\tau_{i+2}) \rangle_i$ as a function of frequency. $\langle \rangle_i$ indicates an average over all possible time windows. The parameters (Q_0/η) of the power law $Q_c = Q_0/\eta^i$ are determined from a least squares fit of the frequency dependent amplitude spectral ratio.

| | | |
|--|--|---|
|  | <p>Research and Development Programme on Seismic Ground Motion</p> <p>CONFIDENTIAL <i>Restricted to SIGMA scientific partners and members of the consortium, please do not pass around</i></p> | <p>Ref : SIGMA-2014-D2-113 Version : 01</p> <hr/> <p>Date : 2014-06-05 Page :</p> |
|--|--|---|

2.1.3 Method of Xie and Nuttli [1988]

Adopting a different point of view, Xie & Nuttli [1988] propose to estimate Q_c with a spectral method. Their data processing technique has been developed for the estimation of the coda quality factor of Lg waves and has been adapted to our needs. Compared to the two previous methods, Xie & Nuttli [1988] make the following assumption on the frequency dependence of Q_c :

$$Q_c = Q_0 f^\eta \quad (10)$$

The purpose of the method developed by Xie & Nuttli [1988] is to retrieve the parameters Q_0 and η of the power law (10). Note that when the data deviate strongly from the power law (10), it has an impact on the estimate of Q_c at all frequencies, which is a drawback of this approach. The main steps of the method are illustrated in Figure 5.

First, we divide the coda window of duration $L_w=50s$ into non overlapping subwindows of length 5 seconds. Note that this procedure applies to the *unfiltered* time series. Each of the ten resulting subwindow is characterized by a central time τ_i , where i is the index of the subwindow (Fig. 5.a). Using a Fast Fourier Transform, we compute the amplitude spectrum for each subwindow, after application of a cosine taper of width 10%. Following the work of Aki & Chouet [1975] and the assumption (10), the amplitude spectrum for a given subwindow A_i can be expressed as follows:

$$A_i \propto \tau_i^{\alpha/2} \exp\left(-\frac{\pi f^{1-\eta} \tau_i}{Q_0}\right) \quad (11)$$

Note that the geometrical exponent α is divided by 2 compared to the method of Aki & Chouet [1975] because we consider amplitudes. The amplitude spectrum in each subwindow is subsequently smoothed by computing a geometric average in logarithmically spaced frequency windows. The resulting smoothed amplitude spectrum is denoted by $\langle A \rangle_i$. Two examples of smoothed amplitude spectra for subwindows 2 and 4, are shown in figure 5.b. Next, we define the scaled logarithmic ratio of the smoothed amplitude spectra R as follows:

$$R_{i,N_r+i} = \frac{1}{\tau_{i+1} - \tau_i} \log \frac{\tau_{i+1}^{\alpha/2} \langle A \rangle_i}{\tau_i^{\alpha/2} \langle A \rangle_{N_r+i}} \quad (12)$$

where N_r is half the number of subwindows. Note that the frequency dependence of the amplitude spectrum ratio R_i is implicit in equation 12. As shown by Xie & Nuttli [1988], the definition of the smoothed spectral amplitude in equation 12 implies that its probability density function is of Rayleigh type. To reduce the fluctuations, the quantity R_i is averaged over all possible pairs of subwindows:

$$F = \frac{1}{N_r} \sum_{i=1}^{N_r} R_{i,N_r+i} \quad (13)$$

with $N_r=5$ in our case. The parameters Q_0 and η of the power law (10) may be estimated by taking the logarithm of equation 13:

$$\log_{10} F = (1 - \eta) \log_{10} f - \log_{10} Q_0 \quad (14)$$

and by applying a simple least-squares linear regression in the log-frequency domain. The estimated frequency dependence of Q_c is shown in figure 5.c together with the original data. We observe that the power law (10) applies in the 1-10 Hz frequency band only.

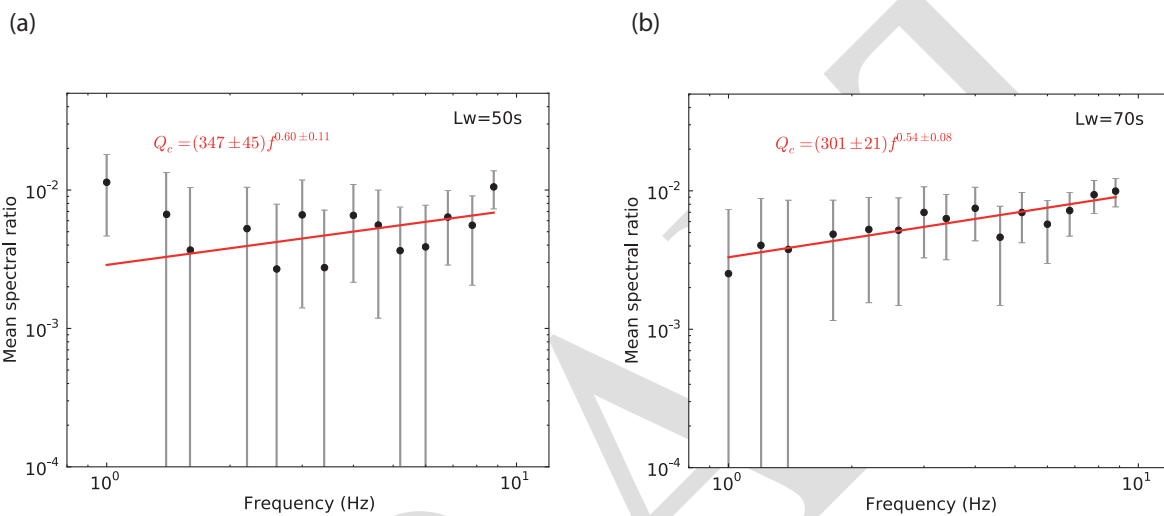


Figure 6: Mean spectral ratio as a function of frequency computed for (a) $L_w=50s$ and (b) $L_w=70s$. The red lines show the resulting least squares fit.

As seen previously, the technique of Xie & Nuttli [1988] has been developed for Lg-coda waves which usually have a long coda duration, typically of the order of 200s. To test the robustness of the method, we have applied the method to a longer coda of duration $L_w=70s$. Note that the value of L_w cannot be greater than 70s because most earthquakes of our dataset have relatively small magnitudes. A comparison of the estimate of Q_c for $L_w=50s$ and $L_w=70s$ is shown in figure 6. We observe that the data variance is reduced and that the power-law (10) is better verified in the frequency range of interest. In particular the correlation coefficient of the linear regression in the log-frequency domain increases from $R^2=0.7$ to $R^2=0.87$. In addition, the uncertainties associated to Q_0 and η are also reduced by nearly a factor of 2. This result suggests that the method of Xie and Nuttli [1988] is much better suited to Lg codas of long duration, than to short codas of local earthquakes.

2.2 Comparison of the methods

We propose to briefly compare between the results of the three methods in the 8-16 Hz frequency band. We select four earthquakes with epicentral distances of about 50 km and magnitudes in the range 3.1-3.6. The criterion used to select the record is a long coda duration with

high signal to noise ratio, so that the comparison is not hampered by the noise level. We also make sure that the coda is not contaminated by undesired signals such as aftershocks or storms. The signals were recorded in the Alps on the SismAlp network. Figure 7 shows a comparison between the estimates of Q_c with uncertainties, for coda windows of duration $L_w=50s$ (Fig. 7.a), and $L_w=70s$ (Fig. 7.b).

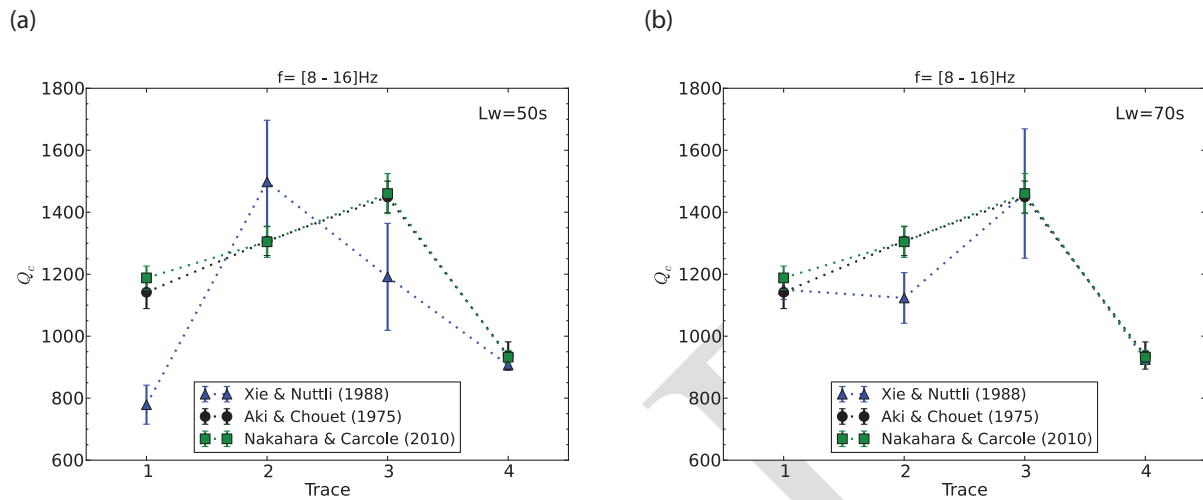


Figure 7: Comparison of Q_c measurements for four seismograms recorded in the Alps with coda window duration $L_w = 50s$ (a), and $L_w=70s$ (b). The estimations of Q_c have been performed with the three methods described in the text and are denoted by different coloured symbols (see the legend in inset).

For the shortest coda duration, we observe that the estimates of Q_c obtained by the Aki & Chouet [1975] and Nakahara & Carcolé [2010] methods are in very good agreement, well within the uncertainties. By contrast, the results of the method of Xie & Nuttli [1988] differ by about $\pm 20\%$ from previous two. This tendency is reduced when we consider a longer coda duration (Fig. 7.b).

2.3. Conclusion

From the comparison between the three methods of Q_c estimation presented in this section, we can draw two conclusions:

- (3) The method of Xie & Nuttli [1988] has two main problems: its strong assumption on the frequency dependence of Q_c (Eq. 10) and its lack of robustness for short coda durations (Fig. 7) typical of our dataset ($L_w < 100s$).
- (4) Even if the method of Nakahara & Carcolé [2010] takes into account explicitly the details of the statistical fluctuations of the coda envelope, its results are nearly identical to those obtained by the technique of Aki & Chouet [1975].

We are thus confident in the simple but well adapted technique of Aki & Chouet [1975] to estimate the S-coda quality factor. However, we will probably make use of the method of Xie & Nuttli [1988] at a later stage of this project, since we plan to analyze Lg-codas to map the attenuation in areas of low seismic activity.

3. Lateral variations of Q_c

In this section, after briefly reviewing the existing maps of attenuation for Metropolitan France as a whole, we will focus on the French alpine range and its surrounding regions. Because Q_c is lapse time dependent [Calvet & Margerin, 2013], we will discuss in some details the optimal choice of epicentral distance Δ and coda window parameters (t_w , L_w) to avoid biases in the mapping procedure. Finally, we will present and discuss frequency-dependent maps of Q_c for the Alps.

3.1 Attenuation of crustal phases in France

Nicolas et al. [1982] were the first to study the attenuation of crustal phases at regional distances – in particular L_g waves – in Metropolitan France. Using a simple linear regression of the log-Amplitude of band-passed filtered signals as a function of epicentral distance, they were able to identify low- Q regions in Eastern France (Rhône Valley and Ivrea Zone). Their study reveals that L_g waves are strongly attenuated (low Q value) when propagating through the Rhone Valley or the Ivrea Zone in southeast of France.

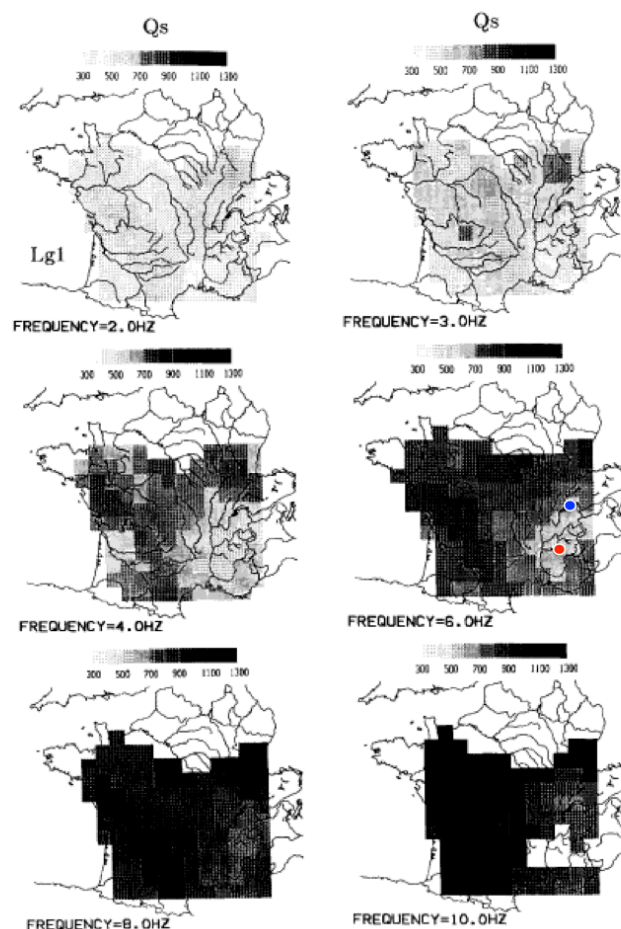


Figure 8: Spatial variations of the apparent attenuation of S waves in the French crust at six frequencies ranging from 2 to 10 Hz [Campillo & Plantet, 1991]. On the attenuation map at 6 Hz, the blue and red points indicate the station locations for the blue and red records shown in Figure 9.

Using a larger dataset, Campillo & Plantet [1991] have obtained the first frequency-dependent maps of attenuation with good spatial coverage for France. They have developed an inversion scheme based on a starting model with homogeneous quality factor of S-wave Q_s , estimated with the method of Xie & Nuttli [1988] (see section 2). The starting model is subsequently refined on a regular grid which yields a continuous distribution of the apparent attenuation of Lg waves [Campillo et al., 1985 and Campillo & Plantet, 1991]. The resulting attenuation maps are shown in figure 8 in six narrow frequency bands ranging from 2 to 10 Hz. At frequencies higher than 4 Hz, the maps of Q_s exhibit a high attenuating area in southeastern France also revealed by Nicolas et al. [1982]. However, except for this highly attenuating zone, the estimates of Q_s seem to be homogeneously distributed over the country regardless of the frequency band.

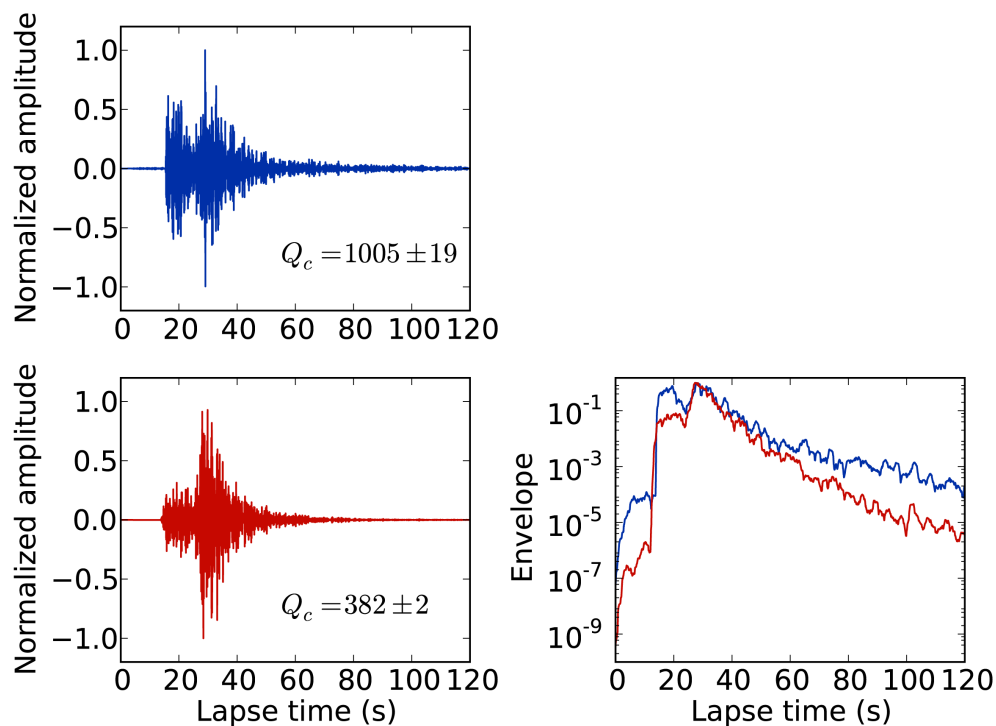


Figure 9: Two typical examples of seismograms recorded in the Alps for an earthquake of $M=3.6$, at an epicentral distance of about 85 km, in the 4-8 Hz frequency band. The smoothed envelopes as a function of lapse time are plotted on the right of the figure. Notice the large difference of coda attenuation observed at a regional scale.

Figure 9.a shows two typical examples of seismograms recorded in the Alps at the same epicentral distance ($\Delta \sim 85$ km) for an earthquake of magnitude 3.5. The station locations are depicted by the blue and red points on figure 8, respectively. We can observe notable differences in both the shape and duration of the signals. In particular, the blue envelope exhibits a rate of decay of the coda roughly 2.5 times slower than the red envelope (Fig. 9.b). This suggests a clear difference of attenuation properties below the two recording stations which is not visible on the attenuation maps of Campillo & Plantet [1991].

Following the work of Calvet et al. [2013], who have revealed fine scale (~50 km) variations of coda attenuation along the Pyrenean range, we have applied their mapping technique to a dataset of waveforms recorded in the Alps. Our aim is to illustrate in greater detail the spatial variations of Q_c for the alpine range.

3.2 Data and networks

In this study, we analyse velocity waveform data recorded by permanent and temporary seismic networks in the French Alps and surrounding regions. The area of investigation extends from the Rhine Graben in the north, to the northern Apennine Range in the south, and includes the Eastern and Western Alps. We have selected about 2000 weak to moderate earthquakes, which occurred between 1995 to 2013, with local magnitude ranging from 3 to 6. Focal depths vary between 1 km and 20 km. Location of epicenters, local magnitude and origin time of earthquakes have been determined by the Réseau National de Surveillance Sismique (RÉNASS) and the Centre Sismologique Euro-Méditerranéen (CSEM). Our dataset contains short period waveforms from RÉNASS (69 stations) and SismAlp (29 stations). We also include accelerometric data from RAP (Réseau Accélérométrique Permanent – 63 stations) and broadband data from the Observatories and Research Facilities for European Seismology (ORFEUS) data center through requests with the ArcLink protocol. Most of the short period and accelerometric data are recorded by triggered systems which often implies short coda durations, whereas broadband stations record continuously. Locations of epicenters and stations are reported on Figure 10. Waveforms were selected to have an epicentral distance smaller than 200 km. In this epicentral distance range, records show a prominent S-wave coda, which facilitates the investigation of spatial variations of attenuation.

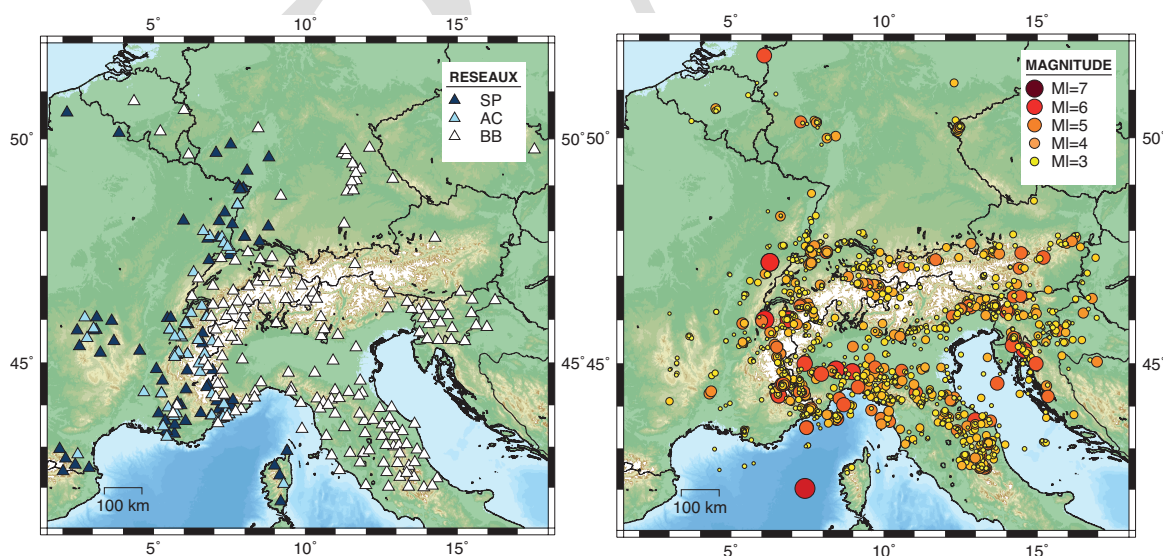



Figure 10: (a) Locations of stations used in this study. Short period (SP), accelerometric stations (AC) and broadband (BB) are denoted with a dark-blue triangle, light-blue triangle and white triangle respectively. (b) Seismicity of the Alps in the 1995 to 2013 period. The color scale indicates the range of local magnitude estimated for each event.

| | | |
|--|--|---|
|  | <p>Research and Development Programme on Seismic Ground Motion</p> <p>CONFIDENTIAL <i>Restricted to SIGMA scientific partners and members of the consortium, please do not pass around</i></p> | <p>Ref : SIGMA-2014-D2-113 Version : 01</p> <hr/> <p>Date : 2014-06-05 Page :</p> |
|--|--|---|

The available dataset comprises more than 88000 waveforms with both long and short coda duration, sometimes affected by undesired signals such as aftershocks, storms, etc. We have developed an automated algorithm to select records with long coda duration, free from any undesired arrivals. To be selected, the records should obey the following criteria:

- (1) Record duration larger than 70 seconds.
- (2) Coda duration larger than 20 seconds. We define the coda window as follows: it starts at the time where the smoothed envelope defined by Aki & Chouet [1975] (see section 2) is maximal and ends at the time where the SN ratio is lower than 4. Note that the noise level is taken at the beginning of the signal, in a window of length 5 seconds.
- (3) Intensity should decrease continuously in a coda window of maximal duration $L_w=100s$. The coda window is divided into overlapping subwindows of length 5s and characterized by a central time τ . We compute the mean intensity for each subwindow and we select records for which the mean intensity decreases with the central time τ .

The automatic selection removes 48% of the records from the initial database: the criterion (1) removes 7% of the records, and the combination of the criteria (1) and (2) removes 39% of the waveforms.

To test the robustness of our automatic selection program, we selected manually clean coda records from a subset of our initial database. This visual inspection rejects 38% of the records only, but at the expense of a highly time-consuming procedure. Considering the 10% loss as acceptable, the selection program has been then applied to the whole dataset of waveforms recorded in the Alps (~88000 waveforms). The final dataset of clean codas is composed of about 41000 waveforms on which we will perform the estimation of Q_c .

3.3 Coda window definition

Because the estimate of Q_c is lapse-time dependent [Calvet & Margerin, 2013], we have to optimize the choice of coda window parameters (t_w , L_w) and epicentral distance range Δ to minimize potential measurement biases. In this paragraph, we consider data band-passed around a central frequency of 6 Hz. We adopt the procedure of Aki & Chouet [1975] and retain estimates of Q_c when the correlation coefficient of the linear fit exceeds 0.9 (see section 2). Figure 11 illustrates the lapse time dependence of Q_c , for an onset of the coda window $t_w=2t_s$ – commonly adopted in seismological literature – and a duration of the coda $L_w=30s$. At short epicentral distance, the coda window is located closer to the S-wave arrival than at larger epicentral distance and Q_c is thus underestimated. Consequently, if different coda windows are mixed (early and late coda window), it will be difficult to distinguish variations of Q_c caused by variations of the epicentral distance, from variations of Q_c caused by spatial variations of the attenuation. To avoid this problem, the epicentral distance range must be bounded, and the coda window parameters (t_w , L_w) must be chosen in a way such that the measurements are free from any lapse-time dependence.

First, we limit the epicentral distance to the range 50-80 km and explore different onsets of coda window: $t_w=50s$, $t_w=60s$ and $t_w=70s$ after the origin time of the earthquake. Note that t_w is always larger than $2t_s$. We vary the duration of the coda window (L_w) between 20s and 130s. Figure 12 clearly displays an overall increase of Q_c with L_w , which is known as lapse-time dependence of

coda Q in the literature. Q_c typically varies from 350 at shot lapse-time to 750 at long lapse-time. Note that Q_c does not increase indefinitely with the lapse-time, but rather stabilizes around a plateau value of 750 ± 200 . The length of the coda window required to reach the plateau decreases as the onset time of the coda increases ($L_w=80s$ for $t_w=50s$ and $L_w=50s$ for $t_w=70s$). For sufficiently large L_w ($\geq 80s$), the plateau is always reached, independent of t_w . However, with the available data, we cannot impose such a long coda duration, because seismic records are often either truncated or hampered by the noise level. For the epicentral distance range 50-80 km, we thus select the following coda window parameters: $t_w=70s$ and $L_w=50s$.

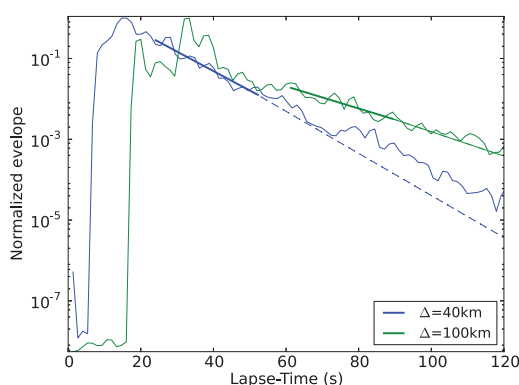


Figure 11: Normalized intensity envelopes of two seismic signals recorded at an epicentral distance of 40 km (blue) and 100 km (green) in the 4-8 Hz frequency band. Envelopes have been corrected from the geometrical term ($t^{3/2}$). The coda onset is taken at the classical value $t_w=2t_s$. The thick lines indicate the coda decay estimated by linear regression of the logarithm of intensity as a function of time. Because the blue data are recorded at shorter epicentral distance, the coda decay may be overestimated in this case.

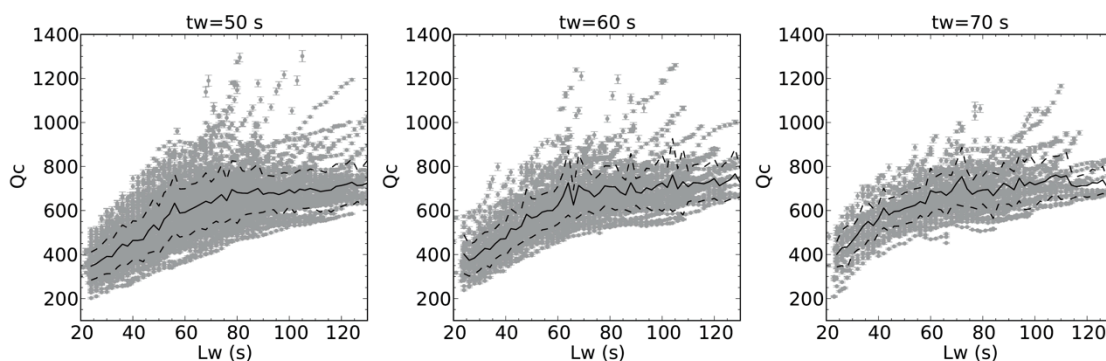



Figure 12: Q_c as a function of the coda duration L_w in the 4-8 Hz frequency band. The epicentral distance ranges from 50 to 80km. Each measurement is denoted by a grey point with the associated error bar. The solid and dashed lines show the mean lapse time dependence of Q_c and the associated uncertainties respectively. The analysis has been performed for three onsets of coda window: $t_w=30s$ (left), $t_w=50s$ (center) and $t_w=70s$ (right). Q_c reaches a plateau at long lapse time in the coda ($t_w=70s$) with a duration $L_w=50s$.

| | | |
|--|--|---|
|  | <p style="text-align: center;">Research and Development Programme on Seismic Ground Motion</p> <p style="text-align: center;">CONFIDENTIAL <i>Restricted to SIGMA scientific partners and members of the consortium, please do not pass around</i></p> | <p>Ref : SIGMA-2014-D2-113 Version : 01</p> <hr/> <p>Date : 2014-06-05 Page :</p> |
|--|--|---|

We interpret the variations of Q_c (± 200) around the plateau as an indication of strong lateral variations of attenuation in the Alps. Note that the uncertainty of individual measurements is typically (± 20), which is one order of magnitude lower than the observed spatial variation of Q_c (see error bars in Fig. 12).

We now explore the measurements of Q_c in a larger epicentral distance range. Figure 13 shows Q_c at 6 Hz as a function of epicentral distance for $tw=70s$ and $Lw=50s$. The purpose of this plot is to determine the range of epicentral distance which guarantees that Q_c is indeed estimated on the plateau identified in Figure 12. While Q_c is almost independent of the travel distance for $\Delta < 180km$, we observe that Q_c decreases for larger epicentral distances Δ . This observation is consistent with the lapse-time dependence shown in Fig. 12. For $\Delta > 180 km$, the ballistic time of S-wave is typically larger than 50s. Because the coda onset is fixed ($tw=70s$), Q_c is estimated in the very early coda where the energy decay is faster in this case.

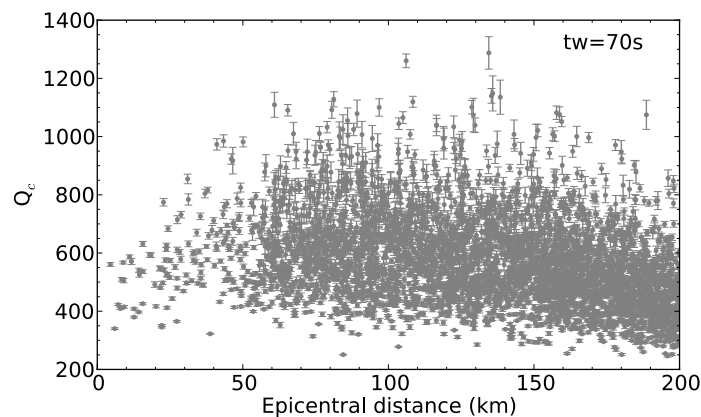


Figure 13: Q_c as a function of epicentral distance in the 4-8 Hz frequency band. The onset and duration of the coda window are fixed ($tw=70s$, $Lw=50s$).

Following the previous discussion, we conclude that the best compromise is to measure Q_c in a coda window of duration 50s, starting 70s after the origin time of the earthquake, for epicentral distances smaller than 180 km. Note that we verified that Q_c is independent of Δ ($\Delta \leq 180 km$) in the four frequency bands of interest.

3.4 Q_c maps

- **Mapping methodology**

In each frequency band (1-2Hz, 2-4Hz, 4-8Hz and 8-16 Hz), we follow the mapping method employed by Calvet et al. [2013] for the Pyrenees. Only 2-D lateral variations of Q_c are considered in this approach. The target region is discretized into pixels of dimension $50 km \times 50 km$. For each source receiver pair, Q_c is measured using the procedure outlined in section 2.1.1 and the value of Q_c is stored in each pixel crossed by the direct ray path between the source and the station. An average over all paths is performed to obtain the local value of Q_c . A spatial smoothing over an area covering a square of 9 pixels is subsequently applied. Only pixels crossed by more than 3 ray paths are retained.

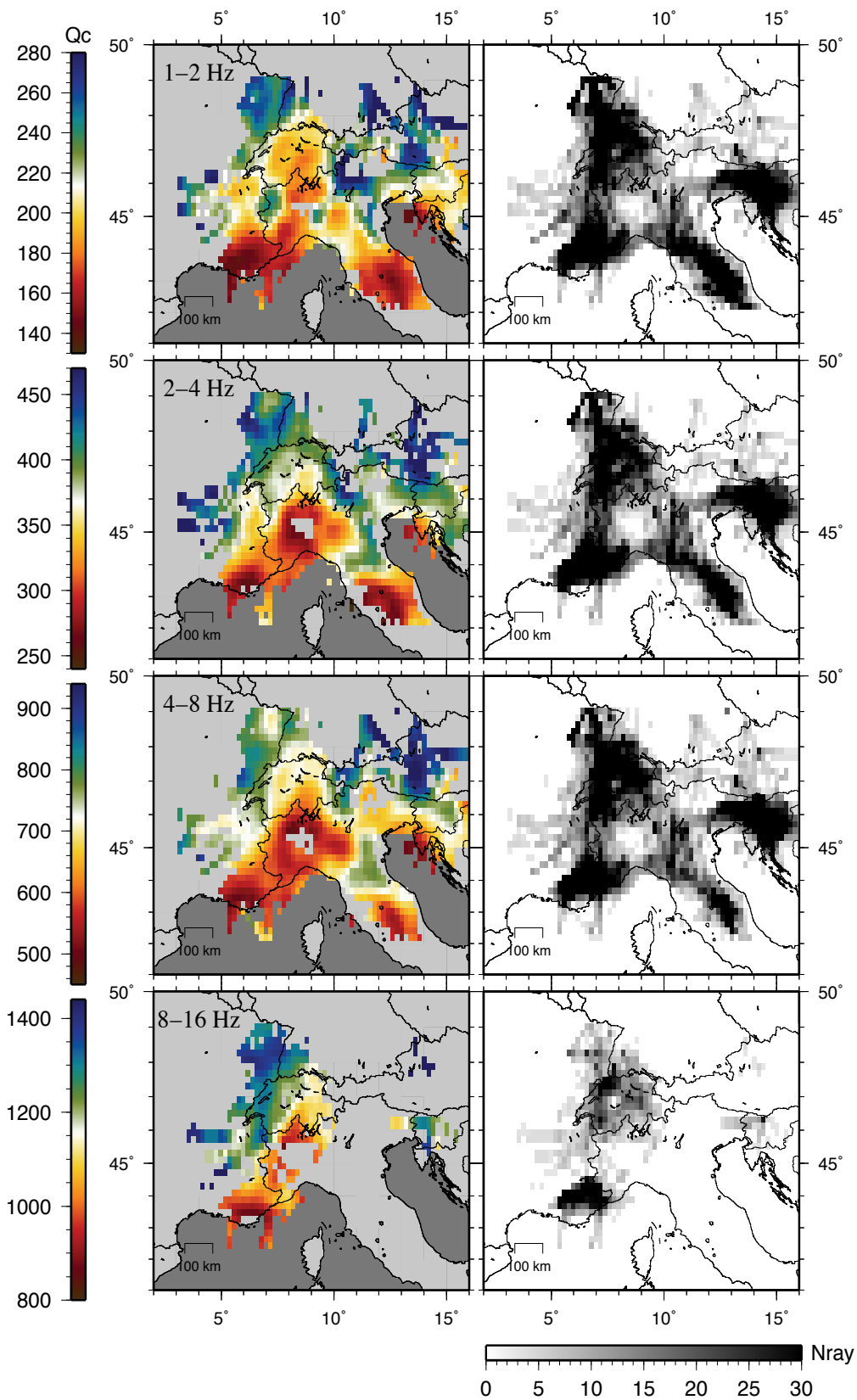


Figure 14: Left: Map of the regional variations of Q_c . Right: ray path density. Q_c is estimated in four frequency bands, from [1-2] Hz (top) to [8-16] Hz (bottom).

- **Q_c maps**

We have applied the methodology described above to map the spatial variations of Q_c in the Alpine range. Figure 14 shows the spatial distribution of Q_c and the ray path density in the four frequency bands (from [1-2] Hz to [8-16] Hz). Low attenuation (large Q_c values) is indicated in blue whereas strong attenuation (low Q_c values) is indicated in red. The spatial coverage of the Alpine range is rather good from 1 to 8 Hz. Because we have unfortunately requested waveforms with a sampling rate of 20 Hz, we do not have high-frequency measurements in the eastern part of the Alps. This deficiency will be remedied soon.

At all frequencies, the ratio between the lowest and largest value of Q_c is typically larger than 2. The typical scale of the spatial variations of the coda quality factor is of the order of 100 km, which suggests rapid lateral variation of attenuation properties in the crust.

Some geological formations such as the Upper Rhine Graben and the eastern Alps show up clearly on the maps and systematically exhibit lower attenuation than the Po Valley and the Apennines. High-attenuation in the Apennines had been previously proposed, based on the rapid attenuation of the coda of Pn-waves [Mele et al., 1996]. The French Alps are characterized by an attenuation gradient increasing from the north-west to the south-east. Even if the attenuation pattern is complex it appears relatively independent of frequency. A notable exception is a low attenuation region located between Torino and Geneva, which is clearly visible in the 1-2 Hz frequency band and disappears at higher frequencies. This region encompasses the Ivrea body, which exhibits both fast seismic velocities in the upper crust, and a large positive gravity anomaly. This geophysical anomaly is interpreted as a piece of lithospheric mantle which has been sandwiched in the crust during the formation of the alpine range (near the Mont-Blanc massif). Our observation of high- Q_c in the Ivrea zone strongly suggests that small-scale heterogeneities (and not absorption) are at the origin of the Lg propagation anomalies reported in the literature (Nicolas et al. [1982], Campillo et al. [1993]).

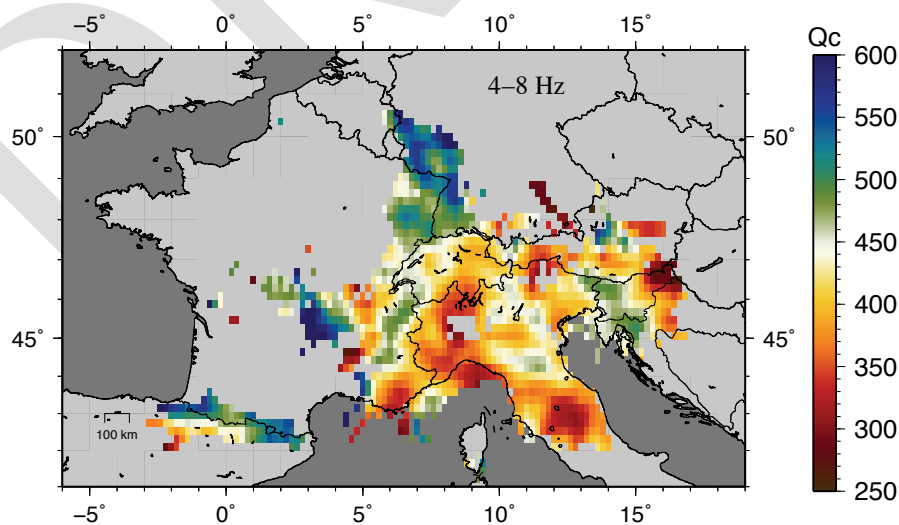



Figure 15: Regional variations of Q_c in the main French geological formations: Pyrenees, Rhine Graben and Alps, in the 4-8 Hz frequency band. The alpine range appears clearly more attenuating (low Q_c in red color) than other regions.

| | | |
|--|--|---|
|  | <p>Research and Development Programme on Seismic Ground Motion</p> <p>CONFIDENTIAL <i>Restricted to SIGMA scientific partners and members of the consortium, please do not pass around</i></p> | <p>Ref : SIGMA-2014-D2-113 Version : 01</p> <p>Date : 2014-06-05 Page :</p> |
|--|--|---|

3.5 Conclusion

Even if this work is still in progress, Q_c maps show that the attenuation strongly varies over the Alpine range. Q_c maps delineate the main geological features such as the Apennines and the Po Valley with high attenuation, and, the Upper Rhine Graben and the eastern Alps with low attenuation. We have already started to map Q_c in other regions of France in the 4-8 Hz frequency band (Fig. 15). With our available dataset, it clearly appears that attenuation in the Pyrenees and the Rhine Graben is lower than in the Alpine range which qualitatively agrees with the estimate of Q_s proposed by Drouet et al. [2010].

We expect to obtain a much more detailed map of attenuation by adopting a finer tomographic grid in regions where the density of ray paths is large, in particular in southeastern France, in the Rhine Graben and in the Apennines. To improve the spatial coverage, we will complement our current dataset with waveforms from the Laboratoire de Détection et de Géophysique (LDG-CEA) and from temporary networks (e.g: PYROPE, PYROPE +).

4. Sensitivity of coda waves to spatial variations of scattering and absorption


In this section, we propose to study the sensitivity of coda waves to spatial variations of scattering and absorption. After a review of different observations which allow the quantification of the two different processes (scattering/absorption), we will detail the theory of sensitivity kernels underlying the tomographic approach we intend to develop. We conclude this part by showing examples of sensitivity kernels of coda waves to spatial variations of absorption and scattering.

4.1 Observations

Numerous studies have documented spatial variations of seismic wave attenuation in the crust from coda waves analysis [e.g: Xie & Mitchell, 1990; Nishigami, 2000; Taira et al., 2007; Mitchell et al., 2008; Carcolé and Sato, 2010; Calvet et al., 2013]. Q_c maps obtained for the Alps (Fig. 14) and Metropolitan France (Fig. 15) clearly show that the attenuation is not spatially homogeneous. However, the physical interpretation of Q_c is ambiguous and depends on the lapse time. As discussed in the introduction of this report, two observations, one at long lapse time and another at short lapse time, will be necessary to quantify the relative contribution of scattering and absorption to the total attenuation. At sufficiently large lapse time, Q_c is expected to be close to Q_i . Carcolé & Sato [2010] found that the spatial dependence of Q_c is very well correlated with fine-scale lateral variations of the intrinsic quality factor of shear waves. By contrast, Q_c at short lapse time in the coda is sensitive to both scattering and absorption.

To quantify the strength of the scattering, the peak delay time of shear waves (Tpd) [Sato, 1989; Obara & Sato, 1995] may also be employed. Tpd is defined as the time lag between the onset of shear waves and the maximum of the seismogram envelope. It primarily reflects the scattering properties of the medium. One remarkable example of peak delay time analysis has been provided by Takahashi et al. [2007]. They showed that Tpd increases drastically when the direct S-wave path between source and station intersects the quaternary volcanoes in northern Japan.

By comparing maps of Q_c at long lapse time and Tpd in the Pyrenean range, Calvet et al. [2013]

| | | |
|--|--|---|
|  | <p>Research and Development Programme on Seismic Ground Motion</p> <p>CONFIDENTIAL <i>Restricted to SIGMA scientific partners and members of the consortium, please do not pass around</i></p> | <p>Ref : SIGMA-2014-D2-113 Version : 01</p> <p>Date : 2014-06-05 Page :</p> |
|--|--|---|


have proposed a qualitative interpretation of the origin of seismic attenuation (absorption/scattering). For example, in the Eastern Pyrenees, they proposed that absorption is dominant over scattering at high frequency. Because both Q_c and T_{pd} are influenced simultaneously by scattering and absorption, more quantitative analyses are necessary to confirm (or infirm) these conclusions. As an example, a strong absorption anomaly may significantly shift the maximum of the seismogram towards short lapse time [Saito et al., 2002] and be misinterpreted as a sign of weak heterogeneity in the medium.

The MLTWA approach developed by Fehler et al. [1992] permits to quantitatively retrieve Q_i and Q_{sc} as a function of frequency by modeling the spatio-temporal distribution of energy in the coda. The energy is estimated in consecutive lapse time windows, the first window including the S-wave arrival. By appropriately regionalizing the data, it is thus possible to obtain maps of scattering and absorption parameters with high level of details as illustrated by Carcolé & Sato [2010] for Japan. However, the MLTWA analysis cannot be considered as a genuine tomographic method for two reasons: (1) it relies on an a priori regionalization of the data and (2) MLTWA only retrieves an equivalent uniform model of scattering and absorption that fits the data.

We thus propose to develop a tomographic approach to map scattering and absorption anomalies from coda waves. We explicitly take into account the spatial variations of propagation properties in a given region, which is in sharp contrast with the regionalization approaches discussed above. The first step of a classical tomography as summarized by Nolet [2008] is to derive linearized relations between a given seismic observable – the intensity in the coda (e.g) – and the governing physical parameters – the scattering and absorption quality factors. These relations depend on so-called sensitivity kernels which quantify the perturbation of the detected intensity induced by a local perturbation of the propagation properties. As the spatial sensitivity of Q_c was not clearly understood, various mapping strategies have been previously proposed. For example, to obtain the Q_c maps shown in Fig. 14, we have chosen to distribute the sensitivity of the measurement of Q_c along the ray path between the source and the receiver. This choice has been supported by the works of Pacheco & Snieder [2005] and Rossetto et al. [2011] who have shown that in the diffusive propagation model (at long lapse time), the sensitivity of coda waves is expected to be larger at the the source, the receiver and on the direct ray path. Because coda waves sample the area contained in the single scattering ellipse whose foci are located on the source and on the receiver, some authors, e.g. Xie & Mitchell [1990], have also proposed to distribute homogeneously the sensitivity of the Lg-coda (and thus Q_c measurements) inside the single-scattering ellipse. In the next section, these assumptions will be critically examined by computing the sensitivity of coda waves to scattering and absorption using a multiple-scattering model.

4.2 Theory

To model the transport of energy in a scattering and absorbing medium, we introduce the radiative transfer equation satisfied by the specific intensity $I(\mathbf{r}, \hat{\mathbf{n}}, t)$:

| | | |
|--|--|---|
|  | <p style="text-align: center;">Research and Development Programme on Seismic Ground Motion</p> <p style="text-align: center;">CONFIDENTIAL <i>Restricted to SIGMA scientific partners and members of the consortium, please do not pass around</i></p> | <p>Ref : SIGMA-2014-D2-113 Version : 01</p> <hr/> <p>Date : 2014-06-05 Page :</p> |
|--|--|---|

$$(\partial t + c \hat{\mathbf{n}} \cdot \nabla) I(\mathbf{r}, \hat{\mathbf{n}}, t) = - \left(\frac{\omega}{Q_{sc}(\mathbf{r})} + \frac{\omega}{Q_i(\mathbf{r})} \right) I(\mathbf{r}, \hat{\mathbf{n}}, t) + \frac{\omega}{Q_{sc}(\mathbf{r})} \int_{S^{d-1}} p(\hat{\mathbf{n}}, \hat{\mathbf{n}}') I(\mathbf{r}, \hat{\mathbf{n}}', t) d\hat{\mathbf{n}}' + S(\mathbf{r}, \hat{\mathbf{n}}, t) \quad (15)$$

The specific intensity quantifies the flux of energy directed around the unit vector $\hat{\mathbf{n}}$ at point \mathbf{r} and time t in a scattering medium. The parameter ω denotes the angular frequency. In this work, we consider only infinite 2-D random media with constant background velocity c . The quantity $Q_{sc}(\mathbf{r})$ denotes the spatially varying quality factor of scattering, which controls the strength of the scattering in the heterogeneous medium. $Q_i(\mathbf{r})$ corresponds to the spatially varying intrinsic quality factor. Note that the radiative transfer equation has so far been used to retrieve spatially-independent attenuation parameters Q_i and Q_{sc} by regionalization approaches [Gusev & Abubakirov, 1999a; Margerin et al., 1999; Carcolé & Sato, 2010; Calvet & Margerin, 2013]. Scattering anisotropy is described by the phase function $p(\hat{\mathbf{n}}, \hat{\mathbf{n}}')$, which gives the probability that energy propagating in direction $\hat{\mathbf{n}}'$ be deflected into direction $\hat{\mathbf{n}}$. The source of energy is encapsulated in the term $S(\mathbf{r}, \hat{\mathbf{n}}, t)$ which describes the flux injected in the medium in direction $\hat{\mathbf{n}}$ at point \mathbf{r} and time t . Finally, the symbol $\int_{S^{d-1}} d\hat{\mathbf{n}}'$ denotes an integral over the unit sphere of space directions in d -dimensional space. Equation (15) can be deduced at the phenomenological level from a local balance of energy. In seismology, radiative transfer has become a standard tool to model the propagation of short-period seismic waves as reviewed in the book by Sato et al. [2012].

To derive the sensitivity kernel, we use standard perturbation theory as applied to other linear partial differential equations of physics. The method assumes that spatial variations of absorption and scattering properties are superposed upon a statistically homogeneous background with quality factor Q_{sc}^0 and Q_i^0 for scattering and absorption, respectively. The perturbation of the reference medium can be written as follows:

$$\frac{1}{Q_{sc}(\mathbf{r})} = \frac{1}{Q_{sc}^0} + \delta \left(\frac{1}{Q_{sc}(\mathbf{r})} \right) \quad (16a)$$

$$\frac{1}{Q_i(\mathbf{r})} = \frac{1}{Q_i^0} + \delta \left(\frac{1}{Q_i(\mathbf{r})} \right) \quad (16b)$$

The weak perturbation condition demands in addition that perturbations of absorption $\delta \left(\frac{1}{Q_i(\mathbf{r})} \right)$ and of scattering $\delta \left(\frac{1}{Q_{sc}(\mathbf{r})} \right)$ are smaller than the parameters of attenuation of the reference medium. Upon inserting Equations (16) into (15), it can be shown that the perturbation of the intensity in the coda can be written in the following linearized form:

$$\delta I(\mathbf{r}; \mathbf{r}_0; t) = \int K^a(\mathbf{r}; \mathbf{r}'; \mathbf{r}_0; t) \delta \left(\frac{1}{Q_i(\mathbf{r})} \right) d\mathbf{r}' + \int K^{sc}(\mathbf{r}; \mathbf{r}'; \mathbf{r}_0; t) \delta \left(\frac{1}{Q_{sc}(\mathbf{r})} \right) d\mathbf{r}' \quad (17)$$

The complete derivation of Equation (17) can be found in Mayor et al. [2014] (see appendix 3).

Equation (17) expresses the perturbation of the intensity in the coda δI as a function of the perturbations of scattering and absorption, weighted by their sensitivity kernels denoted by K^{sc} and K^a , respectively. These two kernels depend on the positions of the source (\mathbf{r}_0), receiver (\mathbf{r}), perturbation (\mathbf{r}') and on the lapse time t in the coda. We remind that K^{sc} and K^a quantify the perturbation of the detected intensity induced by a local perturbation of the propagation properties. These two kernels are themselves expressed as a convolution between two specific intensities which require the solution of two transport problems: one from the source to the perturbation and another from the receiver to the perturbation (the exact mathematical forms of K^a and K^{sc} are given in Mayor et al. [2014]). As is well known, the intensity that propagates in a scattering medium is composed of a coherent (or un-scattered) part and a diffuse (or incoherent) part. The word “diffuse” refers here to the intensity which has been scattered at least once in the medium. We thus have to consider four different paths from the source to the receiver through the perturbation to compute the total kernel: a coherent-coherent path, a coherent-diffuse path, a diffuse-coherent path and a diffuse-diffuse path as illustrated in figure 16. These four possible combinations contribute to the total sensitivity in a different way, as will be discussed in the next section.

The computation of the sensitivity kernels requires the knowledge of the Green’s function of the radiative transfer equation, including the full angular dependence of the specific intensity (Eq. 15). In this work, we consider a simplified physical situation: isotropic scattering ($p(\hat{\mathbf{n}}, \hat{\mathbf{n}}')=1$ in Eq.(15)) in two dimensions. From a more practical point of view, 2-D kernels may provide a first idea of the sensitivity of scattered surface waves to lateral variations of scattering and absorption properties. In this simple 2-D isotropic model, a closed-form expression for the Green’s function of the radiative transfer equation has been derived by Paasschens [1997], including the angular dependence required for our purposes. Armed with this analytical solution, we will examine the role of spatial variations of absorption first and we will then present the results for scattering.

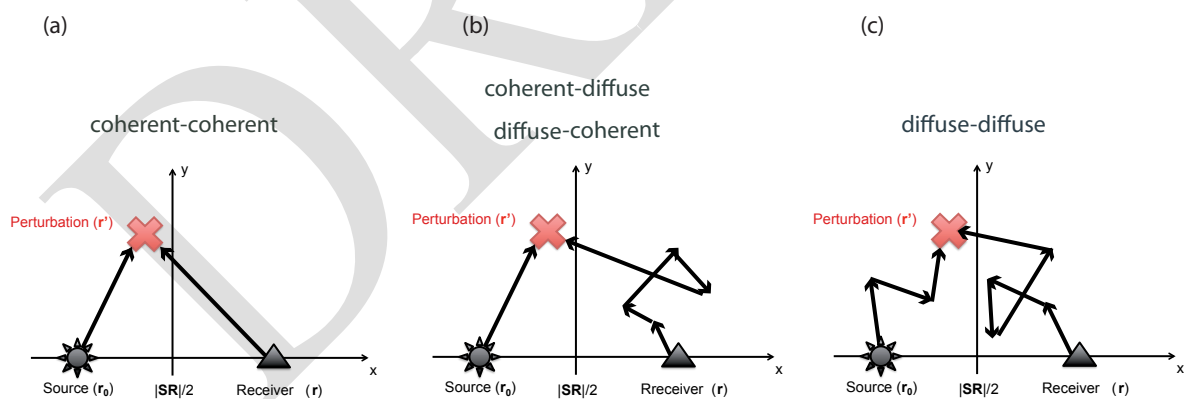



Figure 16: Schematic views of the different possible path to go from the source to the receiver through the perturbation: (a) coherent-coherent, (b) coherent-diffuse or diffuse-coherent and (c) diffuse-diffuse. The source, receiver and perturbation position vectors are denoted by \mathbf{r}_0 , \mathbf{r} and \mathbf{r}' , respectively. We introduce non-dimensional Cartesian coordinates (\bar{x}, \bar{y}) expressed in l_0 units, with $l_0 = cQ_{sc}^0/\omega$ the reference mean free path of the background medium. In this coordinate system, the source is located at $(-\bar{SR}/2, 0)$ and the receiver at $(\bar{SR}/2, 0)$.

| | | |
|--|--|---|
|  | <p>Research and Development Programme on Seismic Ground Motion</p> <p>CONFIDENTIAL <i>Restricted to SIGMA scientific partners and members of the consortium, please do not pass around</i></p> | <p>Ref : SIGMA-2014-D2-113 Version : 01</p> <hr/> <p>Date : 2014-06-05 Page :</p> |
|--|--|---|

4.3 Results

In this subsection, we discuss the spatial pattern of the sensitivity kernels for absorption (Fig. 17) and scattering (Fig. 18). The kernels are plotted using non-dimensional Cartesian coordinates (\bar{x}, \bar{y}) expressed in l_0 units, with $l_0 = cQ_{sc}^0/\omega$ the reference mean free path which described the characteristic length between two scattering events. Note that the kernels are normalized by the inverse of the scattering quality factor of the reference medium $1/Q_{sc}^0$ because of this change of variable. Typically, l_0 is of the order of 100 km in the continental crust whereas in volcanic areas where scattering is much stronger, l_0 is of the order of 1 km. In Fig. 17 and 18, the source and the receiver (black dots) are located on the horizontal axis $\bar{y}=0$ at $\bar{x}=\pm 0.5$, *i.e.* for an epicentral distance of the order of the reference mean free path l_0 . Kernels are plotted for three lapse times in the coda: the classical $t=2t_s$ (top) close to the S-wave arrival, $t=3t_s$ (middle) and $t=4t_s$ (bottom).

The total kernel results from the summation of the four contributions discussed above. Figure 17 and 18 show, from left to right, map views of the coherent-diffuse (K^{cd}), diffuse-diffuse (K^{dd}) and total kernels (K^a , K^{sc}). Note that the coherent-diffuse and the diffuse-coherent terms are both encapsulated in the coherent-diffuse contribution denoted by K^{cd} in these figures, because the paths are symmetric. The coherent-diffuse and diffuse-diffuse kernels have been calculated as follows: the region of the plane $[-w, w] \times [0, w]$ is discretized on a 2-D grid of dimension $(2N+1) \times (N+1)$ delimiting $2N \times N$ pixels (N typically equal to 100), the value of the kernel is evaluated at the centre of each pixel and stored in a matrix. Using the symmetry of the kernel with respect to reflection across the horizontal axis, the complete map is obtained. To easily discuss the weight of the different contributions to the total sensitivity, the kernels have been normalized so that the absolute value of the total sensitivity equals 1 at the midpoint of the source-receiver path. The black ellipse delimits the causality domain (or the single scattering ellipse) outside which the kernels equal zero. To enhance the visibility of the kernels, the colour scale has been saturated.

In the next paragraph, we propose to briefly discuss the spatial pattern of the sensitivity kernels and the relative contribution of K^{cc} , K^{cd} and K^{dd} to the total kernels (more details can be found in Mayor et al. [2014]). Note that if $l_0 \sim 100$ km, the spatial and temporal scale used in Fig. 17 and 18 is typical of coda detection at local to regional distances.

▪ Absorption kernel

Let us first remark that the absorption kernels are negative because absorption removes energy from the system. Moreover, by contrast with the hypothesis of Xie & Mitchell [1990] previously discussed, the sensitivity is not homogeneously distributed inside the single-scattering ellipse. Note that, the contribution of the coherent-coherent contribution is not shown in Figure 17 because it only impacts the ballistic S-wave (see Mayor et al. [2014]).

For a source-station distance of one mean free path and lapse times in the range $[2t_s-4t_s]$, the total absorption kernel is dominated by the coherent-diffuse kernel. K^{cd} exhibits maximal sensitivity at the location of the source and station because all scattered wave paths have to propagate through a neighbourhood of these two points. The diffuse-diffuse term mainly adds some extra sensitivity in the bulk of the medium. Nevertheless, the zone of highest sensitivity in the total kernel is localized

around the direct ray connecting the source and receiver, which strongly suggests that local information on the absorption structure may be retrieved from the coda. It also justifies a posteriori our mapping strategy for Q_c in the Alps.

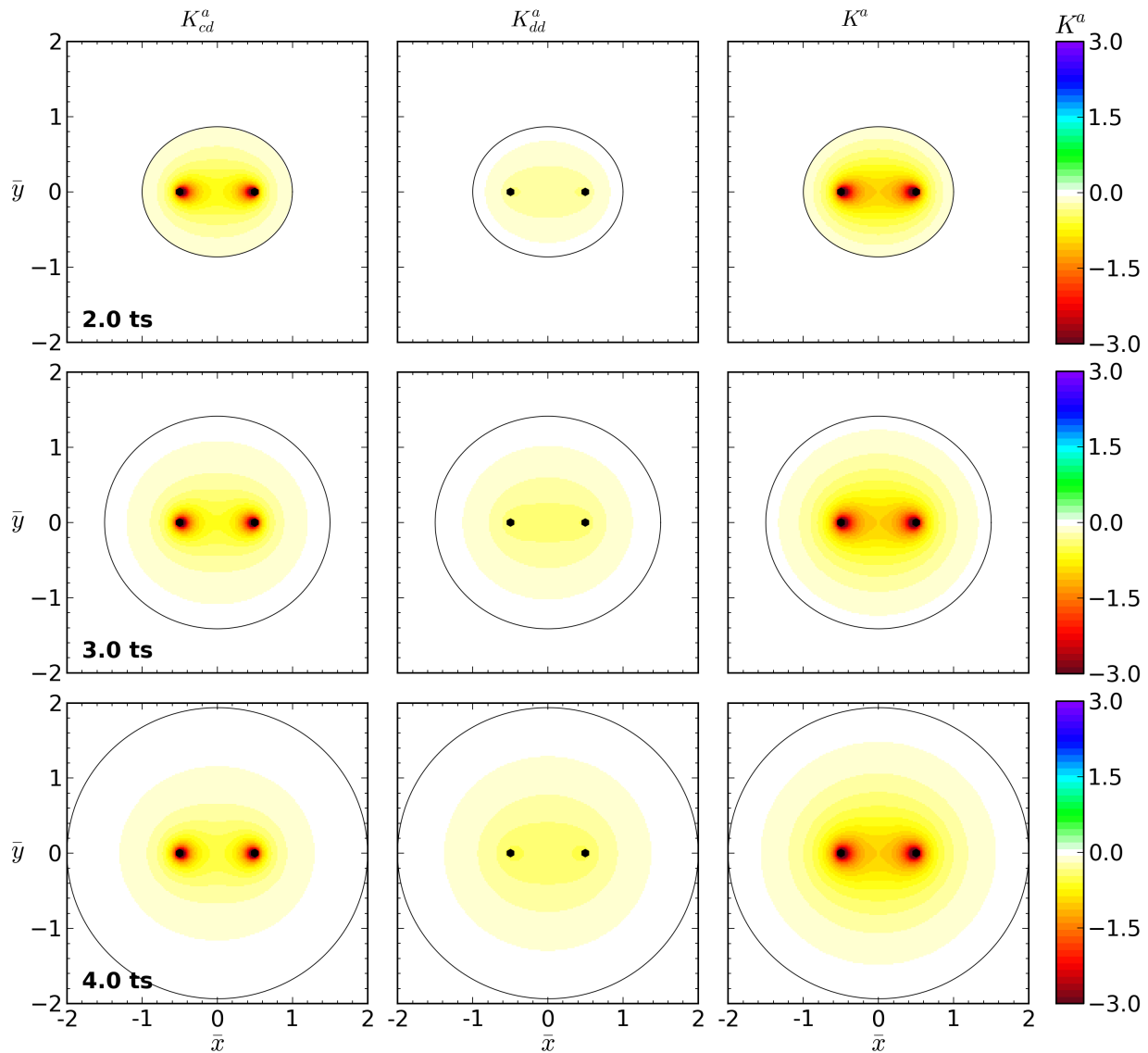



Figure 17: Colour maps of the absorption sensitivity kernels for source–station distance $SR = l_0$, and propagation times $t = 2t_s$ (top), $t = 3t_s$ (middle) and $t = 4t_s$ (bottom), with $t_s = \tau_0$ the propagation time of ballistic waves. Left: coherent–diffuse term; Centre: diffuse–diffuse term; Right: total sensitivity kernel. On the horizontal and vertical axes, the distances are expressed in mean free path units. The black ellipse delimits the causality domain outside which the kernels equal zero. The black dots indicate the position of the source and station. The kernels have been normalized so that the absolute value of the total sensitivity equals 1 at the midpoint of the source–receiver path. To enhance the visibility, the colour scale has been saturated.

| | | |
|--|--|---|
|  | <p style="text-align: center;">Research and Development Programme on Seismic Ground Motion</p> <p style="text-align: center;">CONFIDENTIAL <i>Restricted to SIGMA scientific partners and members of the consortium, please do not pass around</i></p> | <p>Ref : SIGMA-2014-D2-113 Version : 01</p> <hr/> <p>Date : 2014-06-05 Page :</p> |
|--|--|---|

▪ Scattering kernel

Figure 18 illustrates that the scattering kernel is significantly more complex than its absorption counterpart, with notable zones of positive and negative sensitivity. The coherent-coherent contribution is only shown on the total sensitivity kernel. The sensitivity of the coherent-coherent term is concentrated on the causality ellipse (or single-scattering ellipse) and decays exponentially fast in the coda. It becomes completely negligible after a few t_s .

The coherent-diffuse contribution has an algebraic singularity at the source and the receiver. It exhibits an additional square-root type singularity in the vicinity of the single scattering ellipse from the inside. The coherent-diffuse kernel has a zone of negative sensitivity of typical width one mean free path along the direct ray connecting the source and station. Inside this area, an increase of the scattering strength results in a decrease of the intensity received in the coda: the extra-scattering deflects part of the energy which would have otherwise propagated from source to station. Conversely, an extra scattering event adds some probability for waves propagating in a direction opposite to the direct ray to be backscattered to the receiver and implies an increase of the intensity received in the coda. This gives rise to the lobes of high positive sensitivity visible in Figure 18.

The diffuse-diffuse term provides some sensitivity to the variations of scattering strength in the bulk of the medium. It also exhibits a zone of negative sensitivity around the direct ray path. Indeed, at large lapse time, the diffuse-diffuse kernel depends on the scalar product between the energy current vectors of two sources: one placed at the source, and the other (virtual) at the receiver. Clearly, this scalar product will be negative on the direct ray path because the energy fluxes of the two sources are in opposite directions at all times. Conversely, elsewhere on the source-receiver path, the energy flows away from the two sources in the same direction, hence the positive sign [Mayor et al., 2014].

Figure 18 shows that the spatial pattern of the coherent-diffuse and total scattering kernels are very similar. The most clearly visible contribution of the diffuse-diffuse term is the broadening of the positive lobes of sensitivity, as well as some additional sensitivity in the bulk of the medium. Like in the case of absorption, we remark that at long lapse time in the coda, the total sensitivity is highest in a domain of width one mean free path going from source to station, but that there is some additional complexity due to the changes of sign of the kernel.

4.4 Conclusion

Our study of sensitivity functions for the intensity detected in the coda brings us to the following conclusions: (1) in the case of absorption, the sensitivity is maximal along the direct ray path connecting the source and station and diverges at these two points. A localized perturbation of absorption affects the overall decay of the coda in a manner which depends on the location of the anomaly with respect to the source and receiver; (2) in the case of scattering, the sensitivity has a much more complex structure. The scattering kernel displays a broad zone of strong negative sensitivity around the direct ray path and is positive elsewhere. In addition to the divergence at the source and station, the kernel is also singular on the single scattering ellipse and in its vicinity. Because of this intricate spatial pattern, a localized scattering anomaly has a complex signature in

the coda, and may entail a positive or negative variation of intensity depending on the lapse time. Local scattering and absorption perturbations have thus a distinct impact on the intensity received in the coda. These results suggest that a separation of scattering and absorption effects should be possible by modeling the spatio-temporal distribution of energy in the coda.

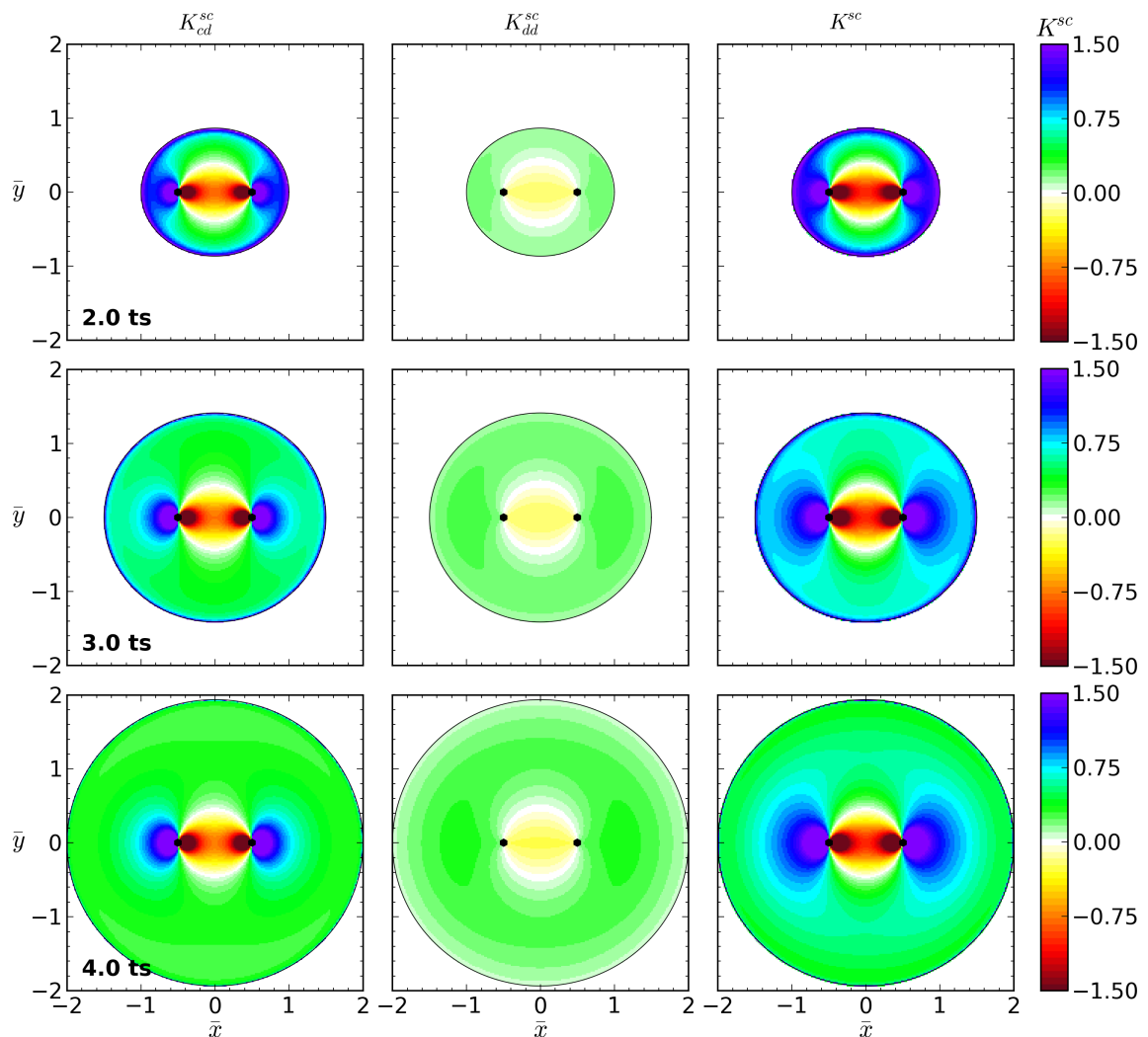



Figure 18: Colour maps of the scattering sensitivity kernels for source–station distance $SR = l_0$ and propagation times $t = 2t_s$ (top), $t = 3t_s$ (middle) and $t = 4t_s$ (bottom), with $t_s = \tau_0$ the propagation time of ballistic waves. Left: coherent–diffuse term. Centre: diffuse–diffuse term. Right: total (including the coherent–coherent part). On the horizontal and vertical axes, the distances are expressed in mean free path units. The black ellipse delimits the causality domain outside which the kernels equal zero. The black dots indicate the position of the source and station. The kernels have been normalized so that the absolute value of the total equals 1 at the midpoint of the source–receiver path. To enhance the visibility, the colour scale has been saturated.

| | | |
|--|--|---|
|  | <p style="text-align: center;">Research and Development Programme on Seismic Ground Motion</p> <p style="text-align: center;">CONFIDENTIAL <i>Restricted to SIGMA scientific partners and members of the consortium, please do not pass around</i></p> | <p>Ref : SIGMA-2014-D2-113 Version : 01</p> <hr/> <p>Date : 2014-06-05 Page :</p> |
|--|--|---|

Conclusions and Outlook

The objective of my thesis is to estimate the contribution of intrinsic and scattering attenuation (Q_i and Q_{sc}) to the total attenuation of seismic waves. In this report, we have analyzed the rate of decay of the coda, described by the coda quality factor Q_c , which is mostly sensitive to the intrinsic quality factor Q_i at large lapse time. We have made a first step towards the development of a tomographic approach to map lateral variations of Q_{sc} and Q_i from the coda intensity analysis.

In section 2, we have tested three different methods to estimate Q_c . These three methods mainly differ in their domain of analysis (spectral or temporal) and in their statistical assumptions on the fluctuations of the coda envelope. After critical examination of the three methods, we have chosen to employ the simple but well adapted technique of Aki & Chouet [1975]. This method gives a rather good estimate of Q_c in different frequency bands without any assumption on the frequency-dependence of Q_c .

In section 3, we discussed the optimal choices of epicentral distance range (0-180 km) and coda window parameters ($t_w=70s$, $L_w=50s$) to avoid biases due to the lapse time dependence of Q_c . Then, we obtained preliminary maps of Q_c for the Alps in four frequency bands ranging from 1 to 16 Hz. These maps show that the typical scale of the spatial variations of Q_c is of the order of 100 km (Fig. 15), which suggests rapid lateral variations of attenuation properties in the crust. Q_c maps delineate the main geological features such as the Appenines and the Po Valley with high attenuation, and the Upper Rhine Graben and Eastern Alps with low attenuation.


In section 4, we have briefly described the theory underpinning our tomographic approach and we have detailed the spatiotemporal sensitivity of coda intensity to scattering and absorption anomalies. The perturbation of the detected intensity caused by a local perturbation of the propagation properties is quantified by the sensitivity kernels of absorption and scattering which have been computed in 2-D isotropic scattering media. We have seen that both absorption and scattering kernels have their sensitivity concentrated on the direct ray path connecting the source and station and diverge at these two points. The two kernels present sufficiently different structures to permit the mapping of lateral variations of scattering and absorption in the crust. However, a number of steps must be taken before we reach our goal.

Concerning Q_c maps and data analysis:

- (1) We will increase our dataset to improve the data coverage in the Alps and Metropolitan France for frequencies ranging from 1 to 32 Hz. Moreover, an adaptive mesh that homogenizes the ray path density should increase the level of details of our Q_c maps in regions with a high density of source and station.
- (2) We plan to explore more deeply the lapse time dependence of Q_c in order to estimate the scattering anisotropy (and its possible lateral variations) following the work of Calvet & Margerin (2013).

Concerning the sensitivity kernels:


- (1) The limits of validity of the perturbation theory adopted in our work should be established. This question will be addressed with the aid of Monte Carlo simulations to solve the radiative transfer equation in laterally varying scattering and absorbing media.
- (2) Another important issue is to develop specific sensitivity kernels for other seismic

| | | |
|--|--|---|
|  | <p style="text-align: center;">Research and Development Programme on Seismic Ground Motion</p> <p style="text-align: center;">CONFIDENTIAL <i>Restricted to SIGMA scientific partners and members of the consortium, please do not pass around</i></p> | <p>Ref : SIGMA-2014-D2-113 Version : 01</p> <hr/> <p>Date : 2014-06-05 Page :</p> |
|--|--|---|

observables such as the peak delay time and the coda quality factor. During my PhD, I plan to develop the sensitivity kernels for Q_c .

- (3) Scattering anisotropy may play an important role in the observed spatio-temporal dependence of the coda envelope (Calvet & Margerin [2013]). Future works should take into account scattering anisotropy in the computation of the kernels. Because the calculation of the full angular dependence of the specific intensity required for our purposes is still challenging, we have first adhered to the simple isotropic scattering approximation which hopefully captures the essential features of the sensitivity.
- (4) Finally, future works should also address the possible role of depth-dependent attenuation structures, which calls for the development of 3-D sensitivity kernels.

DRAFT

| | | |
|--|--|---|
|  | <p style="text-align: center;">Research and Development Programme on Seismic Ground Motion</p> <p style="text-align: center;">CONFIDENTIAL <i>Restricted to SIGMA scientific partners and members of the consortium, please do not pass around</i></p> | <p>Ref : SIGMA-2014-D2-113 Version : 01</p> <hr/> <p>Date : 2014-06-05 Page :</p> |
|--|--|---|

References

Aki, K. & Chouet, B., (1975). Origin of coda waves: source, attenuation, and scattering effects, *J. geophys. Res.*, **80**(23), 3322–3342.

Aki, K., (1969). Analysis of the seismic coda of local earthquakes as scattered waves. *Journal of geophysical research*, *74*(2), 615-631.

Calvet, M., & Margerin, L. (2013). Lapse-Time Dependence of Coda-Q: Anisotropic Multiple-Scattering Models and Application to the Pyrenees. *Bulletin of the Seismological Society of America*, *103*(3), 1993-2010.

Calvet, M., Sylvander, M., Margerin, L., & Villaseñor, A. (2013). Spatial variations of seismic attenuation and heterogeneity in the Pyrenees: coda Q and peak delay time analysis. *Tectonophysics*, *608*, 428-439.

Campillo, M., Feignier, B., Bouchon, M., & Béthoux, N. (1993). Attenuation of crustal waves across the Alpine range. *Journal of Geophysical Research: Solid Earth (1978–2012)*, *98*(B2), 1987-1996.


Campillo, M., & Plantet, J. L. (1991). Frequency dependence and spatial distribution of seismic attenuation in France: experimental results and possible interpretations. *Physics of the earth and planetary interiors*, *67*(1), 48-64.

Campillo, M., Plantet, J. L., & Bouchon, M. (1985). Frequency-dependent attenuation in the crust beneath central France from Lg waves: data analysis and numerical modeling. *Bulletin of the Seismological Society of America*, *75*(5), 1395-1411.

Carcolé, E., & Sato, H. (2010). Spatial distribution of scattering loss and intrinsic absorption of short-period S waves in the lithosphere of Japan on the basis of the Multiple Lapse Time Window Analysis of Hi-net data. *Geophysical Journal International*, *180*(1), 268-290.

Carcolé, E., and H. Sato (2009). Statistics of the fluctuations of the amplitude of coda waves of local earthquakes, Abstracts of the Seismological Society of Japan 2009 Fall Meeting, C31-13, Kyoto, Japan.

Drouet, S., Cotton, F., & Guéguen, P. (2010). vS_{30} , κ , regional attenuation and M_w from accelerograms: application to magnitude 3–5 French earthquakes. *Geophysical Journal International*, *182*(2), 880-898.

| | | |
|--|--|---|
|  | <p style="text-align: center;">Research and Development Programme on Seismic Ground Motion</p> <p style="text-align: center;">CONFIDENTIAL <i>Restricted to SIGMA scientific partners and members of the consortium, please do not pass around</i></p> | <p>Ref : SIGMA-2014-D2-113 Version : 01</p> <hr/> <p>Date : 2014-06-05 Page :</p> |
|--|--|---|

Fehler, M., Hoshiya, M., Sato, H. & Obara, K., (1992). Separation of scattering and intrinsic attenuation for the Kanto-Tokai region, Japan, using measurements of S-wave energy versus hypocentral distance, *Geophys. J. Int.*, **108**(3), 787–800.

Gusev, A. & Abubakirov, I., (1999a). Vertical profile of effective turbidity reconstructed from broadening of incoherent body-wave pulses. I. General approach and the inversion procedure, *Geophys. J. Int.*, **136**(2), 295–308.

Gusev, A. A., & Abubakirov, I. R. (1996). Simulated envelopes of non-isotropically scattered body waves as compared to observed ones: Another manifestation of fractal heterogeneity. *Geophysical Journal International*, *127*(1), 49-60.

Gusev, A. A., & Abubakirov, I. R. (1987). Monte-Carlo simulation of record envelope of a near earthquake. *Physics of the earth and planetary interiors*, *49*(1), 30-36.

Hoshiya, M. (1995). Estimation of nonisotropic scattering in western Japan using coda wave envelopes: Application of a multiple nonisotropic scattering model. *Journal of Geophysical Research: Solid Earth (1978–2012)*, *100*(B1), 645-657.

Hoshiya, M., (1993). Separation of scattering attenuation and intrinsic absorption in Japan using the multiple lapse time window analysis of full seismogram envelope, *J. geophys. Res.*, **98**(B9), 15 809–15 824.


Hoshiya, M., (1991). Simulation of multiple-scattered coda wave excitation based on the energy conservation law, *Phys. Earth planet. Inter.*, **67**(1), 123–136.

Margerin, L., Campillo, M., Shapiro, N. & Van Tiggelen, B., 1999. Residence time of diffuse waves in the crust as a physical interpretation of coda Q: application to seismograms recorded in Mexico, *Geophys. J. Int.*, **138**(2), 343–352.

Mayor, J., Margerin, L., & Calvet, M. (2014). Sensitivity of coda waves to spatial variations of absorption and scattering: radiative transfer theory and 2-D examples. *Geophysical Journal International*, **197**, 1117-1137.

Mele, G., Rovelli, A., Seber, D., & Barazangi, M. (1996). Lateral variations of Pn propagation in Italy: Evidence for a high-attenuation zone beneath the Apennines. *Geophysical research letters*, *23*(7), 709-712.

Mitchell, B. J., Cong, L., & Ekström, G. (2008). A continent-wide map of 1-Hz Lg coda Q variation across Eurasia and its relation to lithospheric evolution. *Journal of Geophysical Research: Solid Earth (1978–2012)*, *113*(B4).

| | | |
|--|--|---|
|  | <p style="text-align: center;">Research and Development Programme on Seismic Ground Motion</p> <p style="text-align: center;">CONFIDENTIAL <i>Restricted to SIGMA scientific partners and members of the consortium, please do not pass around</i></p> | <p>Ref : SIGMA-2014-D2-113 Version : 01</p> <hr/> <p>Date : 2014-06-05 Page :</p> |
|--|--|---|

Nakahara, H., & Carcolé, E. (2010). Maximum-likelihood method for estimating coda Q and the Nakagami-m parameter. *Bulletin of the Seismological Society of America*, 100(6), 3174-3182.

Nicolas, M., B. Massinon, P. Mechler, and M. Bouchon (1982). Attenuation of regional phases in western Europe, *Bull. Seism. Soc. Am.* 72, 2089-2106.

Nishigami, K., 2000. Deep crustal heterogeneity along and around the San Andreas fault system in Central California and its relation to the segmentation, *J. geophys. Res.*, **105**(B4), 7983–7998.

Nolet, G., (2008). *A Breviary of Seismic Tomography*, Cambridge Univ. Press.

Obara, K. & Sato, H., (1995). Regional differences of random inhomogeneities around the volcanic front in the Kanto-Tokai area, Japan, revealed from the broadening of S wave seismogram envelopes, *J. geophys. Res.*, **100**(B2), 2103–2121.

Pacheco, C. & Snieder, R., 2005. Time-lapse travel time change of multiply scattered acoustic waves, *J. acoust. Soc. Am.*, **118**, 1300–1310.

Paasschens, J., 1997. Solution of the time-dependent Boltzmann equation, *Phys. Rev. E*, **56**, 1135–1141.

Phillips, W. S., & Aki, K. (1986). Site amplification of coda waves from local earthquakes in central California. *Bulletin of the Seismological Society of America*, 76(3), 627-648.


Rautian, T. G., & Khalturin, V. I. (1978). The use of the coda for determination of the earthquake source spectrum. *Bulletin of the Seismological Society of America*, 68(4), 923-948.

Rossetto, V., Margerin, L., Planès, T. & Larose, E., (2011). Locating a weak change using diffuse waves: theoretical approach and inversion procedure, *J. Appl. Phys.*, **109**, 034903, 1–11.

Saito, T., Sato, H. & Ohtake, M., 2002. Envelope broadening of spherically outgoing waves in three-dimensional random media having power law spectra, *J. geophys. Res.*, **107**(B5), doi:10.1029/2001JB000264.

Sato, H., Fehler, M.C. & Maeda, T., (2012). *Seismic Wave Propagation and Scattering in the Heterogeneous Earth*, Springer.

Sato, H., (1989). Broadening of seismogram envelopes in the randomly inhomogeneous lithosphere based on the parabolic approximation: Southeastern Honshu, Japan, *J. geophys. Res.*, **94**(B12), 17 735–17 747.

| | | |
|--|--|---|
|  | <p style="text-align: center;">Research and Development Programme on Seismic Ground Motion</p> <p style="text-align: center;">CONFIDENTIAL <i>Restricted to SIGMA scientific partners and members of the consortium, please do not pass around</i></p> | <p>Ref : SIGMA-2014-D2-113 Version : 01</p> <hr/> <p>Date : 2014-06-05 Page :</p> |
|--|--|---|

Sato, H., (1977). Energy propagation including scattering effects single isotropic scattering approximation. *J. Phys. Earth*, 25, 27-41.

Takahashi, T., Sato, H., Nishimura, T., & Obara, K. (2009). Tomographic inversion of the peak delay times to reveal random velocity fluctuations in the lithosphere: method and application to northeastern Japan. *Geophysical Journal International*, 178(3), 1437-1455.

Taira, T., Yomogida, K., Kuwahara, Y., Imanishi, K. & Ito, H., 2007. Imaging of crustal heterogeneous structures using a slowness weighted back-projection with effects of scattering modes: 2. Application to the Nagamachi-Rifu fault, Japan, area, *J. geophys. Res.*, **112**, B06312, doi:10.1029/2006JB004382.

Xie, J., & Mitchell, B. J. (1990). A back-projection method for imaging large-scale lateral variations of Lg coda Q with application to continental Africa. *Geophysical Journal International*, 100(2), 161-181.

Xie, J., & Nuttli, O. W. (1988). Interpretation of high-frequency coda at large distances: stochastic modelling and method of inversion. *Geophysical Journal*, 95(3), 579-595.

DRAFT

Appendix 1

Poster presentation: European Geosciences Union General Assembly 2014, 29 April to 2 May 2014, in Vienna (Austria).
Poster session: Seismic Imaging

LATERAL VARIATIONS OF CODA WAVE ATTENUATION IN THE ALPS

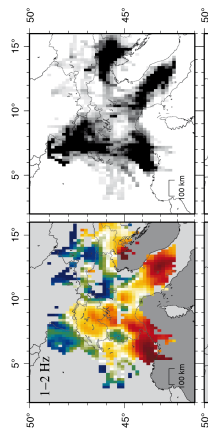
Jessie Mayor ⁽¹⁾, Marie Colvet ⁽¹⁾, Ludovic Margerin ⁽¹⁾, Paola Traversa ⁽²⁾



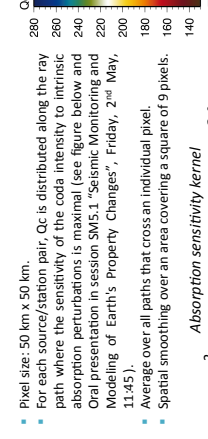
B570

ABSTRACT: We investigate lateral variations of coda wave attenuation in the Alps. We used microseismicity. The use of high-quality coda wave measurements allows us to study coda wave attenuation in the time domain. We have selected about 2000 weak to moderate earthquakes, with magnitudes ranging from 1.5 to 3.0. We have measured the coda onset time (tw) as measured from the origin time (tw) and coda onset time (tw). The map of Qc is obtained by inverting the coda onset time (tw) and coda onset time (tw) for each source/receiver pair. The estimated value of Qc is presented along the direct ray path. An average over all paths that cross an individual pixel is performed to obtain the final map of Qc. The map of Qc is obtained by inverting the coda onset time (tw) and coda onset time (tw) for each source/receiver pair. The estimated value of Qc is presented along the direct ray path. An average over all paths that cross an individual pixel is performed to obtain the final map of Qc. The map of Qc is obtained by inverting the coda onset time (tw) and coda onset time (tw) for each source/receiver pair. The estimated value of Qc is presented along the direct ray path. An average over all paths that cross an individual pixel is performed to obtain the final map of Qc.

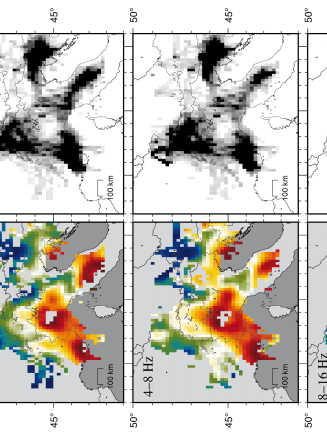
DATA SELECTION



SIGNAL PROCESSING



CHOICE OF THE CODA WINDOW



CONCLUSIONS

- The ratio between the lowest and largest value of Qc is typically larger than 2 in all frequency bands.
- The typical scale of the spatial variations of the coda quality factor is of the order of 100km, which suggests rapid lateral variation of attenuation properties in the crust.
- The attenuation pattern is complex but relatively independent of frequency.

ACKNOWLEDGEMENTS

The authors acknowledge a research grant of Electricité de France through the research program SIGMA (Seismic Ground Motion Assessment). This research has also been partially supported by the ALIAS program of INSU-CNRS. The authors would like to thank the institutions that operate permanent seismological networks in the Alps (CH, CN, FR, GE, GR, CU, IJ, MN, NI, OV, RA, SI, SE, RENASS and Sismalp).

MAPPING


- Pixel size: 50 km x 50 km.
- For each source/station pair, Qc is distributed along the ray path where the sensitivity of the coda intensity to intrinsic absorption perturbations is maximal (see figure below and Oral presentation in session SW5.1 "Seismic Monitoring and Modeling of Earth's Property Changes", Friday, 2nd May, 11:45).
- Average over all paths that cross an individual pixel.
- Spatial smoothing over an area covering a square of 9 pixels.

CONCLUSIONS

- The ratio between the lowest and largest value of Qc is typically larger than 2 in all frequency bands.
- The typical scale of the spatial variations of the coda quality factor is of the order of 100km, which suggests rapid lateral variation of attenuation properties in the crust.
- The attenuation pattern is complex but relatively independent of frequency.

ACKNOWLEDGEMENTS

The authors acknowledge a research grant of Electricité de France through the research program SIGMA (Seismic Ground Motion Assessment). This research has also been partially supported by the ALIAS program of INSU-CNRS. The authors would like to thank the institutions that operate permanent seismological networks in the Alps (CH, CN, FR, GE, GR, CU, IJ, MN, NI, OV, RA, SI, SE, RENASS and Sismalp).

| | | |
|--|--|---|
|  | <p>Research and Development Programme on Seismic Ground Motion</p> <p>CONFIDENTIAL <i>Restricted to SIGMA scientific partners and members of the consortium, please do not pass around</i></p> | <p>Ref : SIGMA-2014-D2-113 Version : 01</p> <p>Date : 2014-06-05 Page :</p> |
|--|--|---|

Appendix 2

Oral presentation: European Geosciences Union General Assembly 2014, 29 April to 2 May 2014, in Vienna (Austria).

Oral session: Seismic Monitoring and Modeling of Earth's Property Changes


Geophysical Research Abstracts
Vol. 16, EGU2014-**PREVIEW**, 2014
EGU General Assembly 2014
© Author(s) 2014. CC Attribution 3.0 License.



Sensitivity of coda waves to lateral variations of absorption and scattering: radiative transfer theory and 2-D examples

Jessie Mayor, Ludovic Margerin, and Marie Calvet
IRAP, CNRS, Université de Toulouse, France

We investigate the impact of lateral variations of absorption and scattering properties on the energy envelopes of coda waves. To model the spatio-temporal distribution of seismic energy, we employ a scalar version of the radiative transfer equation with spatially-dependent absorption and scattering quality factor. The scattering pattern which describes the angular distribution of energy upon scattering is assumed to be statistically isotropic, independent of position, but otherwise arbitrary. Further assuming that the lateral variations of the governing parameters are sufficiently weak, we employ perturbation theory to derive linearized relations between the absorption/scattering properties of the medium and the intensity detected in the coda. These relations take the form of weighted integrals where so-called scattering/absorption sensitivity kernels play the role of weighting function. The kernels depend on the type of perturbation (scattering or absorption), the lapse time in the coda, and require the knowledge of the complete angular dependence of the specific intensity describing the flow of energy in a given direction at a given location. In the long lapse-time limit, we establish simplified formulas which depend on the first two angular moments of the specific intensity only. As an illustration of the theory, we calculate the absorption and scattering sensitivity kernels in a 2-D isotropically scattering medium at different lapse times in the coda, and discuss their singularities in detail. The sensitivity kernels are then employed to calculate the relative intensity variations of the coda caused by a localized Gaussian absorption/scattering anomaly. We find that the dominant effect of absorption anomalies is to modify the decay rate of the coda, while scattering anomalies have a more complex signature, causing either positive or negative deflection of the energy envelope, depending on their location and on the lapse time. Our results suggest the possibility to locate and discriminate between scattering and absorption anomalies from the energy envelope of coda waves.

| | | |
|--|--|---|
|  | <p>Research and Development Programme on Seismic Ground Motion</p> <p>CONFIDENTIAL <i>Restricted to SIGMA scientific partners and members of the consortium, please do not pass around</i></p> | <p>Ref : SIGMA-2014-D2-113 Version : 01</p> <p>Date : 2014-06-05 Page :</p> |
|--|--|---|

Appendix 3

Paper published in Geophysical Journal International (vol: 197, 1117-1137) Sensitivity of coda waves to spatial variations of absorption and scattering: radiative transfer theory and 2-D examples

Authors: Jessie Mayor, Ludovic Margerin and Marie Calvet

DRAFT

Sensitivity of coda waves to spatial variations of absorption and scattering: radiative transfer theory and 2-D examples

Jessie Mayor, Ludovic Margerin and Marie Calvet

Institut de Recherche en Astrophysique et Planétologie, Observatoire Midi-Pyrénées, Université Paul Sabatier, C.N.R.S., 14 Avenue Edouard Belin, Toulouse, France. E-mail: Jessie.Mayor@irap.omp.eu

Accepted 2014 February 3. Received 2014 January 29; in original form 2013 December 6

SUMMARY

We investigate the impact of spatial variations of absorption and scattering properties on the energy envelopes of coda waves. To model the spatiotemporal distribution of seismic energy, we employ a scalar version of the radiative transfer equation with spatially dependent absorption and scattering quality factor. The scattering pattern which describes the angular distribution of energy upon scattering is assumed to be statistically isotropic, independent of position, but otherwise arbitrary. Further assuming that the spatial variations of the governing parameters are sufficiently weak, we employ perturbation theory to derive linearized relations between the absorption/scattering properties of the medium and the intensity detected in the coda. These relations take the form of weighted integrals where so-called scattering/absorption sensitivity kernels play the role of weighting function. The kernels depend on the type of perturbation (scattering or absorption), the lapse-time in the coda, and require the knowledge of the complete angular dependence of the specific intensity describing the flow of energy in a given direction at a given location. In the long lapse-time limit, we establish simplified formulae which depend on the first two angular moments of the specific intensity only. As an illustration of the theory, we calculate the absorption and scattering sensitivity kernels in a 2-D isotropically scattering medium at different lapse-times in the coda, and discuss their singularities in detail. The sensitivity kernels are then employed to calculate the relative intensity variations of the coda caused by a localized Gaussian absorption/scattering anomaly. We find that the dominant effect of absorption anomalies is to modify the decay rate of the coda, while scattering anomalies have a more complex signature, causing either positive or negative deflection of the energy envelope, depending on their location and the lapse-time. Our results suggest the possibility to locate and discriminate between scattering and absorption anomalies from the energy envelope of coda waves.

Key words: Coda waves; Theoretical seismology; Wave scattering and diffraction.

1 INTRODUCTION

With the rapid development of dense seismic networks in the last 20 yr, it has become clear that the attenuation structure of the lithosphere is not spatially homogeneous. High-frequency (> 1 Hz) seismic waves have been particularly useful to detect propagation anomalies associated with spatial variations of scattering and absorption properties. The strength of these anomalies may be quantified by simple measurements. One example is the peak delay time of shear waves, defined as the time difference between the onset of shear waves and the maximum of the seismogram envelope. As shown by Obara & Sato (1995), this observable reflects primarily the scattering properties of the medium, strong scattering being associated with significant broadening of the seismogram envelope. A remarkable example has been provided by Takahashi *et al.* (2007)

who showed that the peak delay time increases drastically when the direct *S*-wave path between source and station intersects the quaternary volcanoes in northern Japan. Strong scattering associated with small-scale heterogeneities is the primary explanation for the observed broadening of the seismogram envelope in this case.

The coda quality factor Q_c , which quantifies the decay rate of scattered arrivals forming the coda of local earthquakes (Aki & Chouet 1975), is yet another easily accessible parameter which contains information on the attenuation structure of the lithosphere. Although the physical interpretation of Q_c is still debated (Hoshihara 1991; Gusev 1995; Margerin *et al.* 1999; Calvet & Margerin 2013), this parameter is known to depend on the scattering and/or absorption quality factors of the medium, and displays clear lateral variations at the continental scale (Singh & Herrmann 1983; Jin & Aki 1988). In a recent study, Carcolé & Sato (2010) have provided

maps of Q_c for Japan revealing the spatial variations of this parameter with an unprecedented level of details. They also found that the spatial dependence of Q_c is very well correlated with fine-scale lateral variations of the intrinsic quality factor of shear waves deduced from radiative transfer modelling of the space–time energy distribution in the coda.

In a completely different geological context, Calvet *et al.* (2013) have mapped sharp lateral variations of Q_c and of the peak delay time along the Pyrenean range. The western part of the Pyrenees, where the broadening of the seismogram envelope of local earthquake is particularly large, is also characterized seismically by a blockage of the L_g waves (Chazalon *et al.* 1993). The latter phenomenon has been successfully explained by the presence of a localized zone of enhanced scattering and absorption, which might be explained geologically by the mixing of sedimentary and mantle rocks during the formation of the range (Sens-Schönfelder *et al.* 2009). From these recent observations, we conjecture that spatial variations of scattering and absorption in the lithosphere are ubiquitous and may provide meaningful information on the local geological structure. From our ability to provide high resolution, accurate maps of scattering and absorption will depend to a large extent the possibility to better delineate interesting geological features, possibly not seen by other geophysical methods.

The purpose of the present work is to provide a simple theoretical framework to calculate the impact of local perturbations of scattering and absorption properties on the energy envelopes of seismograms. To achieve this goal, we will follow the classical tomographic approach as summarized by Nolet (2008) and derive linearized relations between a given seismic observable—the intensity in the coda (e.g.)—and the governing physical parameters—the scattering and absorption times (or quality factors). These relations take the form of space integrals and depend, in turn, on a so-called sensitivity kernel which quantifies the perturbation of the detected intensity induced by a local perturbation of the propagation properties. Because coda waves are composed primarily of scattered waves, radiative transfer theory will be used as the basic physical model to derive the sensitivity kernels. To clarify our angle of attack and see how it differs from previous investigations, it is worthwhile to summarize briefly the tools developed by seismologists to map the scattering and absorption properties in the lithosphere. While some approaches make use of the spatiotemporal distribution of the energy in the coda, others focus more specifically on the peak delay time of shear waves. We will begin by reviewing the latter first.

Using a multiple low-angle scattering approach, Gusev & Abubakirov (1999a) showed that the peak delay time of S wave may be approximated by a line integral of the effective turbidity weighted by a simple function of the curvilinear abscissa along the ray path connecting the source to the station. We recall that the inverse effective turbidity, also known as the transport mean free path quantifies the typical distance after which a beam of energy has lost memory of its initial direction of propagation in a random inhomogeneous medium. This parameter controls the broadening of seismogram envelopes and also shows up in the diffusion constant of multiply scattered waves. The simplicity of the sensitivity kernel, which consists of a (weighted) delta function along the direct ray, is an attractive feature of this method. The approach of Gusev & Abubakirov (1999a) has been supported by numerical simulations of the radiative transfer equation, and applied to data from Kamtchatka to obtain a vertical profile of effective turbidity (Gusev & Abubakirov 1999b). From this study, the authors inferred a large contrast of turbidity between crust and mantle, the latter being much more transparent than the former.

A different approach to the peak delay time is provided by the Markov approximation, which is yet another form of multiple forward scattering model. It can be derived by appropriate ensemble averaging techniques from the parabolic wave equation and assumes that the waves propagate mostly in the forward direction on their way from source to station (Sato 1989; Saito *et al.* 2002). This sophisticated model is particularly attractive because it provides constraints on the power spectrum of heterogeneities, which quantifies the distribution of velocity fluctuations over different scale lengths. In particular, by combining observations of the peak delay time in different frequency bands, it is possible to infer the richness in small-scale heterogeneities of the propagation medium. It should be noted that reasonable guesses for the correlation distance and frequency dependence of the intrinsic quality factor are necessary to actually determine the power spectrum from the observed peak delay times. Once these quantities have been fixed, all the parameters that quantify the scattering such as the effective turbidity can be calculated exactly. It can therefore be considered as a method to map the scattering properties of the medium, although the relation is not direct. As remarked above, the peak delay time may also be influenced by the 3-D absorption structure, which may bias the estimate of the scattering parameters in certain circumstances. Using a recursive formula for the peak delay time in laterally varying random media derived by Takahashi *et al.* (2008), Takahashi *et al.* (2009) developed a new inversion scheme validated by numerical simulations and obtained detailed maps of the heterogeneity power spectrum in North-Eastern Japan for three depth ranges (0–20, 20–40 and 40–60 km). In this approach, the sensitivity is concentrated along the direct ray path connecting the source to the station. Let us emphasize again that the end result—a map of the spatial variations of the heterogeneity power spectrum—contains rich information on the statistical properties of the heterogeneities. More recently, an improved version of this tomographic method has been applied by Takahashi *et al.* (2011) to the mapping of inhomogeneities in the northern Izu-Bonin arc.

We pursue our overview of general approaches to map the attenuation properties of the lithosphere by considering techniques that exploit the coda of the seismogram. Nishigami (1991) devised a method to invert for the scattering properties of the lithosphere by considering the deviation of individual envelope records from a master curve. The master curve is obtained by fitting the overall decay of the coda of local earthquakes with a simple algebro-exponential formula of the form $t^{-2}e^{-\alpha t}$, and is supposed to represent adequately the average scattering properties of the region under study. The observed intensity residuals between the reference curve and the data are interpreted in terms of a 3-D scattering structure, which implicitly assumes that the intrinsic quality factor is spatially homogeneous. To map the scattering properties, Nishigami (1991) further assumes that scattering is isotropic and that the coda is dominated by singly scattered waves. This, in turn, implies that the sensitivity is concentrated on revolution ellipsoids with foci located at the source and station and great axis ct , with t the lapse-time in the coda. By considering a sufficiently large number of station pairs and different time windows in the coda, it is then possible to infer the 3-D perturbations of the turbidity (inverse mean free path). This method has been applied by Nishigami (2000) to unravel the complex pattern of heterogeneity around the San-Andreas fault. An extension to elastic waves that uses dense seismic arrays and the polarization information has later been proposed by Taira & Yomogida (2007) and applied by Taira *et al.* (2007) to image crustal heterogeneities around the Nagamachi-Rifu fault in Japan. There are yet other methods which map scatterers in the lithosphere using

more deterministic models of wave propagation (see, e.g. Bostock & Rondenay 1999), but they will not be discussed in this paper because our approach is inherently stochastic.

Xie & Mitchell (1990) developed a method to map lateral variations of Q at the continental scale using measurements of the coda quality factor of Lg waves Q_c^{Lg} . In their approach, the spectral stacking technique of Xie & Nuttli (1988) is applied to the whole Lg coda to reduce the data variance and obtain reliable Q_c^{Lg} measurements. It is also assumed that these measurements are representative of the total Q of the Lg wavetrain Q^{Lg} . The target region is divided up into cells where Q^{Lg} is assumed to be constant. For a given source station configuration and maximum lapse-time in the coda t_{\max} , a single-scattering ellipse with its foci at the location of the source and station and great axis ct_{\max} (c the average shear wave velocity in the crust) is constructed at the surface of the Earth. The contribution of each particular cell to a given Q_c^{Lg} measurement is taken proportional to the intersection area between the ellipse and the cell. In other words, the sensitivity of Lg coda waves is supposed to be homogeneously distributed inside the single-scattering ellipse. Because the typical maximal lapse-time t_{\max} is of the order of 300 s, the lateral resolution of the derived Q maps is of the order of 1000 km. This technique has been applied in various regions of the world to obtain maps of Q^{Lg} , which have been interpreted in terms of geological and tectonic activity, as summarized in Mitchell (1995) and Mitchell & Cong (1998).

Note that the approach of Xie & Mitchell (1990) does not distinguish between scattering and absorption quality factors and therefore provides constraints on the total Q only. Let us also remark that both Nishigami's method and peak delay time tomography rely on the strong assumption that absorption is either homogeneous or negligible with respect to scattering. Clearly, peak delay maps are not completely independent from the lateral variation of Q . A strong absorption anomaly may significantly shift the maximum of the seismogram envelope towards short lapse-time and be misinterpreted as a low turbidity anomaly. Analogous biases are expected in the approach of Nishigami. This motivates the developments of methods capable of separating scattering from absorption.

Although it cannot be considered as a genuine tomographic method, the multiple lapse time window analysis (MLTWA) is worth mentioning in this short review because it is the only method that allows separation of scattering from absorption (Fehler *et al.* 1992; Hoshiya 1993). In this approach, the spatial distribution of energy in the coda is estimated in three consecutive time windows. Their duration is typically of the order of 15 s and the first window includes the ballistic pulse propagating between source and station. The spatiotemporal energy distribution is modelled using the radiative transfer equation for isotropic scattering which allows the retrieval of the scattering mean free path and absorption length in the medium as a function of frequency. By appropriately regionalizing the data, it is possible to obtain maps of scattering and absorption parameters as illustrated in the paper of Carcolé & Sato (2010) for Japan. The modelling procedure developed in the next section combines the basic idea of Nishigami (1991) with the theoretical approach underpinning the MLTWA.

2 THEORY

2.1 Overview of theoretical approaches

In this section, we aim at predicting the perturbation of intensity induced by general (weak) spatial variations of scattering and

absorption properties superposed upon a homogeneously scattering and absorbing background. This is a problem of general interest which has received considerable attention in other fields of physics. It is therefore worthwhile to give an overview of the methods which have been proposed in the past to calculate intensity perturbations in non-homogeneous scattering and absorbing media to place our work in an interdisciplinary context.

A general framework to calculate the perturbation of intensity caused by a local variation of scattering/absorption properties is provided by the diagram method. A detailed exposition of diagrammatic expansions goes well beyond the scope of this paper. The interested reader is referred to the review article by van Rossum & Nieuwenhuizen (1999). In seismology, this method has been employed to calculate the multiple scattering of seismic waves using local coupled-modes (Park & Odom 2005) or the diffusion of coupled P and S waves (Margerin 2013). The idea of the method is to represent a change of scattering/absorption properties by the addition (or subtraction) of a single scatterer/absorber (Nieuwenhuizen & van Rossum 1993). This technique is very general and can be used to calculate intensity perturbations, but also more general quantities such as the two-point correlation function of the wavefield. Pioneering works have been done using this approach by Feng & Sornette (1991) in the field of acoustical, non-destructive evaluation of heterogeneous media, and by Nieuwenhuizen & van Rossum (1993) in the field of optics of dense media.

Because the exact evaluation of diagrams is a difficult task, one generally assumes that the spatiotemporal distribution of the energy inside the medium is smooth, which considerably simplifies the calculations. When the smoothness condition applies, a diffusion equation can be employed to describe the propagation of energy in the medium, which offers a less general but much more straightforward way of calculating the perturbation of intensity in a non-homogeneous scattering/absorbing medium. This approach has particularly been well developed in the field of optical tomography applied to medical imaging, where the mapping of absorption and scattering coefficients of infrared light inside the human body is a central question. In this field, linearized relations between the detected intensity and spatial variations of propagation properties have been derived in the diffusion approximation in the early nineties by Arridge *et al.* (1991). The kernel of the linear operator relating the medium perturbations to the measurements has been termed 'photon measurement density function', or 'sensitivity function' in short (Arridge 1995). Detailed derivations of stationary, frequency-dependent and time-dependent sensitivity functions for optical tomography in the diffusion approximation can be found in the review article by Arridge (1999).

While the diffusion approximation usually performs extremely well in medical imaging, it is generally a rather poor approximation to the propagation of high-frequency seismic waves in the crust at the notable exception of volcanic areas (Wegler & Lühr 2001; Wegler 2004). Even in the latter context, it is not possible to completely neglect the energy transported by the coherent wave, which is not described by the diffusion approximation. Coherent propagation plays an important role because seismic sources are embedded inside the target medium. Hence, perturbations of scattering/absorption properties which are located at less than one mean free path from the source (or receiver) can interact with the coherent wave and leave an imprint in the coda. This point will be clearly illustrated in Section 3. Radiative transfer provides a general framework to model simultaneously the coherent and incoherent (or diffuse) parts of the high-frequency seismic wavefield and has also been introduced in medical imaging to model the propagation

of photons in the most weakly scattering parts of the human body. Dorn (1998, 2000) has derived theoretical expressions for the sensitivity functions of diffuse optical tomography using an adjoint formalism for the time-dependent radiative transfer equation. His results are tailored to the experimental conditions encountered in medical imaging, and are therefore not directly applicable to seismology. In this work, we employ a straightforward Green's function method to derive sensitivity functions adapted to our purposes. In particular, we take into account the fact that the sources and receivers are point-like, omni-directional and embedded inside the propagation medium. Another notable difference between our approach and the one usually adopted in diffuse optical tomography lies in the fact that we treat explicitly the role of the coherent wave. Using the solution of the time-dependent solution of the equation of transfer derived by Paasschens (1997), this allows us to study analytically the singularities of our sensitivity functions (see the next section). The correct handling of these singularities is of particular importance in the seismological context as we demonstrate below.

2.2 Transport theory

To model the transport of energy in a scattering and absorbing medium, we introduce the radiative transfer equation satisfied by the specific intensity $I(\mathbf{r}, \hat{\mathbf{n}}, t)$:

$$\begin{aligned} (\partial_t + c\hat{\mathbf{n}} \cdot \nabla) I(\mathbf{r}, \hat{\mathbf{n}}, t) &= - \left(\frac{1}{\tau(\mathbf{r})} + \frac{1}{t^a(\mathbf{r})} \right) I(\mathbf{r}, \hat{\mathbf{n}}, t) + \frac{1}{\tau(\mathbf{r})} \\ &\times \int_{S^d} p(\hat{\mathbf{n}}, \hat{\mathbf{n}}') I(\mathbf{r}, \hat{\mathbf{n}}', t) d\hat{\mathbf{n}}' + S(\mathbf{r}, \hat{\mathbf{n}}, t). \end{aligned} \quad (1)$$

The specific intensity quantifies the flux of energy directed around the unit vector $\hat{\mathbf{n}}$ at point \mathbf{r} and time t in a scattering medium. In this work, we consider only infinite 2-D or 3-D random media with constant background velocity c , and assume that $I(\mathbf{r}, \hat{\mathbf{n}}, t) = 0$ for $t < 0$. The quantity $\tau(\mathbf{r})$ denotes the spatially varying mean free time which controls the strength of the scattering in the heterogeneous medium. It is related to the more familiar scattering quality factor by the formula $Q_{sc}(\mathbf{r}) = \omega\tau(\mathbf{r})$. In the case of statistical homogeneity, the mean free time is exactly equal to the mean time between two scattering events. The absorption time $t^a(\mathbf{r})$ controls the rate at which energy is locally dissipated due to anelastic phenomena, and is related to the intrinsic quality factor by the formula $Q_i(\mathbf{r}) = \omega t^a(\mathbf{r})$. Scattering anisotropy is described by the phase function $p(\hat{\mathbf{n}}, \hat{\mathbf{n}}')$, which gives the probability that energy propagating in direction $\hat{\mathbf{n}}'$ be deflected into direction $\hat{\mathbf{n}}$. The phase function should obey the reciprocity relation $p(\hat{\mathbf{n}}, \hat{\mathbf{n}}') = p(-\hat{\mathbf{n}}', -\hat{\mathbf{n}})$ and, in the case of a rotationally invariant medium, is of the form $p(\hat{\mathbf{n}} \cdot \hat{\mathbf{n}}')$. Possible spatial variations of the scattering pattern will be ignored in this paper. The source of energy is encapsulated in the term $S(\mathbf{r}, \hat{\mathbf{n}}, t)$ which describes the flux injected in the medium in direction $\hat{\mathbf{n}}$ at point \mathbf{r} and time t . Finally, the symbol $\int_{S^d} d\hat{\mathbf{n}}'$ denotes an integral over the unit sphere of space directions in d -dimensional space ($d = 2, 3$).

Eq. (1) can be deduced at the phenomenological level from a local balance of energy as described in several treatises (Chandrasekhar 1960; Apresyan & Kravtsov 1996) and review articles (Margerin 2005). Mathematically sound derivations of the transport equations for a variety of wave phenomena can be found in the paper by Ryzhik *et al.* (1996). In seismology, radiative transfer has become

a standard tool to model the propagation of short-period seismic waves as reviewed in the book by Sato *et al.* (2012).

Following Case (1969), we introduce the Green's function of the radiative transfer equation, which physically corresponds to the intensity response to a point-like, uni-directional and instantaneous release of energy in the scattering and absorbing medium. This Green's function will be denoted by $G(\mathbf{r}, \hat{\mathbf{n}}; \mathbf{r}', \hat{\mathbf{n}}'; t)$ and is the solution to eq. (1) for the source term:

$$S(\mathbf{r}, \hat{\mathbf{n}}, t) = \delta(\mathbf{r} - \mathbf{r}_0) \delta(\hat{\mathbf{n}} - \hat{\mathbf{n}}_0) \delta(t), \quad (2)$$

where δ denotes the usual Dirac delta function. Some key properties of the Green's functions will be useful for our purposes. (1) The first one pertains to *non-absorbing media* only and is a simple reformulation of the energy conservation law which underlies transport theory:

$$\iint_{\mathbb{R}^d S^d} G(\mathbf{r}, \hat{\mathbf{n}}; \mathbf{r}_0, \hat{\mathbf{n}}_0; t) d\mathbf{r} d\hat{\mathbf{n}} = 1, \quad (3)$$

where the symbol $\int_{\mathbb{R}^d}$ denotes an integral over d -dimensional space. (2) The reciprocity theorem of transport theory takes the form:

$$G(\mathbf{r}_0, -\hat{\mathbf{n}}_0; \mathbf{r}, -\hat{\mathbf{n}}; t) = G(\mathbf{r}, \hat{\mathbf{n}}; \mathbf{r}_0, \hat{\mathbf{n}}_0; t). \quad (4)$$

Note the reversal of the directions of propagation $\hat{\mathbf{n}}$ and $\hat{\mathbf{n}}_0$ in this equation, reminiscent of the symmetry of the phase function in a reciprocal medium. (3) The formal solution to the boundary value problem of transport theory, that is, the solution to eq. (1) for a smooth source term S may be expressed as

$$I(\mathbf{r}, \hat{\mathbf{n}}, t) = \iiint_{\mathbb{R}^d S^d} G(\mathbf{r}, \hat{\mathbf{n}}; \mathbf{r}', \hat{\mathbf{n}}'; t - t') S(\mathbf{r}', \hat{\mathbf{n}}'; t') d\mathbf{r}' d\hat{\mathbf{n}}' dt'. \quad (5)$$

The interested reader is referred to Case (1969) for a derivation of these formulae and applications of the Green's function formalism in transport theory. Note that the solution (5) tends to 0 in the limit $t \rightarrow 0^+$. Hence, if the boundary value problem is supplemented with the initial condition $I(\mathbf{r}, \hat{\mathbf{n}}, 0^+) = I^{ic}(\mathbf{r}, \hat{\mathbf{n}})$, the term

$$\mathcal{I}(\mathbf{r}, \hat{\mathbf{n}}, t) = \iint_{\mathbb{R}^d S^d} G(\mathbf{r}, \hat{\mathbf{n}}; \mathbf{r}', \hat{\mathbf{n}}'; t) I^{ic}(\mathbf{r}', \hat{\mathbf{n}}') d\mathbf{r}' d\hat{\mathbf{n}}' \quad (6)$$

must be added to (5) to match the distribution of intensity at $t = 0^+$. The Green's function therefore propagates the system from its initial state to an arbitrary time t . Let us finally remark that if the Green's function of the transport equation is known in an absorption-free medium, the case of uniform absorption time t_0^a is immediately obtained by multiplying this Green's function by a factor e^{-t/t_0^a} , as can be verified from the transport equation (1). The energy conservation law must be amended accordingly.

2.3 Derivation of the sensitivity kernels

We now assume that 'spatial' variations of absorption and scattering properties are superposed upon a statistically homogeneous background with mean free time τ_0 and absorption time t_0^a and write:

$$\frac{1}{\tau(\mathbf{r})} = \frac{1}{\tau_0} + \delta\left(\frac{1}{\tau(\mathbf{r})}\right), \quad (7a)$$

$$\frac{1}{t^a(\mathbf{r})} = \frac{1}{t_0^a} + \delta\left(\frac{1}{t^a(\mathbf{r})}\right). \quad (7b)$$

The weak perturbation condition demands in addition that

$$\delta(1/\tau(\mathbf{r})), \delta(1/t^a(\mathbf{r})) \ll 1/\tau_0, 1/t_0^a. \quad (8)$$

Note that in our paper, the symbol δ does double duty. It represents either the Dirac delta function or the perturbation of a physical quantity. The correct interpretation should be clear from the context. Let us denote by $G_0(\mathbf{r}, \hat{\mathbf{n}}; \mathbf{r}_0, \hat{\mathbf{n}}_0; t)$ the Green's function of the transport equation in the reference medium with parameters τ_0 and t_0^a . Upon inserting the decomposition (7a)–(7b) into eq. (1), collecting all perturbative terms on the right-hand side, and applying the representation theorem (5), we obtain the following integral equation for the Green's function of the laterally varying medium:

$$\begin{aligned} G(\mathbf{r}, \hat{\mathbf{n}}; \mathbf{r}_0, \hat{\mathbf{n}}_0; t) &= G_0(\mathbf{r}, \hat{\mathbf{n}}; \mathbf{r}_0, \hat{\mathbf{n}}_0; t) \\ &+ \iiint_0^t G_0(\mathbf{r}, \hat{\mathbf{n}}; \mathbf{r}', \hat{\mathbf{n}}'; t-t') \delta\left(\frac{1}{t^a(\mathbf{r}')}\right) \\ &\times G(\mathbf{r}', \hat{\mathbf{n}}'; \mathbf{r}_0, \hat{\mathbf{n}}_0; t') d\hat{\mathbf{n}}' dt' dr' \\ &+ \iiint_0^t G_0(\mathbf{r}, \hat{\mathbf{n}}; \mathbf{r}', \hat{\mathbf{n}}'; t-t') \delta\left(\frac{1}{\tau(\mathbf{r}')}\right) \\ &\times \left[\int p(\hat{\mathbf{n}}', \hat{\mathbf{n}}'') G(\mathbf{r}', \hat{\mathbf{n}}''; \mathbf{r}_0, \hat{\mathbf{n}}_0; t') d\hat{\mathbf{n}}'' \right. \\ &\left. - G(\mathbf{r}', \hat{\mathbf{n}}'; \mathbf{r}_0, \hat{\mathbf{n}}_0; t') \right] d\hat{\mathbf{n}}' dt' dr'. \quad (9) \end{aligned}$$

Note that unless indicated, the spatial and angular domains of integration cover the full space and the whole sphere of directions, respectively. The limits of the time integrals will be specified throughout the paper. The formally exact eq. (9) will now be approximated and manipulated to obtain the desired sensitivity kernels of coda waves. (1) Following the standard idea of perturbation theory, we assume that the overall impact of the spatial variations of scattering and absorption is small, and therefore substitute G with G_0 in the right-hand side of eq. (9). This procedure is equivalent to the first-Born approximation in wave propagation problems (Rytov *et al.* 1989; Sato *et al.* 2012). It can also be seen as the first term of the Neumann series solution to integral equation (9). (2) Considering the double couple radiation pattern of earthquakes and the usual average over sources performed experimentally, it seems appropriate to integrate over $\hat{\mathbf{n}}_0$ to simulate an omni-directional point source. We will denote by $I(\mathbf{r}, \hat{\mathbf{n}}; \mathbf{r}_0; t)$ the outcome of this operation applied to the Green's function $G(\mathbf{r}, \hat{\mathbf{n}}; \mathbf{r}_0, \hat{\mathbf{n}}_0; t)$, after normalization by the area S^d of the unit sphere in space dimension d . Similar definitions apply to I_0 and G_0 . In 2-D, the function $I_0(\mathbf{r}, \hat{\mathbf{n}}; \mathbf{r}_0; t)$ is known analytically in the case of isotropic scattering (Paasschens 1997), which is important for the applications of the theory developed in the next section. (4) Since seismic sensors are omni-directional, a final integration over $\hat{\mathbf{n}}$ (without normalization) is likewise required to model seismic records. This operation yields the total intensities $I(\mathbf{r}; \mathbf{r}_0; t)$ (or $I_0(\mathbf{r}; \mathbf{r}_0; t)$) radiated by the unit source. After applying steps (1)–(4) to eq. (9), as well as the reciprocity theorem (4), we obtain the perturbation of intensity in the coda in the desired linearized form:

$$\begin{aligned} \delta I(\mathbf{r}; \mathbf{r}_0; t) &= \int K^a(\mathbf{r}; \mathbf{r}'; \mathbf{r}_0; t) \delta\left(\frac{1}{t^a(\mathbf{r}')}\right) dr' \\ &+ \int K^{\text{sc}}(\mathbf{r}; \mathbf{r}'; \mathbf{r}_0; t) \delta\left(\frac{1}{\tau(\mathbf{r}')}\right) dr', \quad (10) \end{aligned}$$

eq. (10) introduces the following absorption and scattering sensitivity kernels:

$$K^a(\mathbf{r}; \mathbf{r}'; \mathbf{r}_0; t) = -S^d \iint_0^t I_0(\mathbf{r}', -\hat{\mathbf{n}}'; \mathbf{r}; t-t') I_0(\mathbf{r}', \hat{\mathbf{n}}'; \mathbf{r}_0; t') d\hat{\mathbf{n}}' dt' \quad (11)$$

$$\begin{aligned} K^{\text{sc}}(\mathbf{r}; \mathbf{r}'; \mathbf{r}_0; t) &= S^d \iint_0^t I_0(\mathbf{r}', -\hat{\mathbf{n}}'; \mathbf{r}; t-t') \\ &\times \left[\int p(\hat{\mathbf{n}}', \hat{\mathbf{n}}'') I_0(\mathbf{r}', \hat{\mathbf{n}}''; \mathbf{r}_0; t') d\hat{\mathbf{n}}'' \right. \\ &\left. - I_0(\mathbf{r}', \hat{\mathbf{n}}'; \mathbf{r}_0; t') \right] d\hat{\mathbf{n}}' dt'. \quad (12) \end{aligned}$$

These kernels depend on the positions of the source, receiver, perturbation and on the lapse-time in the coda. Their calculation requires the knowledge of the full intensity distribution, including its angular part. A physical interpretation is that in a scattering medium, the description of all possible paths from source to receiver going once through an elementary volume dr' located at \mathbf{r}' requires the knowledge of the geometry of the paths, which is encapsulated in the angular dependence of the specific intensity. This point will be further clarified when we consider specific applications of formulae (11)–(12). Let us remark that the calculation of the sensitivity kernel requires the solution of two transport problems: one from the source to the perturbation and another from the receiver to the perturbation. Although we have not employed the adjoint formalism, the concept of transport–backtransport transpires in formulae (11)–(12) (see Dorn 2000, for details). Let us finally remark that if the phase function is isotropic, the kernel for scattering perturbations may be decomposed as

$$K^{\text{sc}}(\mathbf{r}; \mathbf{r}'; \mathbf{r}_0; t) = K^{\text{iso}}(\mathbf{r}; \mathbf{r}'; \mathbf{r}_0; t) + K^a(\mathbf{r}; \mathbf{r}'; \mathbf{r}_0; t), \quad (13)$$

where the kernel K^{iso} is defined as

$$K^{\text{iso}}(\mathbf{r}; \mathbf{r}'; \mathbf{r}_0; t) = \int_0^t I_0(\mathbf{r}; \mathbf{r}'; t-t') I_0(\mathbf{r}'; \mathbf{r}_0; t') dt'. \quad (14)$$

Up to the normalization factor $I_0(\mathbf{r}; \mathbf{r}_0; t)$, formula (14) has already surfaced in the literature, in the context of monitoring temporal variations from coda waves (Pacheco & Snieder 2005; Larose *et al.* 2010; Obermann *et al.* 2013; Planès *et al.* 2014). The validity of formula (14) (after proper normalization) to extract apparent velocity changes in an evolving medium will be discussed in Section 5.

2.4 Basic properties of the kernels

Since absorption removes energy from the system, the kernel K^a must be negative as is trivially verified from eq. (11). This kernel also satisfies the following sum rule:

$$\begin{aligned} \frac{1}{t} \int K^a(\mathbf{r}; \mathbf{r}'; \mathbf{r}_0; t) dr' &= -\frac{S^d}{t} \iiint_0^t I_0(\mathbf{r}', -\hat{\mathbf{n}}'; \mathbf{r}; t-t') \\ &\times I_0(\mathbf{r}', \hat{\mathbf{n}}'; \mathbf{r}_0; t') d\hat{\mathbf{n}}' dt' dr' \\ &= -\frac{1}{t} \int_0^t dt' \iint G_0(\mathbf{r}, \hat{\mathbf{n}}'; \mathbf{r}', \hat{\mathbf{n}}'; t-t') \\ &\times I_0(\mathbf{r}', \hat{\mathbf{n}}'; \mathbf{r}_0; t') d\hat{\mathbf{n}}' d\hat{\mathbf{n}}'' dr' \\ &= -I_0(\mathbf{r}; \mathbf{r}_0; t), \quad (15) \end{aligned}$$

which follows from eq. (6), the time invariance of the system and the uniqueness of the solution to the transport equation. The plausibility

of this result can be attested physically by the following thought experiment: consider an isotropic source which injects energy into the reference medium at point \mathbf{r}_0 and time $t = 0$; suppose we can stop the time evolution at an arbitrary time $t' < t$ and measure the specific intensity at every point of the medium; imagine we can restart the experiment and use as initial condition the measured intensity distribution $I(\mathbf{r}', \hat{\mathbf{n}}'; \mathbf{r}_0; t')$ (no additional source); let the system evolve during $t - t'$ and measure the total intensity at every point. The outcome of this experiment should be independent of t' , and give the same result as a measurement at time t of the intensity field radiated by the isotropic point source acting at \mathbf{r}_0 and time $t = 0$ (last line of eq. 15). The stop/restart process is expressed mathematically by the triple integral in the second line of eq. (15). In more mathematical words, this sum rule follows from the semi-group structure of the radiative transfer equation (Preisendorfer 1957). As an application of eq. (15), let us consider the addition of a uniform, weak perturbation of absorption $\delta(1/t^a)$ to the reference medium. Using eqs (10) and (15), we immediately deduce $I = I_0(1 - t\delta(1/t^a)) \approx I_0 e^{-\delta(1/t^a)t}$, as expected. The relation (15) will also be useful to test the numerical implementation of the kernels, as discussed in the next section.

We now deduce an important sum rule for the scattering sensitivity kernel from the conservation of energy in transport theory. Upon integration of K^{sc} over all detection points \mathbf{r} and application of eq. (3), one obtains:

$$\int K^{\text{sc}}(\mathbf{r}; \mathbf{r}'; \mathbf{r}_0; t) d\mathbf{r} = 0. \quad (16)$$

Eq. (16) demonstrates that the application of first-order perturbation theory to the transport equation conserves energy. Note that this sum rule does not apply in the case of a finite medium with absorbing boundary condition like in diffuse optical tomography, because energy leaks out of the medium in this case. The result (16) is in sharp contrast with the first-order Born approximation in wave propagation problems, which is known to violate the energy conservation law. A different sum-rule is obtained when we consider a spatially homogeneous change of the inverse scattering time $\delta(1/\tau)$. Such a change entails a perturbation of the intensity which may be calculated in two ways: (1) by integrating the scattering sensitivity kernel over all possible locations of the perturbation and (2) by substituting $1/\tau_0$ with $1/\tau_0 + \delta(1/\tau)$ in the Green's function $I_0(\mathbf{r}; \mathbf{r}_0; t)$ and using a Taylor expansion. Equating the results of methods (1) and (2) yields:

$$\int K^{\text{sc}}(\mathbf{r}; \mathbf{r}'; \mathbf{r}_0; t) d\mathbf{r}' = \frac{\partial I_0(\mathbf{r}; \mathbf{r}_0; t)}{\partial \tau^{-1}}, \quad (17)$$

where the dependence of I_0 on τ is implicit. An application of this sum rule will be given in the next section. Note that the same method applied to a perturbation of absorption yields eq. (15) again.

2.5 Large lapse-time asymptotics

In the limit of long lapse-time, it is possible to make supplementary assumptions on the angular dependence of the intensity which allow further simplifications of eqs (11)–(12). Because scattering tends to homogenize the distribution of energy in phase space, the specific intensity may be expanded in terms of its first two angular moments as follows (see, e.g. Akkermans & Montambaux 2007):

$$I_0(\mathbf{r}, \hat{\mathbf{n}}; \mathbf{r}_0; t) = \frac{1}{S^d} [I_0(\mathbf{r}; \mathbf{r}_0; t) + d\mathbf{J}_0(\mathbf{r}; \mathbf{r}_0; t) \cdot \hat{\mathbf{n}}], \quad (18)$$

where we have introduced the current vector:

$$\mathbf{J}_0(\mathbf{r}; \mathbf{r}_0; t) = \int_{S^d} I_0(\mathbf{r}, \hat{\mathbf{n}}; \mathbf{r}_0; t) \hat{\mathbf{n}} d\hat{\mathbf{n}}. \quad (19)$$

On the right-hand side of eq. (18), the first term represents the angular average of the intensity and the second is a small correction to isotropy ($J_0 \ll I_0$) describing the diffusive transport of intensity in space dimension d . Reporting the expansion (18) into eq. (11) and retaining the leading term only, we obtain:

$$\lim_{t \rightarrow +\infty} K^{\text{sc}}(\mathbf{r}; \mathbf{r}'; \mathbf{r}_0; t) = - \int_0^t I_0(\mathbf{r}; \mathbf{r}'; t - t') I_0(\mathbf{r}'; \mathbf{r}_0; t') dt'. \quad (20)$$

An alternative derivation of this result based on a diffusion model for the propagation of energy in the medium is outlined in Appendix A.

To derive the long lapse-time asymptotics of the scattering kernel, we proceed as above and insert eq. (18) into eq. (12). It can be seen that all terms containing the mean intensity cancel out, leaving only one term containing the product of two current vectors:

$$\lim_{t \rightarrow +\infty} K^{\text{sc}}(\mathbf{r}; \mathbf{r}'; \mathbf{r}_0; t) = d(1-g) \int_0^t \mathbf{J}_0(\mathbf{r}'; \mathbf{r}; t - t') \cdot \mathbf{J}_0(\mathbf{r}'; \mathbf{r}_0; t') dt', \quad (21)$$

where g denotes the mean cosine of the scattering angle, defined as

$$g = \int_{S^d} p(\hat{\mathbf{n}} \cdot \hat{\mathbf{n}}') \hat{\mathbf{n}} \cdot \hat{\mathbf{n}}' d\hat{\mathbf{n}}. \quad (22)$$

Note that we have assumed that the medium is statistically isotropic in the definition of g . As shown in Appendix A, the formulae (20)–(21) may also be established by application of first-order perturbation theory to the diffusion equation. The interested reader is referred to Arridge (1995, 1999) for further details. Because at long lapse-time, the current vector is supposed to be much smaller than the mean intensity, we conclude that the perturbations of intensity are asymptotically dominated by the effects of absorption. Formula (21) is also interesting because it shows that the sign of the kernel varies spatially depending on the relative orientations of the two current vectors. The key features of the sensitivity kernels will be further explored and described in the next section, in the case of 2-D isotropic scattering.

3 APPLICATION TO 2-D ISOTROPIC SCATTERING

As illustrated in the previous section, the calculation of the sensitivity kernels requires the knowledge of the Green's function of the radiative transfer equation, including the full angular dependence of the specific intensity. As is well known, the intensity that propagates in a scattering medium is composed of a coherent (or un-scattered) part, and a diffuse (or incoherent) part (see, e.g. Akkermans & Montambaux 2007). The word 'diffuse' refers here to the intensity which has been scattered at least once and does not imply any diffusion approximation. Because in seismic applications, the source and receiver are point-like and embedded in the medium, both the diffuse and coherent parts of the intensity are singular and contribute to the sensitivity kernels. In this work, we consider a simplified physical situation (isotropic scattering), but we proceed as far as we can in the analytical treatment of the singularities. We do so by explicitly separating the intensity into its coherent and incoherent parts. As a consequence of the spatial perturbations in the medium, these two terms are coupled and contribute to the sensitivity in the coda at long lapse-time. This approach is in sharp contrast with

the numerical treatment usually adopted in radiative-transfer-based optical tomography (Arridge & Schotland 2009).

Let us consider an isotropically scattering medium in two dimensions. In this simple model, a closed-form expression for the Green's function of the radiative transfer equation has been derived by Paasschens (1997), including the angular dependence of the specific intensity required for our purposes. From a more practical point of view, 2-D kernels may provide a first idea of the sensitivity of scattered surface waves to lateral variations of scattering and absorption properties. As shown by Paasschens (1997), the transport of specific intensity from source to station involves two terms:

$$I(\mathbf{SR}, \hat{\mathbf{n}}, t) = \frac{1}{2\pi} e^{-ct/l_0} \delta(\mathbf{SR} - ct\hat{\mathbf{n}})\theta(t) + \frac{\theta(ct - SR)}{2\pi l_0 (ct - \mathbf{SR} \cdot \hat{\mathbf{n}})} e^{\sqrt{c^2 t^2 / l_0^2 - SR^2 / l_0^2 - ct / l_0}}, \quad (23)$$

where \mathbf{SR} denotes the source–station position vector, t is the lapse-time in the coda, $l_0 = c\tau_0$ is the mean free path of the reference medium and $\hat{\mathbf{n}}$ is the propagation direction at the detection point. The symbols δ and θ represent the Dirac and Heaviside distributions, respectively. On the right-hand side of eq. (23), the first term describes the coherent field which is perfectly localized in time, space and propagation direction. This term decays exponentially fast and becomes negligible a few mean free paths away from the source. At these distances, most of the energy is transported diffusively, as described by the second term on the R.H.S. of eq. (23). Integrating over all space directions $\hat{\mathbf{n}}$ yields the total intensity received at R (Shang & Gao 1988; Paasschens 1997):

$$I(\mathbf{SR}, t) = \frac{e^{-ct/l_0}}{2\pi SR} \delta(ct - SR) + \frac{\theta(ct - SR)}{2\pi l_0 \sqrt{c^2 t^2 - SR^2}} e^{\sqrt{c^2 t^2 / l_0^2 - SR^2 / l_0^2 - ct / l_0}}. \quad (24)$$

To derive eq. (24), we have used the following decomposition of the delta function: $\delta(\mathbf{SR} - ct\hat{\mathbf{n}}) = \delta(ct - SR)\delta(\hat{\mathbf{S}}\hat{\mathbf{R}} - \hat{\mathbf{n}})/SR$ with $SR > 0$, and the property $\int_{2\pi} \delta(\hat{\mathbf{n}} - \hat{\mathbf{n}}_0) d\hat{\mathbf{n}} = 1$, where $\int_{2\pi}$ denotes an integral over all directions in the plane (see Paasschens 1997, for details). Note that by multiplying eqs (23) and (24) by the factor e^{-t/l_0^a} , one obtains the Green's functions of the radiative transfer equation in a scattering medium with constant absorption time t_0^a .

Armed with this analytical solution, we begin by examining the role of spatial variations of absorption.

3.1 Absorption sensitivity kernel

To facilitate the presentation of the results, we introduce non-dimensional variables $\bar{t} = t/\tau_0$, $\bar{\mathbf{R}}' = \mathbf{R}'/l_0$, $\bar{\mathbf{R}}_0 = \mathbf{R}_0/l_0$, where \mathbf{R}_0 (\mathbf{R}') denotes the source–perturbation (receiver–perturbation) position vector (see Fig. 1). As a consequence of the change of variables, the perturbation of absorption and scattering $\delta(1/t^a(\mathbf{r}))$ and $\delta(1/\tau(\mathbf{r}))$ are henceforth *normalized* by the inverse mean free time of the reference medium $1/\tau_0$. To minimize the length of formulae, we omit the exponential decay due to absorption in the reference medium, that is, we take $t_0^a \rightarrow \infty$. Note that this assumption only affects the overall amplitude of the kernels but not their spatial dependence. Inserting eq. (23) into eq. (11), one obtains:

$$K^a(\bar{\mathbf{R}}'; \bar{\mathbf{R}}_0; \bar{t}) = -\frac{1}{2\pi l_0^2} \int_{2\pi} \int_0^{\bar{t}} \left(e^{-(\bar{t}-\bar{t}')}\delta(\bar{\mathbf{R}}' + (\bar{t}-\bar{t}')\hat{\mathbf{n}})\theta(\bar{t}-\bar{t}') + \frac{e^{\sqrt{(\bar{t}-\bar{t}')^2 - \bar{R}^2 - (\bar{t}-\bar{t}')}\theta(\bar{t}-\bar{t}' - \bar{R}')}}{2\pi((\bar{t}-\bar{t}') + \bar{\mathbf{R}}' \cdot \hat{\mathbf{n}})} \right) \times \left(e^{-\bar{t}'}\delta(\bar{\mathbf{R}}_0 - \bar{t}'\hat{\mathbf{n}})\theta(\bar{t}') + \frac{e^{\sqrt{\bar{t}'^2 - \bar{R}_0^2 - \bar{t}'}\theta(\bar{t}' - \bar{R}_0)}}{2\pi(\bar{t}' - \bar{\mathbf{R}}_0 \cdot \hat{\mathbf{n}}')} \right) d\bar{t}' d\hat{\mathbf{n}}'. \quad (25)$$

In eq. (25), the integrand is composed of four terms which describe different paths from source to receiver going through the perturbation. Each term exhibits specific singularities which will be analysed separately.

3.1.1 Coherent–coherent term

We first consider the coherent propagation from source to perturbation and from perturbation to receiver. This term involves products of delta functions which facilitate the integration over $\hat{\mathbf{n}}'$ and \bar{t}' . The

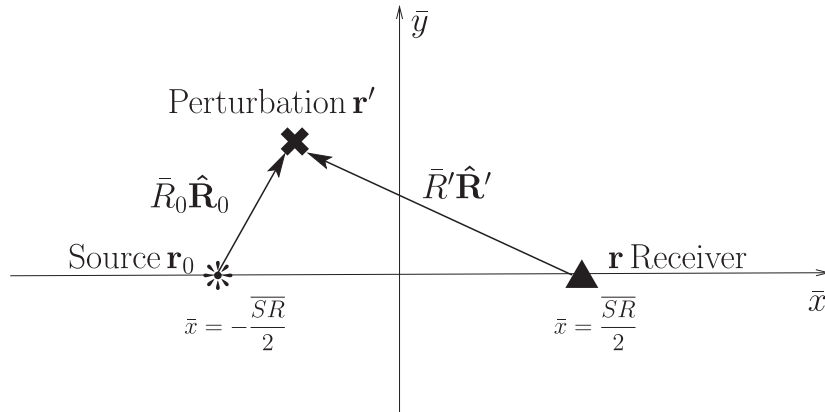


Figure 1. Geometry and notations used in the text. The source, receiver and perturbation position vectors are denoted by \mathbf{r}_0 , \mathbf{r} and \mathbf{r}' , respectively. To evaluate the kernels numerically, we introduce (non-dimensional) Cartesian coordinates (\bar{x}, \bar{y}) expressed in l_0 units, with $l_0 = c\tau_0$ the reference mean free path. In this coordinate system, the source is located at $(-SR/2, 0)$ and the receiver at $(SR/2, 0)$. Unit vectors are denoted with a hat.

end result may be put into two equivalent forms:

$$\begin{aligned} K_{cc}^a(\bar{\mathbf{R}}'; \bar{\mathbf{R}}_0; \bar{t}) &= -\frac{\theta(\overline{SR} - \bar{R}_0)\delta(\overline{\mathbf{SR}} - \bar{t}\hat{\mathbf{R}}_0)e^{-\bar{t}}}{2\pi l_0^2 \bar{R}_0} \\ &= -\frac{\theta(\overline{SR} - \bar{R}')\delta(\overline{\mathbf{RS}} - \bar{t}\hat{\mathbf{R}}')e^{-\bar{t}}}{2\pi l_0^2 \bar{R}'}, \end{aligned} \quad (26)$$

which emphasize the symmetry upon permutation of source and station, as required by reciprocity. To understand the physical meaning of the term (26), we calculate its effect on the detected intensity by considering a general perturbation of absorption $\delta(1/t^a(\mathbf{r}))/l_0$:

$$\delta I_{cc}^a = -\frac{\tau_0 \delta(\overline{SR} - \bar{t})e^{-\overline{SR}}}{2\pi l_0^2 \overline{SR}} \int_0^{\overline{SR}} \delta\left(\frac{1}{t^a(\bar{x}l_0 \mathbf{S}\bar{\mathbf{R}})}\right) d\bar{x}. \quad (27)$$

The perturbation (27) contributes exactly at the ballistic time and corrects the coherent intensity for the effect of absorption inhomogeneities along the direct ray connecting the source and the receiver. In the case of a constant perturbation of absorption, one obtains:

$$\delta I_{cc}^a = -\frac{\delta(SR - ct)e^{-SR/l_0}}{2\pi} \delta\left(\frac{1}{l^a}\right), \quad (28)$$

where dimensional variables have been restored and $l^a = ct^a$ denotes the absorption length. The result (28) may be verified by direct evaluation of the partial derivative of the coherent term of the reference solution (24) with respect to a perturbation of absorption. The coherent-coherent term does not affect the coda intensity and will not be discussed further.

3.1.2 Coherent-diffuse term

We now examine the contribution of the energy transported coherently (respectively, diffusely) from the source to the perturbation and diffusely (respectively, coherently) from the perturbation to the receiver. This coupling between coherent and diffuse waves is expressed as a sum of two terms:

$$\begin{aligned} K_{cd}^a(\bar{\mathbf{R}}'; \bar{\mathbf{R}}_0; \bar{t}) &= -\frac{1}{(2\pi l_0)^2} \left(\frac{e^{-\bar{t} + \sqrt{(\bar{t} - \bar{R}')^2 - \bar{R}_0^2}}}{\bar{R}'(\bar{t} - \bar{R}') + \bar{\mathbf{R}}_0 \cdot \bar{\mathbf{R}}'} \right. \\ &\quad \left. + \frac{e^{-\bar{t} + \sqrt{(\bar{t} - \bar{R}_0)^2 - \bar{R}'^2}}}{\bar{R}_0(\bar{t} - \bar{R}_0) + \bar{\mathbf{R}}' \cdot \bar{\mathbf{R}}_0} \right) \theta(\bar{t} - \bar{R}' - \bar{R}_0), \end{aligned} \quad (29)$$

whose symmetry reflects again the reciprocity at the level of the radiative transfer equation. A map view of the coherent-diffuse kernel is plotted in Fig. 2 (left column) for a source-station distance of one mean free path and three different lapse-times in the coda: $t = 2t_s, 3t_s, 4t_s$, with $t_s = \tau_0$ the propagation time of ballistic waves. The source and station are located on the horizontal axis at $\bar{x} = \pm 0.5$ and are depicted by black dots. The mapped data have been calculated as follows: the region of the plane $[-w, w] \times [0, w]$ is discretized on a 2-D grid of dimension $(2N + 1) \times (N + 1)$ delimiting $2N \times N$ pixels (N typically equals 100); the value of the kernel is evaluated at the centre of each pixel and stored in a matrix. Using the symmetry of the kernel with respect to reflection across the horizontal axis, the complete map is obtained. Note that this procedure avoids the evaluation of the kernel at its singular points. The discretized version of the kernel is subsequently normalized by assigning the absolute value 1 to the central pixel of the *total* kernel. In this way, the weight of the different contributions to the total sensitivity can be more easily analysed.

If we think of a crustal mean free path of the order of 100 km, the spatial and temporal scale used in Fig. 2 is typical of coda detection

at local to regional distances. The coherent-diffuse term is always negative because absorption removes energy from the system. It vanishes outside the causality or single-scattering ellipse defined by the condition $R' + R_0 = ct$, and possesses an algebraic (integrable) singularity at the source and the receiver. To better appreciate the spatial dependence of the coherent-diffuse term, we show cross-sections of the kernel along and across the source-receiver axis in Fig. 3. Each plot has been obtained by evaluating the kernels at 1000 evenly distributed points and the values are clipped at the limits displayed on the vertical axes. The longitudinal cross-section reveals the singular behaviour of the coherent-diffuse term at the source and at the station, which results in a strong sensitivity around these two points. There exists some sensitivity perpendicular to the source-receiver axis. But because the coherent wave decays exponentially fast, the coherent-diffuse kernel cannot extend far from the source and receiver. This point is clearly illustrated in Fig. 4, where the absorption kernels are represented for $SR = 5l_0$ and lapse-times $t = 1.2t_s, 2t_s, 3t_s, t_s = 5\tau_0$. If we think of a mean free path of the order of a few kilometres, this spatiotemporal scale is typical of coda detection in volcanic regions. In this configuration, after a transient regime of expansion, the coherent-diffuse contribution stabilizes and displays two spots of enhanced sensitivity of radius one mean free path around the source and receiver.

3.1.3 Diffuse-diffuse term

We now examine the contribution of waves which propagate diffusely from source to perturbation and from perturbation to receiver. This diffuse-diffuse absorption kernel is given by the following integral:

$$\begin{aligned} K_{dd}^a(\bar{\mathbf{R}}'; \bar{\mathbf{R}}_0; \bar{t}) &= -\frac{1}{2\pi l_0^2} \\ &\times \iint_{2\pi} \frac{e^{-\bar{t} + \sqrt{(\bar{t} - \bar{t}')^2 - (\bar{R}')^2} + \sqrt{(\bar{t}')^2 - (\bar{R}_0)^2}} \theta(\bar{t}' - \bar{R}_0) \theta(\bar{t} - \bar{t}' - \bar{R}')}{(2\pi)^2 (\bar{t} - \bar{t}' + \bar{\mathbf{R}}' \cdot \hat{\mathbf{n}}') (\bar{t}' + \bar{\mathbf{R}}_0 \cdot \hat{\mathbf{n}}')} d\bar{t}' d\hat{\mathbf{n}}', \end{aligned} \quad (30)$$

which diverges logarithmically at the source and at the receiver. To disentangle the singularities and obtain a more symmetric expression, we perform a partial fraction expansion and subsequently introduce new variables $\bar{u} = \bar{t}'/\bar{R}'$ and $\bar{v} = (\bar{t} - \bar{t}')/\bar{R}'$. Taking into account the bounds on \bar{t} and \bar{t}' imposed by the product of Heaviside functions, we obtain:

$$\begin{aligned} K_{dd}^a(\bar{\mathbf{R}}'; \bar{\mathbf{R}}_0; \bar{t}) &= -\frac{1}{(2\pi l_0)^2} \int_{2\pi} \int_1^{\bar{t} - \bar{R}'_0} \frac{e^{-\bar{t} + \sqrt{(\bar{t} - \bar{u}\bar{R}_0)^2 - \bar{R}'^2} + \bar{R}_0 \sqrt{\bar{u}^2 - 1}}}{2\pi (\bar{t} - \bar{\mathbf{S}}\bar{\mathbf{R}} \cdot \hat{\mathbf{n}}') (\bar{u} - \bar{\mathbf{R}}_0 \cdot \hat{\mathbf{n}}')} \\ &\quad \times \theta(\bar{t} - \bar{R}_0 - \bar{R}') d\bar{u} d\hat{\mathbf{n}}' \\ &\quad - \frac{1}{(2\pi l_0)^2} \int_{2\pi} \int_1^{\bar{t} - \bar{R}'_0} \frac{e^{-\bar{t} + \sqrt{(\bar{t} - \bar{v}\bar{R}')^2 - \bar{R}_0^2} + \bar{R}' \sqrt{\bar{v}^2 - 1}}}{2\pi (\bar{t} - \bar{\mathbf{S}}\bar{\mathbf{R}} \cdot \hat{\mathbf{n}}') (\bar{v} + \hat{\mathbf{R}}' \cdot \hat{\mathbf{n}}')} \\ &\quad \times \theta(\bar{t} - \bar{R}_0 - \bar{R}') d\bar{v} d\hat{\mathbf{n}}'. \end{aligned} \quad (31)$$

The first term can be deduced from the second by reflection across the bisector of the source-station line segment \mathbf{SR} . In eq. (31), the angular integral may be performed analytically using contour integration as detailed in Appendix B. The remaining integrals over the variables \bar{u} and \bar{v} can be performed numerically. Maps of the

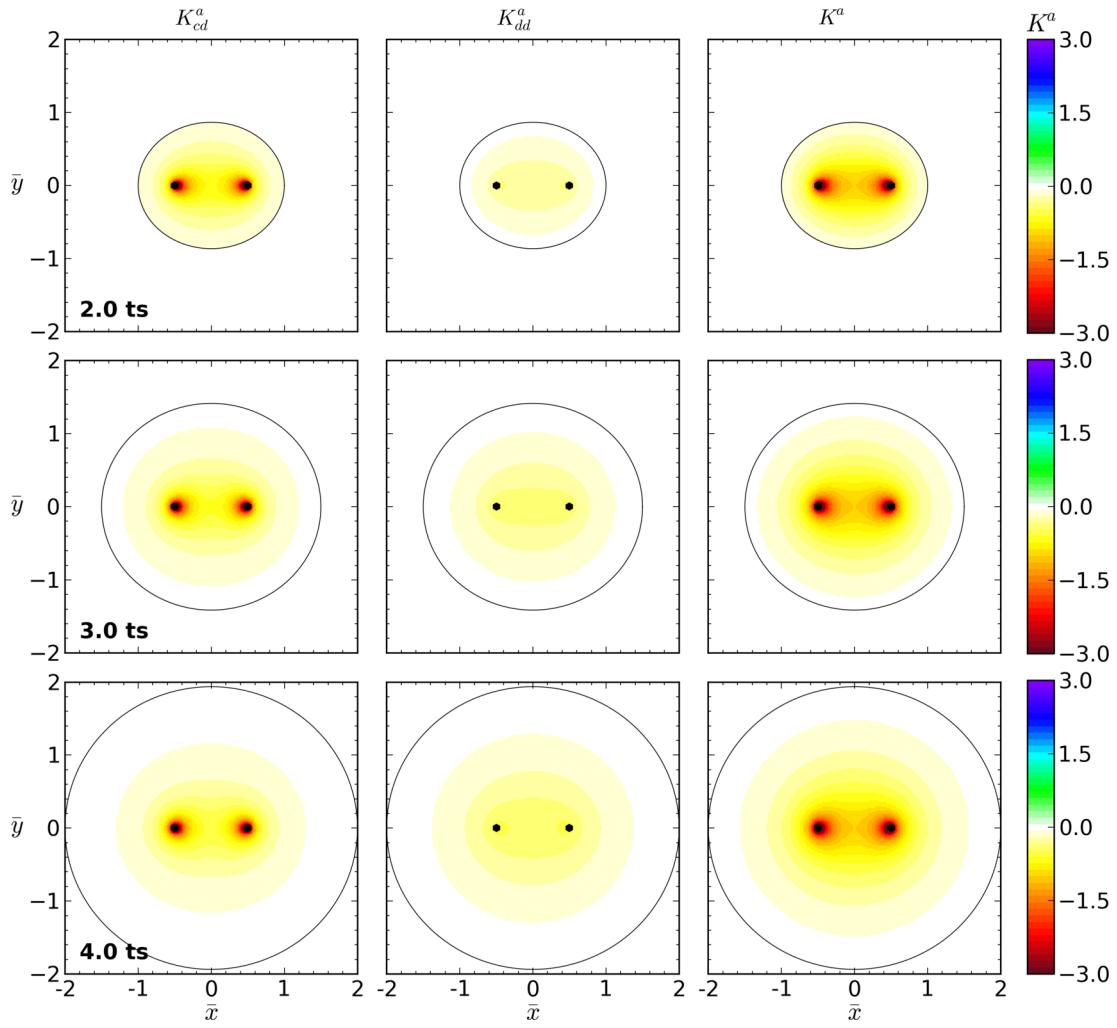


Figure 2. Colour maps of the absorption sensitivity kernels for source–station distance $SR = l_0$, and propagation times $t = 2t_s$ (top), $t = 3t_s$ (middle) and $t = 4t_s$ (bottom), with $t_s = \tau_0$ the propagation time of ballistic waves. Left: coherent–diffuse term; Centre: diffuse–diffuse term; Right: total sensitivity kernel. On the horizontal and vertical axes, the distances are expressed in mean free path units. The black ellipse delimits the causality domain outside which the kernels equal zero. The black dots indicate the position of the source and station. The kernels have been normalized so that the absolute value of the total sensitivity equals 1 at the midpoint of SR . To enhance the visibility, the colour scale has been saturated.

diffuse–diffuse absorption kernel are shown in Figs 2 and 4 for source–station distances of one and five mean free paths, respectively. These map views are complemented with longitudinal and transverse cross-sections in Figs 3 and 5. The diffuse–diffuse kernels display a zone of maximum sensitivity along the ray connecting the source and receiver with a slow (logarithmic) divergence at these two points. Figs 4 and 5 show the growth of the domain of influence of the diffuse–diffuse kernel with time, which is to be related to the expansion of the diffuse halo at a rate \sqrt{Dt} ($t \rightarrow \infty$, D the diffusion constant). The diffuse waves are therefore responsible for the sensitivity of coda waves at large distance (compared to the mean free path) from the source and station.

3.1.4 Total absorption kernel

The total absorption kernel is the sum of the three contributions discussed so far: $K^a = K_{cc}^a + K_{cd}^a + K_{dd}^a$. Let us first remark that all scattered wave paths have to propagate through a neighbourhood of the source and station, which provides a simple explanation for the divergence of the sensitivity at these two points. It is instructive to compare the role played by the different terms for different source–

station distances and different lapse-times in the coda. For $SR = l_0$, and t in the range $[2t_s, 4t_s]$ ($t_s = \tau_0$), the sensitivity of coda waves is dominated by the coherent–diffuse term. The diffuse–diffuse term adds some extra sensitivity in the bulk of the medium for propagation distances larger than the mean free path. Nevertheless, the zone of the highest sensitivity is localized around the direct ray connecting the source and receiver, which strongly suggests that local information on the absorption structure may be retrieved from the coda. For larger source–station distance ($SR = 5l_0$) and lapse-time in the range $([1.2t_s, 3t_s], t_s = 5\tau_0)$, a similar pattern emerges but the role played by the various terms is different. Interestingly, even at large lapse-time in the coda, the maximum sensitivity is still concentrated in a region of typical width one mean free path encompassing the source and the station. Except in the immediate vicinity of these two points, the sensitivity along and across the direct ray path is largely dominated by the diffuse–diffuse term.

3.2 Scattering sensitivity kernel

We pursue our investigations by analysing the sensitivity kernels for perturbations in the scattering strength $\delta(1/\tau(\mathbf{r}))/1/\tau_0$. We follow

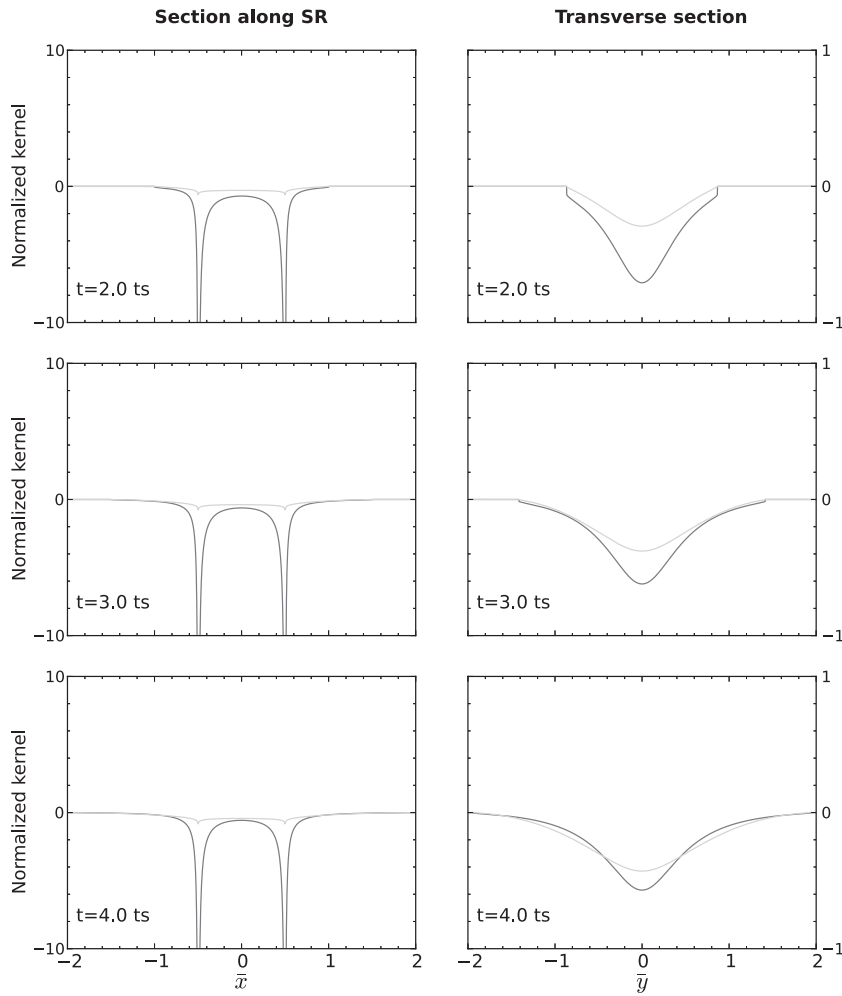


Figure 3. Cross-section of the absorption sensitivity kernels shown in Fig. 2. Left: along the source–receiver axis. Right: along the perpendicular bisector of SR. Black line: coherent–diffuse term. Grey line: diffuse–diffuse term. The kernels have been normalized so that the absolute value of the total equals 1 at the midpoint of SR.

the same approach as in the absorption section and study systematically the coupling between the coherent and diffuse terms of the Green’s function of the radiative transfer equation. As previously shown in eq. (13), the scattering kernel is the sum of the absorption and isotropic kernels, the latter being expressed as

$$\begin{aligned}
 K^{\text{iso}}(\bar{\mathbf{R}}'; \bar{\mathbf{R}}_0; \bar{t}) &= \frac{1}{(2\pi l_0)^2} \int_0^{\bar{t}} \left(\frac{e^{-(\bar{t}-\bar{t}')}}{\bar{R}'} \delta(\bar{t} - \bar{t}' - \bar{R}') \right. \\
 &\quad \left. + \frac{e^{\sqrt{(\bar{t}-\bar{t}')^2 - \bar{R}'^2} - (t-\bar{t}')\theta(\bar{t}-\bar{t}'-\bar{R}')}}{\sqrt{(\bar{t}-\bar{t}')^2 - \bar{R}'^2}} \right) \\
 &\quad \times \left(\frac{e^{-\bar{t}'}}{\bar{R}_0} \delta(\bar{t}' - \bar{R}_0) + \frac{e^{\sqrt{\bar{t}'^2 - \bar{R}_0^2} - \bar{t}'\theta(\bar{t}' - \bar{R}_0)}}{\sqrt{\bar{t}'^2 - \bar{R}_0^2}} \right) d\bar{t}'. \quad (32)
 \end{aligned}$$

The term ‘isotropic’ refers to the fact that only the angularly averaged part of the specific intensity appears in eq. (32). In the discussion that follows, we will emphasize the new singularities brought up by the isotropic part of the scattering kernel. Note that in the context of monitoring temporal variations from waveform changes in the coda, the kernel K^{iso} has recently been introduced by Planès *et al.* (2014).

3.2.1 Coherent–coherent term

The coherent–coherent kernel is the sum of the term (26) which takes into account the variation of the coherent intensity caused by scattering perturbations along the direct ray path and of the following contribution:

$$K_{\text{cc}}^{\text{iso}}(\bar{\mathbf{R}}'; \bar{\mathbf{R}}_0; \bar{t}) = \frac{1}{(2\pi l_0)^2} \frac{e^{-\bar{t}}}{\bar{R}' \bar{R}_0} \delta(\bar{t} - \bar{R}_0 - \bar{R}'), \quad (33)$$

which can be identified as a single-scattering correction. Indeed, this contribution has its sensitivity concentrated on the causality ellipse and corresponds to the coupling between two coherent propagators through a scattering event. This coherent–coherent kernel decays exponentially fast in the coda and becomes completely negligible after a few mean free times. Because it has the form of a Dirac distribution, the sensitivity can only be represented graphically after some smoothing has been applied. To give a realistic idea of its contribution to the total sensitivity in map view, we plot a discretized version of the delta function after averaging over an area of size one pixel. Such a representation is adequate as long as the scattering perturbations are smooth at this scale.

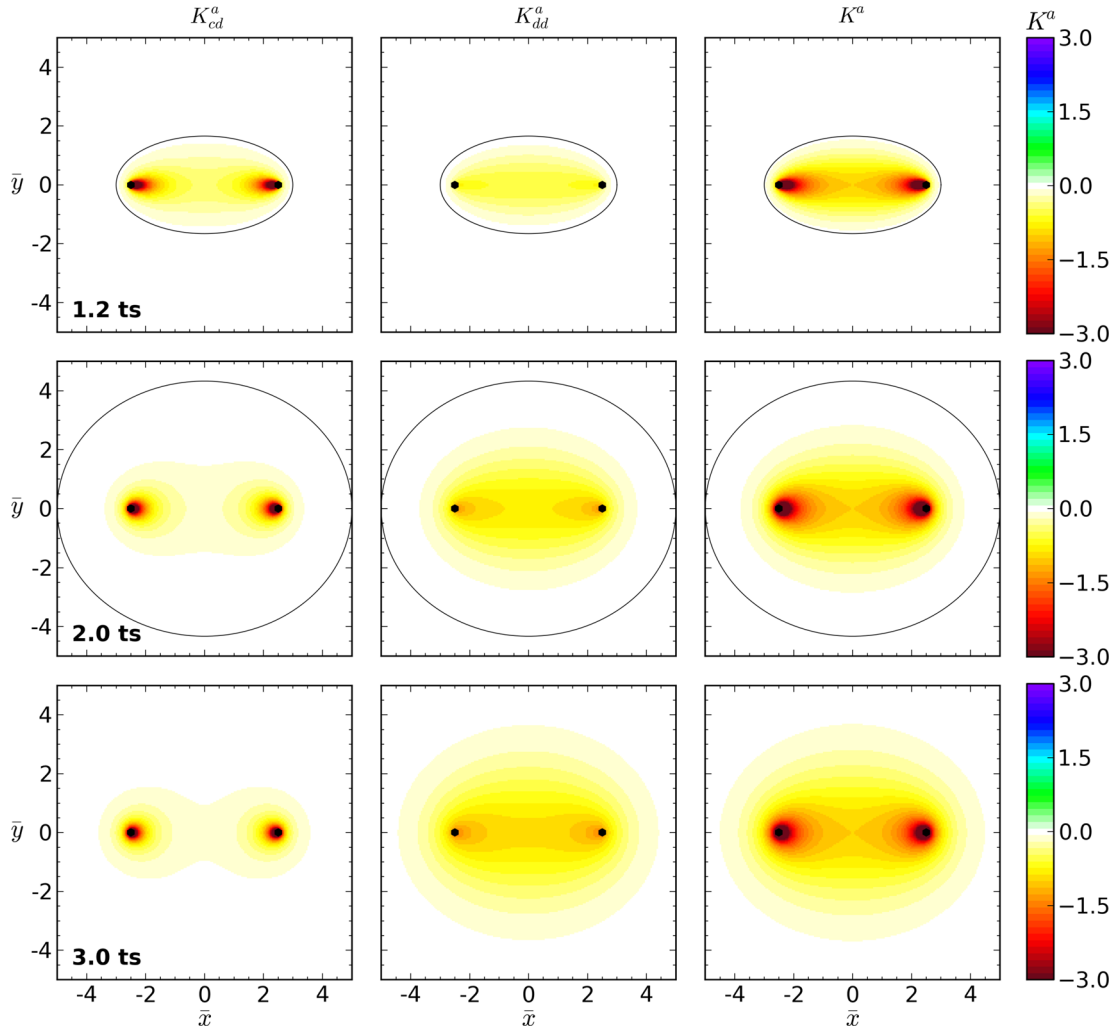


Figure 4. Colour maps of the absorption sensitivity kernels for source–station distance $SR = 5l_0$ and propagation times $t = 1.2t_s$ (top), $t = 2t_s$ (middle) and $t = 3t_s$ (bottom), with $t_s = 5\tau_0$ the propagation time of ballistic waves. Left: coherent–diffuse term. Centre: diffuse–diffuse term. Right: total sensitivity kernel. On the horizontal and vertical axes, the distances are expressed in mean free path units. The black ellipse delimits the causality domain outside which the kernels equal zero. The black dots indicate the position of the source and station. The kernels have been normalized so that the absolute value of the total equals 1 at the midpoint of SR . To enhance the visibility, the colour scale has been saturated.

3.2.2 Coherent–diffuse term

The coherent–diffuse kernel is the sum of the absorption term (29) and of the following term:

$$K_{cd}^{\text{iso}}(\bar{\mathbf{R}}'; \bar{\mathbf{R}}_0; \bar{t}) = \frac{1}{(2\pi l_0)^2} \left(\frac{e^{-\bar{t} + \sqrt{(\bar{t} - \bar{R}')^2 - \bar{R}_0^2}}}{\bar{R}' \sqrt{(\bar{t} - \bar{R}')^2 - \bar{R}_0^2}} + \frac{e^{-\bar{t} + \sqrt{(\bar{t} - \bar{R}_0)^2 - \bar{R}'^2}}}{\bar{R}_0 \sqrt{(\bar{t} - \bar{R}_0)^2 - \bar{R}'^2}} \right) \theta(\bar{t} - \bar{R}' - \bar{R}_0). \quad (34)$$

Like its absorption mate, the isotropic kernel (34) has an algebraic (integrable) singularity at the source and receiver. It exhibits an additional square-root-type singularity as one approaches the single-scattering ellipse from the inside, that is, in the limit $\bar{R}' + \bar{R}_0 \rightarrow \bar{t}^-$. This singularity corresponds to the coherent propagation of intensity from the source to a scattering perturbation located in the vicinity of the causality ellipse followed by diffuse propagation from the perturbation to the receiver after an additional scattering event. The coherent–diffuse scattering kernel (i.e. the sum of the isotropic and absorption parts) is shown in map view in Fig. 6 for a source–

station distance $SR = l_0$ and lapse-time $t = 2t_s, 3t_s, 4t_s, t_s = \tau_0$. The method adopted to obtain these maps is the same as in the absorption case. Fig. 6 illustrates that the coherent–diffuse scattering kernel is significantly more complex than its absorption counterpart. The divergence in the vicinity of the ellipse is clearly visible at short lapse-time and becomes fainter at longer lapse-time. This behaviour can be traced back to the exponential decay of the coherent term with the propagation distance. Cross-sections of the kernels along and across the direct ray path are also shown in Fig. 7. The square-root-type singularity is still apparent in the vicinity of the single-scattering ellipse in this figure.

The coherent–diffuse scattering kernel exhibits a zone of negative sensitivity of typical width one mean free path along the direct ray connecting the source and station. Inside this area, an increase of the scattering strength results in a decrease of the intensity received in the coda. Everything happens as if the extra-scattering plays the role of a screen which deflects part of the energy which would have otherwise propagated from source to station. Conversely, an extra scattering event adds some probability for waves propagating in a direction opposite to the direct ray path to be backscattered to the receiver. This gives rise to the lobes of high positive sensitivity

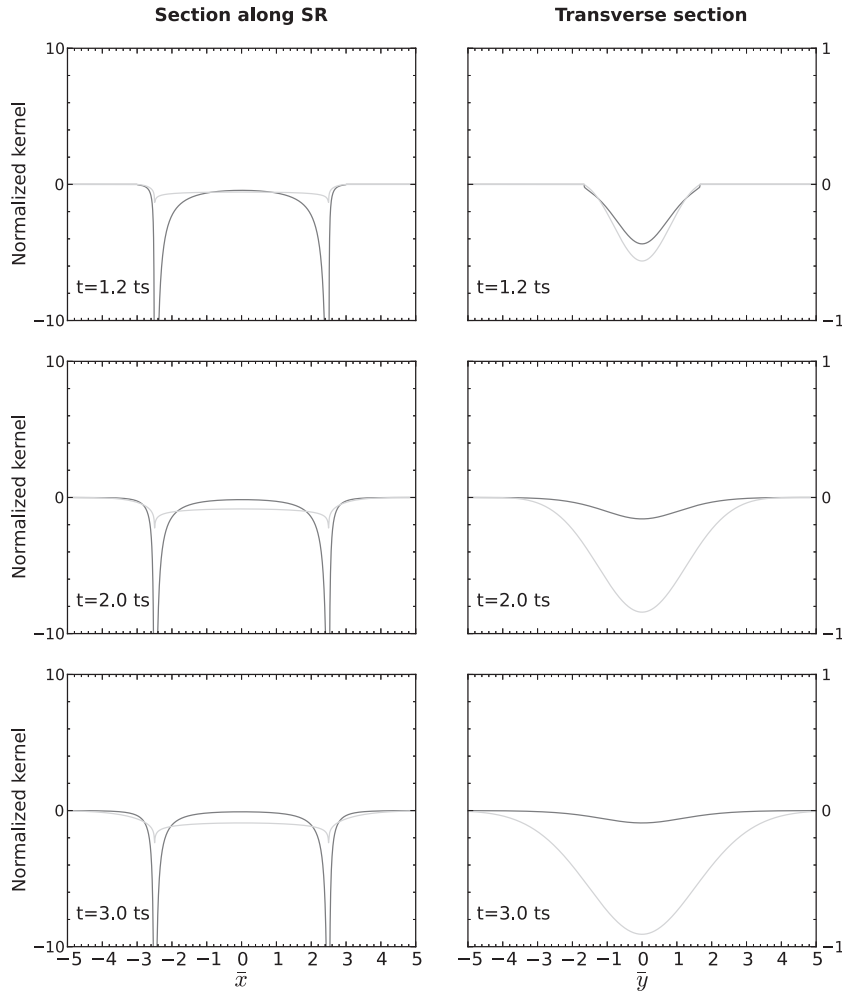


Figure 5. Cross-sections of the absorption sensitivity kernels shown in Fig. 4. Left: along the source–receiver axis. Right: along the perpendicular bisector of **SR**. Black line: coherent–diffuse term. Grey line: diffuse–diffuse term. The kernels have been normalized so that the absolute value of the total equals 1 at the midpoint of **SR**.

visible in Fig. 6. For larger source propagation distance $SR = 5l_0$, The coherent–diffuse kernel displays a strongly dipolar pattern with most of the sensitivity concentrated around the source and station as shown in Fig. 8. The singularity of the coherent–diffuse scattering kernel in the vicinity of the causality ellipse is strongly attenuated and becomes barely visible on the cross-sections (see Fig. 9).

3.2.3 Diffuse–diffuse term

We finally examine the role played by diffuse propagation from source to perturbation and from perturbation to receiver with an extra-scattering event taking place at the perturbation. This process is described by the following sum of two terms:

$$K_{\text{dd}}^{\text{iso}}(\bar{\mathbf{R}}'; \bar{\mathbf{R}}_0'; \bar{t}) = \frac{1}{(2\pi l_0)^2} \times \int_1^{\frac{\bar{t}-\bar{R}_0'}{\bar{R}_0'}} \frac{e^{-\bar{t}+\bar{R}_0'\sqrt{\bar{u}^2-1}+\sqrt{(\bar{t}-\bar{u}\bar{R}_0')^2-\bar{R}'^2}}}{\sqrt{\bar{u}^2-1}(\bar{R}_0'\sqrt{\bar{u}^2-1}+\sqrt{(\bar{t}-\bar{u}\bar{R}_0')^2-\bar{R}'^2})} \times \theta(\bar{t}-\bar{R}'-\bar{R}_0') d\bar{u} + \frac{1}{(2\pi l_0)^2}$$

$$\times \int_1^{\frac{\bar{t}-\bar{R}_0'}{\bar{R}'}} \frac{e^{-\bar{t}+\bar{R}'\sqrt{\bar{v}^2-1}+\sqrt{(\bar{t}-\bar{v}\bar{R}')^2-\bar{R}_0'^2}}}{\sqrt{\bar{v}^2-1}(\bar{R}'\sqrt{\bar{v}^2-1}+\sqrt{(\bar{t}-\bar{v}\bar{R}')^2-\bar{R}_0'^2})} \times \theta(\bar{t}-\bar{R}'-\bar{R}_0') d\bar{v}, \quad (35)$$

which have been obtained by following the same steps as outlined in the absorption section. Thus, the logarithmic divergences at the source and receiver have been separated out. Like in the absorption case, one term of the eq. (35) can be obtained from the other by reflection across the bisector of the source–receiver line segment. The diffuse–diffuse scattering kernel, that is, the sum of (31) and (35) is represented in Figs 6 and 8 for source–receiver distances $SR = l_0$, $5l_0$, respectively. The corresponding longitudinal and transverse cross-sections are shown in Figs 7 and 9. The diffuse–diffuse term exhibits a zone of negative sensitivity of typical width one mean free path around the direct ray path. In the long lapse-time limit, the sign of the kernel can be explained using the asymptotic relation (21). In this formula, everything happens as if both the source and receiver radiate energy into the medium. Then, the sign of the kernel depends on the scalar product between the energy current vectors of the two sources: the one placed at S , and the other at R . Clearly, this scalar product will be negative on the line segment **SR** because

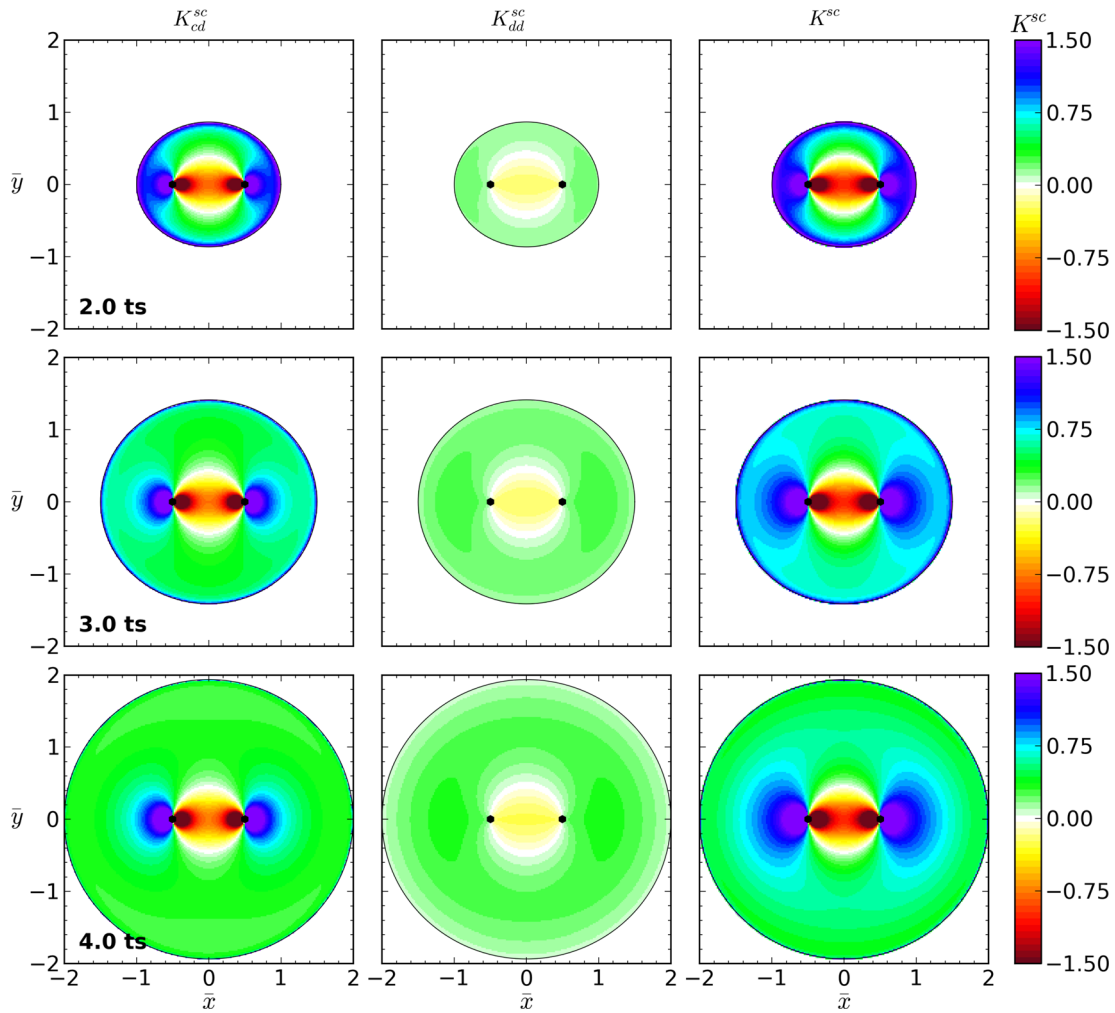


Figure 6. Colour maps of the scattering sensitivity kernels for source–station distance $SR = l_0$ and propagation times $t = 2t_s$ (top), $t = 3t_s$ (middle) and $t = 4t_s$ (bottom), with $t_s = \tau_0$ the propagation time of ballistic waves. Left: coherent–diffuse term. Centre: diffuse–diffuse term. Right: total (including the coherent–coherent part). On the horizontal and vertical axes, the distances are expressed in mean free path units. The black ellipse delimits the causality domain outside which the kernels equal zero. The black dots indicate the position of the source and station. The kernels have been normalized so that the absolute value of the total equals 1 at the midpoint of **SR**. To enhance the visibility, the colour scale has been saturated.

the energy fluxes of the two sources are in opposite directions at all times. Conversely, elsewhere on the line (**SR**), the energy flows away from the two sources in the same direction, hence the positive sign. The cross-sections of Figs 7 and 9 show the slow divergence of the diffuse–diffuse kernel at the source and station. Fig. 8 illustrates the expansion of this kernel with the lapse-time in the coda, which, like in the absorption case, may be related to the \sqrt{Dt} growth of the diffuse halo. Hence, the diffuse–diffuse kernel provides sensitivity to variations of the scattering strength in the bulk of the medium.

3.2.4 Total scattering kernel

We may now examine the relative contributions of the different terms composing the total scattering kernel: $K^{sc} = K_{cc}^{iso} + K_{cd}^{iso} + K_{dd}^{iso} + K^{abs}$. For $SR = l_0$ and relatively short lapse-time $t \in [2t_s, 4t_s]$, Fig. 7 shows that the sensitivity along the direct ray is largely dominated by the coherent–diffuse term. Across the direct ray, the coherent–diffuse term is still dominant but the order of magnitude of the diffuse–diffuse term becomes comparable after four mean free times. As shown in Fig. 6, the spatial patterns of the coherent–diffuse and total scattering kernel are very similar.

The most clearly visible contribution of the diffuse–diffuse term is the broadening of the positive lobes of sensitivity, as well as some additional sensitivity in the bulk of the medium (see Fig. 6). For larger source–station distance $SR = 5l_0$, the coherent–diffuse term plays a dominant role only in the vicinity of the source and receiver, as shown on the cross-sections of Fig. 9. The sensitivity across the direct ray path is largely controlled by the diffuse waves, except at early time in the coda ($t = 1.2t_s$). Like in the case of absorption, we remark that at long lapse-time in the coda, the sensitivity is highest in a domain of width one mean free path going from source to station but there is some additional complexity due to the changes of sign of the kernel.

3.3 Integrated sensitivity kernels

So far, we have focused the discussion on the spatial dependence of the kernels without paying attention to their overall amplitude. In this section, we examine the relative contributions of the different terms composing the scattering and absorption kernels by calculating their integrals over all possible positions of the perturbation. These integrated kernels give an idea of the sensitivity of

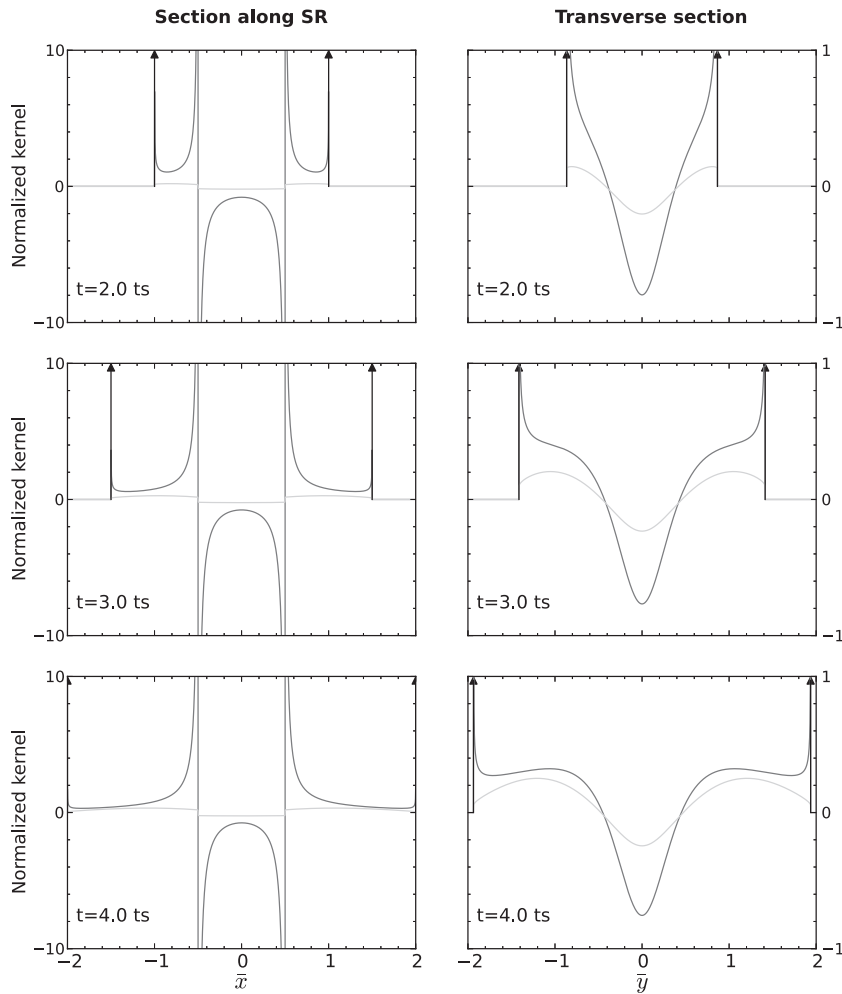


Figure 7. Cross-section of the scattering sensitivity kernels shown in Fig. 6. Left: along the source–receiver axis. Right: along the perpendicular bisector of **SR**. Black line: coherent–diffuse term. Grey line: diffuse–diffuse term. The arrows indicate the Dirac-type distribution on the single-scattering ellipse.

coda waves to spatial variations of scattering and absorption that are smooth at the scale of the area probed by the diffuse waves. Note that this area should typically grow linearly in time when the coherent waves dominate and like the square root of time at long lapse-time in the coda. The different terms of the integrated kernels are plotted in Fig. 10 for a source–receiver distance $SR = l_0$ (on the left) and for $SR = 5l_0$ (on the right). These results have been obtained by direct numerical integration of the sensitivity kernels, except for the coherent–coherent scattering term which can be obtained analytically. The sum rules (15) and (17) have been verified with a typical accuracy of five digits, which validates the numerical approximations. Independent of the source–receiver distance, we find that the absolute magnitude of the integrated kernels is always larger for absorption than for scattering. The single-scattering correction term becomes smaller in absolute value than all other terms after typically two mean free times, as anticipated. The time after which the diffuse–diffuse term exceeds the coherent–diffuse term depends slightly on the source–receiver distance SR and on the type of perturbation. In the case of scattering (respectively, absorption), the integrated sensitivity is dominated by the diffuse–diffuse contribution after $4\tau_0$ (respectively, $3\tau_0$) for $SR = l_0$ and $5.5\tau_0$ (respectively, $5.5\tau_0$) for $SR = 5l_0$. Finally, the change of sign of the integrated scattering kernels, depending on the source–receiver distance, is worth noting. Except for the coherent–coherent term which is always positive, the integrated scattering kernels become very

rapidly positive for $SR = l_0$, but are always negative for $SR = 5l_0$ (see Fig. 10). Our results suggest that as far as large-scale perturbations are concerned, the effects of absorption dominate over scattering in the coda.

4 IMPACT OF A LOCAL PERTURBATION ON THE ENERGY ENVELOPE OF CODA WAVES

In this section, we calculate the relative perturbations of the intensity in the coda induced by a localized perturbation of the scattering and/or absorption properties using the sensitivity kernels developed in Sections 2 and 3. The anomaly has the shape of a Gaussian of typical width σ , normalized such that its maximum equals 1/4. Note that by linearity, the calculations presented below can be rescaled to obtain the results for a perturbation of arbitrary magnitude ϵ . The main purpose of this section is to identify the signature of an anomaly of scattering and/or absorption properties based on the modification of the coda envelope with respect to a reference intensity master curve. This is essentially the idea underlying the work of Nishigami (1991, 2000). We extend his approach by considering the effects of multiple scattering and the role of absorption. In the calculations that follow, we consider two non-dimensional epicentral distances $\bar{SR} = 0.5$ and $\bar{SR} = 2$, respectively. To keep an eye

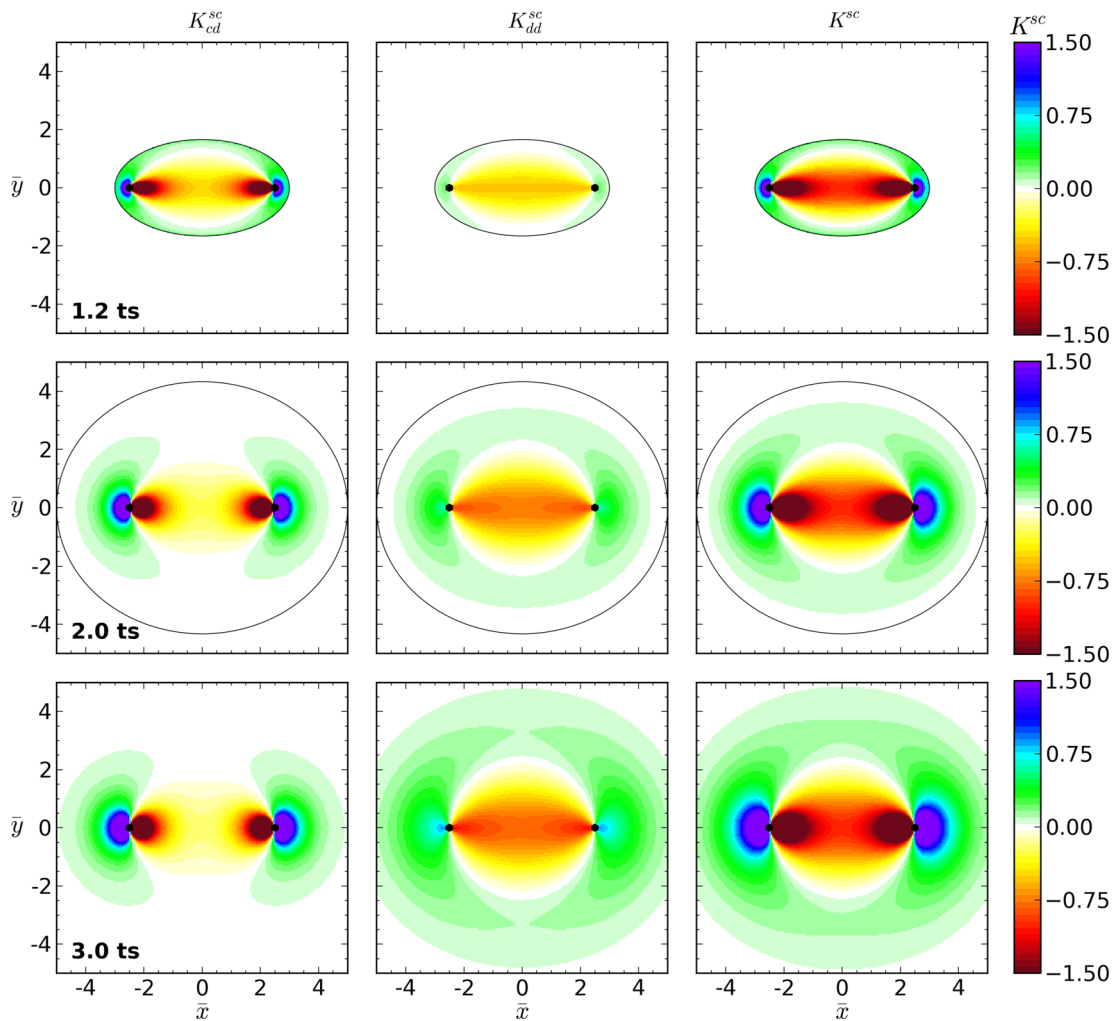


Figure 8. Colour maps of the scattering sensitivity kernels for source–station distance $SR = 5l_0$ and propagation times $t = 1.2t_s$ (top), $t = 2t_s$ (middle) and $t = 3t_s$ (bottom), with $t_s = 5\tau_0$ the propagation time of ballistic waves. Left: coherent–diffuse term. Centre: diffuse–diffuse term. Right: total (including the coherent–coherent part). On the horizontal and vertical axes, the distances are expressed in mean free path units. The black ellipse delimits the causality domain outside which the kernels equal zero. The black dots indicate the position of the source and station. The kernels have been normalized so that the absolute value of the total equals 1 at the midpoint of SR . To enhance the visibility, the colour scale has been saturated.

on future applications, the reader can think of a mean free path of the order of 100 km, which is a reasonable value for the crust around 5 Hz. The two epicentral distances $\overline{SR} = 0.5$ and $\overline{SR} = 2$ therefore correspond to local and regional detection of coda waves generated by crustal earthquakes.

4.1 Effect of the size of the anomaly

We first consider a scattering/absorption anomaly located at the midpoint of the direct ray connecting the source and station and examine four non-dimensional widths $\sigma = \{0.1, 0.2, 0.3, 0.4\}$. The relative intensity perturbation is plotted as a function of the time in the coda for $\overline{SR} = 0.5$ (left) and $\overline{SR} = 2$ (right) in Fig. 11. For both scattering and absorption, we observe that the overall intensity perturbation decreases with the epicentral distance and with the size of the anomaly. Suppose we are able to measure variations of average coda intensity of the order of 5 per cent, then our calculations indicate that a scattering (respectively, absorption) anomaly smaller than 0.2 (respectively, 0.1) mean free path will be almost undetectable in the coda. In other words, small-scale fluctuations of the mean free path and/or absorption length have very little impact

on the shape of the coda, which may partly explain its stability. Other remarkable features show up in Fig. 11. (1) The sign of the intensity perturbation caused by a scattering anomaly depends on the epicentral distance: It may switch from positive to negative as the source–station distance increases. (2) In most cases, absorption anomalies have a much longer-lasting effect on the intensity received in the coda than scattering anomalies. This, in turn, suggests that spatial variations of scattering/absorption should be looked for in the early/late coda, respectively.

4.2 Effect of the position of the anomaly

The observations made so far have been based on a rather specific configuration. In this section, we fix the size of the anomaly $\sigma = 0.2$ and vary its location with respect to the source and receiver. The maximum amplitude is taken equal to 1/4. In Fig. 12, we represent the perturbation of intensity as a function of lapse-time in the coda for two epicentral distances ($\overline{SR} = 0.5$, left; $\overline{SR} = 2$, right) and four positions of the anomaly on the bisector of SR ($\bar{x} = 0$, $\bar{y} = \{0, 0.25, 0.5, 1\}$). Fig. 13 examines the case where the centre of the anomaly is located on the line (SR), backwards from the

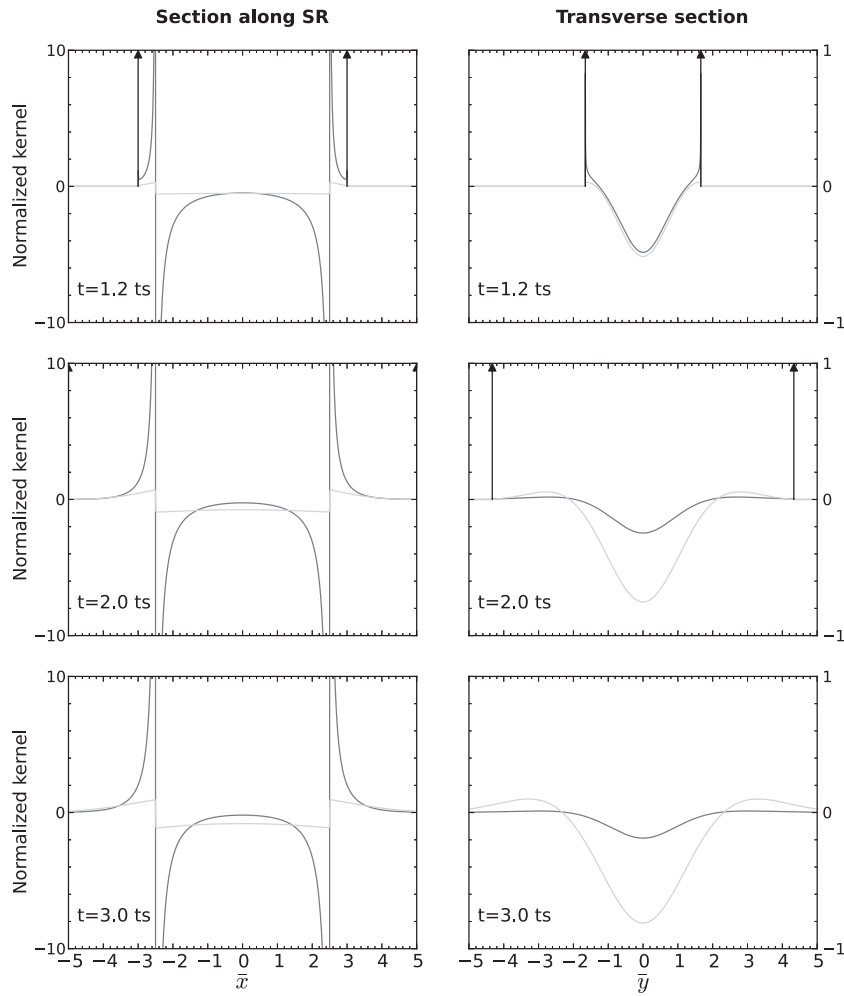


Figure 9. Cross-section of the scattering sensitivity kernels shown in Fig. 8. Left: along the source–receiver axis. Right: along the perpendicular bisector of SR. Black line: coherent–diffuse term. Grey line: diffuse–diffuse term. The arrows indicate the Dirac-type distribution on the single-scattering ellipse.

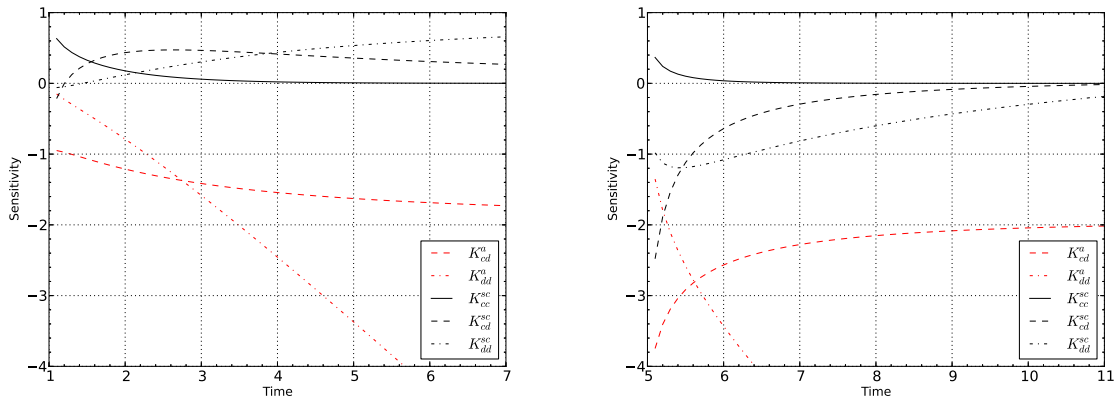


Figure 10. Integrated sensitivity kernels for absorption (red) and scattering (black) as a function of time. The inset shows the different line styles used to represent the different terms of the kernels. Left: source–receiver distance $\overline{SR} = 1$. Right: source–receiver distance $\overline{SR} = 5$. The sensitivities have been normalized by the common pre-factor $1/(2\pi l_0)^2$, with l_0 the mean free path in the unperturbed medium.

source ($\bar{x} = -\overline{SR}/2 - \{0, 0.25, 0.5, 1.0\}$). Note that the same figure would be obtained if the anomalies were flipped around the \bar{y} -axis. For both scattering and absorption anomalies, it is apparent from Figs 12 and 13 that the intensity perturbation decreases with the distance to the source either along or across the direct ray path, as well as with the epicentral distance. Below, we provide more specific descriptions for each kind of perturbation.

4.2.1 Scattering anomalies

We analyse the scattering anomalies first, because they give rise to maxima and/or minima which are easily identifiable on the relative intensity perturbation curves in both Figs 12 and 13. At short epicentral distance ($\overline{SR} = 0.5$), the time of the maximum t_m increases with the distance between the source and the anomaly but does not

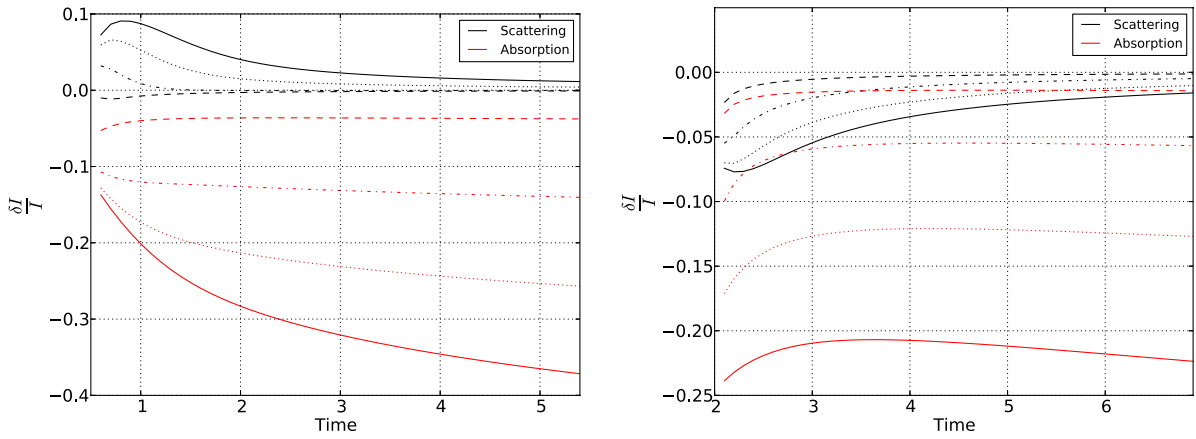


Figure 11. Relative intensity perturbation caused by a localized scattering (black) or absorption (red) anomaly. The anomaly has the shape of a Gaussian of width $\sigma = 0.1$ (dashed line), $\sigma = 0.2$ (dash-dotted line), $\sigma = 0.3$ (dotted line), $\sigma = 0.4$ (solid line) and maximum amplitude $1/4$. Left: epicentral distance $SR = 0.5l_0$. Right: epicentral distance $SR = 2l_0$.

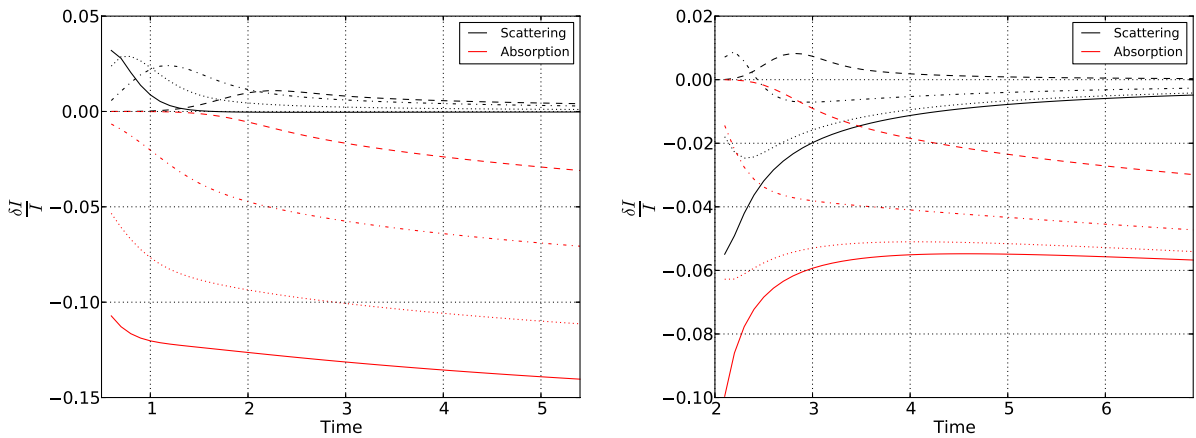


Figure 12. Relative intensity perturbation caused by a localized scattering (black) or absorption (red) anomaly whose centre is located at $\bar{y} = 0$ (solid line), $\bar{y} = 0.25$ (dotted line), $\bar{y} = 0.5$ (dash-dotted line) and $\bar{y} = 1$ (dashed line), on the bisector of SR . The anomaly has the shape of a Gaussian of width $\sigma = 0.2$ (dashed line) and maximum amplitude $1/4$.

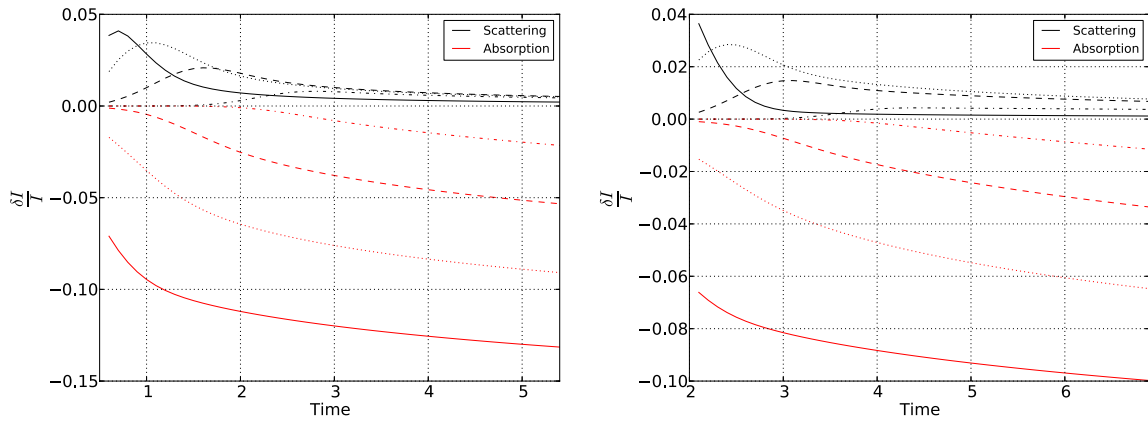


Figure 13. Relative intensity perturbation caused by a localized scattering (black) or absorption (red) anomaly whose centre is located at $\bar{x} = -\overline{SR}/2$ (solid line), $\bar{x} = -\overline{SR}/2 - 0.25$ (dotted line), $\bar{x} = -\overline{SR}/2 - 0.5$ (dashed line) and $\bar{x} = -\overline{SR}/2 - 1$ (dash-dotted line), on the line (SR) . The anomaly has the shape of a Gaussian of width $\sigma = 0.2$ (dashed line) and maximum amplitude $1/4$.

correspond to the time of flight of the ballistic wave t_b . In general, t_m is smaller than t_b , which implies that traditional migration based on the single-scattering approximation may underestimate the actual distance to the anomaly. In addition, we remark that for short epicentral distances, scattering anomalies located along, or perpendicular to the source–receiver line of sight, share very similar signatures. In

practice, this means that a combination of epicentral distances and source–station orientations is necessary to remove the ambiguity and correctly map the scattering properties of the target region. In the case of an anomaly located on the bisector of SR , additional complexity appears as the epicentral distance increases. A positive scattering anomaly may give rise to a negative intensity pulse, or

even entail a positive maximum followed by a negative minimum (see Fig. 12 right, $\bar{y} = 0.5$). The sign change is to be related to the temporal evolution of the sensitivity described in the previous section: at short time, the anomaly intersects the single-scattering ellipse in the vicinity of which the sensitivity is strongly positive, while at late time, the anomaly lies in the broad zone of negative sensitivity between the source and station. Because practical estimation of the coda intensity usually involves smoothing in the time domain, it is likely that the more complex signature of a scattering anomaly might be washed out in such cases.

4.2.2 Absorption anomalies

For short epicentral distances ($\overline{SR} = 0.5$), Figs 12 and 13 illustrate that the relative intensity perturbations caused by absorption anomalies depend generally smoothly on the lapse-time in the coda. In general, absorption anomalies do not yield clearly identifiable maxima but instead manifest themselves as a steady decrease of $\delta I/I$ with time. Hence, they mostly affect the decay rate of the intensity and therefore have a major impact on the apparent coda quality factor Q_c . In Fig. 13, it is also apparent that the epicentral distance does not play an important role when the anomaly is located on the line (SR), backwards from the source. Interestingly, while the magnitude of the intensity perturbation depends strongly on the position of the anomaly, the rate of decay of the intensity appears to be independent from this quantity at sufficiently long lapse-time [see Figs 12 (left) and 13 (left)].

For larger epicentral distance ($\overline{SR} = 2$) and an anomaly located on the bisector of SR , the impact on the intensity received in the coda is more contrasted. When the anomaly is located in the vicinity of the direct ray, after a transient regime of the order of one mean free time, the anomaly manifests itself as an almost time-independent drop of the relative intensity $\delta I/I$. Hence, such anomalies will have no impact on the coda decay and could instead be interpreted as a kind of ‘site effect’. However, its amplitude is so small that it will most likely be undetectable. The comparison of Figs 12 and 13 also reveals that absorption anomalies located at sufficiently large distance (typically half the mean free path) either perpendicular to the direct ray path or backwards from the source yield similar signature. Hence, the combination of different source–receiver pairs with various epicentral distances and backazimuths will be necessary to map an absorption anomaly in the region under study.

To conclude this section, we remark that the most prominent intensity variations caused by scattering/absorption anomalies occur at short lapse-time in the coda. It is well-known, since the paper of Aki & Chouet (1975), that the decay of the coda becomes stable at sufficiently long lapse-time only. Our calculations suggest that the irregular decay of the intensity in the early coda may be partly ascribed to spatial variation of scattering and absorption in the region under study.

5 CONCLUSION AND OUTLOOK

In this paper, we have used a perturbation approach to establish general formulae relating spatial variations of scattering and absorption properties to the intensity received in the coda. These formulae take the form of spatial integrals of the perturbation weighted by a sensitivity kernel, which depends on the lapse-time in the coda and on the type of perturbation. The perturbations couple the coherent and incoherent parts of the intensity so that the two contribute to the sensitivity of coda waves even at long lapse-time. The kernels

have been calculated in 2-D isotropically scattering media and their singularities have been described in detail. In the case of absorption, the sensitivity is maximum along the direct ray path connecting the source and station and diverges at these two points. We have also shown that a localized perturbation of absorption affects the overall decay of the coda in a manner which depends on the location of the anomaly with respect to the source and station. In the case of scattering, the sensitivity has a much more complex structure. In addition to the divergence at the source and station, the kernel is also singular on the single-scattering ellipse. The singularity is, in fact, double, algebraic and Dirac delta-like. These two terms decay exponentially fast with the lapse-time and become negligible after two to three mean free times. The scattering kernel displays a broad zone of strong negative sensitivity around the direct ray path and is positive elsewhere. Because of this intricate spatial pattern, a localized scattering anomaly has a complex signature in the coda, and may entail a positive or negative variation of intensity depending on the epicentral distance and/or the lapse-time. In general, absorption anomalies have a stronger and longer-lasting effect on the intensity received in the coda than scattering anomalies.

Although the primary focus of this work is the mapping of spatial variations of attenuation properties, the proposed theory may also find applications to the mapping of temporal variations based on the measurement of delay times in the coda. In particular, when the diffusion approximation does not apply and the energy flux is strongly anisotropic, the sensitivity kernels originally proposed to map the relative velocity changes in an evolving medium should be amended (Pacheco & Snieder 2005; Obermann *et al.* 2013). These kernels only depend on the angularly averaged intensity usually calculated in the diffusion approximation. When this approximation is invalid, it is tempting to simply substitute the diffusion solution with the intensity derived from the more accurate radiative transfer equation. However, such a substitution would violate the normalization condition derived by Pacheco & Snieder (2005) (eq. 16). Because the specific intensity can be interpreted as a probability density defined in phase space ($\mathbf{x}, \hat{\mathbf{k}}$), we can straightforwardly extend the probabilistic reasoning of Pacheco & Snieder (2005) and derive a sensitivity kernel for delay times in the coda in terms of the specific intensity. We find that the apparent velocity perturbation in the coda $(\delta v/v)_a$ due to a perturbation of the velocity field $\delta v/v$ in an evolving medium is given by

$$\begin{aligned} \left(\frac{\delta v}{v}\right)_a(\mathbf{r}; \mathbf{r}_0; t) &= S^d \int_{\mathbb{R}^d} \int_{S^d} \int_0^t \frac{\delta v}{v}(\mathbf{r}') \\ &\times \frac{I(\mathbf{r}', -\hat{\mathbf{n}}'; \mathbf{r}; t-t') I(\mathbf{r}', \hat{\mathbf{n}}'; \mathbf{r}_0; t')}{I(\mathbf{r}; \mathbf{r}_0; t)} d\hat{\mathbf{n}}' d\mathbf{r}' dt' \end{aligned} \quad (36)$$

Formula (36) is valid in the case of an anisotropic distribution of energy fluxes and reduces to previously published formulae when the isotropy condition applies. It is apparent that the velocity perturbation kernel is identical to the absorption kernel (11). Both verify the generalized normalization condition (15), which involves an integral over phase space.

Our preliminary calculations of the impact of local attenuation perturbations on the intensity received in the coda suggest that it should be possible to map lateral variations of scattering and absorption in the crust with the aid of sensitivity kernels. Existing Q mapping methods such as those developed by Nishigami (1991) or Xie & Mitchell (1990) make rather strong simplifying assumptions on the sensitivity of coda waves. By taking into account the finer

spatiotemporal details of the kernels derived in this paper, there is hope to improve on the resolution of existing methods and to distinguish between absorption and scattering effects. Our future efforts will concentrate on the development of a tool to map the spatial variations of scattering and absorption in the lithosphere from the intensity of coda waves. In this respect, the variety of inverse methods developed in optical tomography, and summarized in the papers by Arridge & Schotland (2009), can certainly benefit to our work. The problem of inverse transport has also received a lot of attention in the mathematical literature (Bal 2009), and the general principles established in these studies can likewise guide us in our research.

Nevertheless, a number of steps must be taken before we reach our goal. First of all, the limits of validity of the perturbation theory adopted in our work should be established. This question can be addressed with the aid of Monte Carlo simulations to solve the radiative transfer equation in laterally varying scattering and absorbing media. Because the coda displays large statistical fluctuations, another important issue is to develop specific sensitivity kernels for robust observables such as the peak delay time and the coda quality factor. Our approach should ultimately allow us to derive attenuation maps of the crust from the observed regional variations of these two parameters (see, e.g. Carcolé & Sato 2010; Calvet *et al.* 2013). Other important issues should be considered in the future. In particular, scattering anisotropy may play an important role in the observed spatiotemporal dependence of the coda envelope. Because the calculation of the full angular dependence of the specific intensity required for our purposes is still challenging, we have adhered to the simple isotropic scattering approximation which hopefully captures the essential features of the sensitivity. Finally, future works should address the possible role of depth-dependent attenuation structures, which calls for the development of 3-D sensitivity kernels.

ACKNOWLEDGEMENTS

The authors acknowledge a research grant of Électricité de France through the research program SIGMA (Seismic Ground Motion Assessment). This research has also been partially supported by the ALEAS program of INSU-CNRS. The manuscript benefited from the comments of M. Ritzwoller, H. Sato and an anonymous referee.

REFERENCES

- Aki, K. & Chouet, B., 1975. Origin of coda waves: source, attenuation, and scattering effects, *J. geophys. Res.*, **80**(23), 3322–3342.
- Akkermans, E. & Montambaux, G., 2007. *Mesoscopic Physics of Electrons and Photons*, Cambridge Univ. Press.
- Apresyan, L.A. & Kravtsov, Y.A., 1996. *Radiation Transfer: Statistical and Wave Aspects*, Gordon and Breach.
- Arridge, S., 1999. Optical tomography in medical imaging, *Inverse Probl.*, **15**, R41–R93.
- Arridge, S.R., 1995. Photon-measurement density functions. Part I: analytical forms, *Appl. Opt.*, **34**(31), 7395–7409.
- Arridge, S.R. & Schotland, J.C., 2009. Optical tomography: forward and inverse problems, *Inverse Probl.*, **25**(12), 123 010.
- Arridge, S.R., van der Zee, P., Cope, M. & Delpy, D.T., 1991. Reconstruction methods for infrared absorption imaging, in *Proceedings of Society of Photo-Optical Instrumentation Engineers (SPIE) Conference Series*, vol. 1431, pp. 204–215.
- Bal, G., 2009. Inverse transport theory and applications, *Inverse Probl.*, **25**(5), doi:10.1088/0266-5611/25/5/053001.
- Bostock, M. & Rondenay, S., 1999. Migration of scattered teleseismic body waves, *Geophys. J. Int.*, **137**(3), 732–746.
- Calvet, M. & Margerin, L., 2013. Lapse-time dependence of coda Q: anisotropic multiple-scattering models and application to the pyrenees, *Bull. seism. Soc. Am.*, **103**(3), 1993–2010.
- Calvet, M., Sylvander, M., Margerin, L. & Villasenör, A., 2013. Spatial variations of seismic attenuation and heterogeneity in the Pyrenees: coda Q and peak delay time analysis, *Tectonophysics*, **608**, 428–439.
- Carcolé, E. & Sato, H., 2010. Spatial distribution of scattering loss and intrinsic absorption of short-period S waves in the lithosphere of Japan on the basis of the multiple lapse time window analysis of Hi-net data, *Geophys. J. Int.*, **180**(1), 268–290.
- Case, K., 1969. On boundary value problems of linear transport theory, in *Proceedings of the Symposium in Applied Mathematics*, vol. 1, pp. 17–36.
- Chandrasekhar, S., 1960. *Radiative Transfer*, Dover.
- Chazalon, A., Campillo, M., Gibson, R. & Carreno, E., 1993. Crustal wave propagation anomaly across the Pyrenean Range. Comparison between observations and numerical simulations, *Geophys. J. Int.*, **115**(3), 829–838.
- Dorn, O., 1998. A transport-backtransport method for optical tomography, *Inverse Probl.*, **14**, 1107–1130.
- Dorn, O., 2000. Scattering and absorption transport sensitivity functions for optical tomography, *Opt. Express*, **7**(13), 492–506.
- Fehler, M., Hoshihara, M., Sato, H. & Obara, K., 1992. Separation of scattering and intrinsic attenuation for the Kanto-Tokai region, Japan, using measurements of S-wave energy versus hypocentral distance, *Geophys. J. Int.*, **108**(3), 787–800.
- Feng, S. & Sornette, D., 1991. Acoustical nondestructive evaluation of heterogeneous materials in the multiple scattering regime, *Acoust. Soc. Am. J.*, **90**, 1742–1748.
- Gusev, A. & Abubakirov, I., 1999a. Vertical profile of effective turbidity reconstructed from broadening of incoherent body-wave pulses. I. General approach and the inversion procedure, *Geophys. J. Int.*, **136**(2), 295–308.
- Gusev, A. & Abubakirov, I., 1999b. Vertical profile of effective turbidity reconstructed from broadening of incoherent body-wave pulses. II. Application to Kamchatka data, *Geophys. J. Int.*, **136**(2), 309–323.
- Gusev, A.A., 1995. Vertical profile of turbidity and coda Q, *Geophys. J. Int.*, **123**(3), 665–672.
- Hoshihara, M., 1991. Simulation of multiple-scattered coda wave excitation based on the energy conservation law, *Phys. Earth planet. Inter.*, **67**(1), 123–136.
- Hoshihara, M., 1993. Separation of scattering attenuation and intrinsic absorption in Japan using the multiple lapse time window analysis of full seismogram envelope, *J. geophys. Res.*, **98**(B9), 15 809–15 824.
- Jin, A. & Aki, K., 1988. Spatial and temporal correlation between coda Q and seismicity in China, *Bull. seism. Soc. Am.*, **78**(2), 741–769.
- Larose, E., Planès, T., Rossetto, V. & Margerin, L., 2010. Locating a small change in a multiple scattering environment, *Appl. Phys. Lett.*, **96**(20), 204 101-1–204 101-3.
- Margerin, L., 2005. Introduction to radiative transfer of seismic waves, in *Seismic Earth: Array Analysis of Broadband Seismograms*, vol. 157 of Geophysical Monograph Series, pp. 229–252, eds. Levander, A. & Nolet, G., American Geophysical Union.
- Margerin, L., 2013. Diffusion approximation with polarization and resonance effects for the modelling of seismic waves in strongly scattering small-scale media, *Geophys. J. Int.*, **192**(1), 326–345.
- Margerin, L., Campillo, M., Shapiro, N. & Van Tiggelen, B., 1999. Residence time of diffuse waves in the crust as a physical interpretation of coda Q: application to seismograms recorded in Mexico, *Geophys. J. Int.*, **138**(2), 343–352.
- Mitchell, B. & Cong, L., 1998. Lg coda Q and its relation to the structure and evolution of continents: a global perspective, *Pure appl. Geophys.*, **153**, 655–663.
- Mitchell, B.J., 1995. Anelastic structure and evolution of the continental crust and upper mantle from seismic surface wave attenuation, *Rev. Geophys.*, **33**, 441–462.

Nieuwenhuizen, T.M. & van Rossum, M., 1993. Role of a single scatterer in a multiple scattering medium, *Phys. Lett. A*, **177**(1), 102–106.

Nishigami, K., 1991. A new inversion method of coda waveforms to determine spatial distribution of coda scatterers in the crust and uppermost mantle, *Geophys. Res. Lett.*, **18**(12), 2225–2228.

Nishigami, K., 2000. Deep crustal heterogeneity along and around the San Andreas fault system in Central California and its relation to the segmentation, *J. geophys. Res.*, **105**(B4), 7983–7998.

Nolet, G., 2008. *A Breviary of Seismic Tomography*, Cambridge Univ. Press.

Obara, K. & Sato, H., 1995. Regional differences of random inhomogeneities around the volcanic front in the Kanto-Tokai area, Japan, revealed from the broadening of S wave seismogram envelopes, *J. geophys. Res.*, **100**(B2), 2103–2121.

Obermann, A., Planès, T., Larose, E., Sens-Schnfelder, C. & Campillo, M., 2013. Depth sensitivity of coda waves to velocity perturbations in an elastic heterogeneous medium, *Geophys. J. Int.*, **194**, 372–382.

Paasschens, J., 1997. Solution of the time-dependent Boltzmann equation, *Phys. Rev. E*, **56**, 1135–1141.

Pacheco, C. & Snieder, R., 2005. Time-lapse travel time change of multiply scattered acoustic waves, *J. acoust. Soc. Am.*, **118**, 1300–1310.

Park, M. & Odom, R.I., 2005. Propagators and Feynman diagrams for laterally heterogeneous elastic media, *Geophys. J. Int.*, **160**(1), 289–302.

Planès, T., Larose, E., Margerin, L., Rossetto, V. & Sens-Schönfelder, C., 2014. Decorrelation and phase-shift of coda waves induced by local changes: multiple scattering approach and numerical validation, in *Waves in Random and Complex Media*, doi:10.1080/17455030.2014.880821.

Preisendorfer, R.W., 1957. A mathematical foundation for radiative transfer theory, *J. Math. Mech.*, **6**, 685–730.

Rytov, S.M., Kravtsov, Y.A. & Tatarskii, V.I., 1989. *Principles of Statistical Radiophysics. 4. Wave Propagation through Random Media*, Springer.

Ryzhik, L., Papanicolaou, G. & Keller, J.B., 1996. Transport equations for elastic and other waves in random media, *Wave Motion*, **24**(4), 327–370.

Saito, T., Sato, H. & Ohtake, M., 2002. Envelope broadening of spherically outgoing waves in three-dimensional random media having power law spectra, *J. geophys. Res.*, **107**(B5), doi:10.1029/2001JB000264.

Sato, H., 1989. Broadening of seismogram envelopes in the randomly inhomogeneous lithosphere based on the parabolic approximation: Southeastern Honshu, Japan, *J. geophys. Res.*, **94**(B12), 17 735–17 747.

Sato, H., Fehler, M.C. & Maeda, T., 2012. *Seismic Wave Propagation and Scattering in the Heterogeneous Earth*, Springer.

Sens-Schönfelder, C., Margerin, L. & Campillo, M., 2009. Laterally heterogeneous scattering explains Lg blockage in the Pyrenees, *J. geophys. Res.*, **114**, B07309, doi:10.1029/2008JB006107.

Shang, T. & Gao, L., 1988. Transportation theory of multiple scattering and its application to seismic coda waves of impulsive source, *Sci. Sinica*, **31**, 1503–1514.

Singh, S. & Herrmann, R.B., 1983. Regionalization of crustal coda Q in the continental United States, *J. geophys. Res.*, **88**(B1), 527–538.

Snieder, R. & Hagerty, M., 2004. Monitoring change in volcanic interiors using coda wave interferometry: application to Arenal Volcano, Costa Rica, *Geophys. Res. Lett.*, **31**(9), L09608, doi:10.1029/2004GL019670.

Taira, T. & Yomogida, K., 2007. Imaging of crustal heterogeneous structures using a slowness-weighted back-projection with effects of scattering modes: 1. Theory, *J. geophys. Res.*, **112**, B06311, doi:10.1029/2006JB004381.

Taira, T., Yomogida, K., Kuwahara, Y., Imanishi, K. & Ito, H., 2007. Imaging of crustal heterogeneous structures using a slowness-weighted back-projection with effects of scattering modes: 2. Application to the Nagamachi-Rifu fault, Japan, area, *J. geophys. Res.*, **112**, B06312, doi:10.1029/2006JB004382.

Takahashi, T., Sato, H. & Nishimura, T., 2008. Recursive formula for the peak delay time with travel distance in von Kármán type non-uniform random media on the basis of the Markov approximation, *Geophys. J. Int.*, **173**(2), 534–545.

Takahashi, T., Sato, H., Nishimura, T. & Obara, K., 2007. Strong inhomogeneity beneath Quaternary volcanoes revealed from the peak delay analysis of S-wave seismograms of microearthquakes in northeastern Japan, *Geophys. J. Int.*, **168**(1), 90–99.

Takahashi, T., Sato, H., Nishimura, T. & Obara, K., 2009. Tomographic inversion of the peak delay times to reveal random velocity fluctuations in the lithosphere: method and application to northeastern Japan, *Geophys. J. Int.*, **178**(3), 1437–1455.

Takahashi, T., Obara, K., Kodaira, S., Suetsugu, D., Takahashi, N., Kamiya, S. & Tamura, Y., 2011. Random inhomogeneities in the northern Izu-Bonin arc estimated by tomographic inversion of peak delay times of S wave seismograms, *J. geophys. Res.*, **116**, B03303, doi:10.1029/2010JB007691.

van Rossum, M. & Nieuwenhuizen, T.M., 1999. Multiple scattering of classical waves: microscopy, mesoscopy, and diffusion, *Rev. Modern Phys.*, **71**, 313–371.

Wegler, U., 2004. Diffusion of seismic waves in a thick layer: theory and application to Vesuvius volcano, *J. geophys. Res.*, **109**(B7), B07303, doi:10.1029/2004JB003048.

Wegler, U. & Lühr, B.-G., 2001. Scattering behaviour at Merapi volcano (Java) revealed from an active seismic experiment, *Geophys. J. Int.*, **145**(3), 579–592.

Xie, J. & Mitchell, B., 1990. A back-projection method for imaging large-scale lateral variations of lg coda q with application to continental africa, *Geophys. J. Int.*, **100**(2), 161–181.

Xie, J. & Nuttli, O., 1988. Interpretation of high-frequency coda at large distances: stochastic modelling and method of inversion, *Geophys. J.*, **95**(3), 579–595.

APPENDIX A: DIFFUSION APPROXIMATION

The purpose of this appendix is to provide an independent derivation of eqs (20) and (21) using a diffusion model for the propagation of energy in the Earth. Such an approximation may be valid if the propagation time and distances are much larger than the mean free time and mean free path, respectively, and if the medium perturbations are not located in the vicinity of the source. In seismology, this model has widely been used to model the propagation of seismic energy in volcanic areas (Wegler & Lühr 2001; Snieder & Hagerty 2004; Wegler 2004). Detailed derivations have been previously published in the context of optical tomography (Arridge 1995); hence, we shall be brief. The diffusion equation for the total intensity in a laterally varying scattering and absorbing medium writes:

$$\frac{\partial I(\mathbf{r}, t)}{\partial t} - \nabla \cdot (D(\mathbf{r})\nabla I(\mathbf{r}, t)) - \frac{I(\mathbf{r}, t)}{t^a(\mathbf{r})} = S(\mathbf{r}, t). \quad (\text{A1})$$

In eq. (A1), we have introduced the diffusion constant of the waves D , which is related to the mean free time of the waves, the mean cosine of the scattering angle g (see eq. 22) and the wave velocity c through the formula:

$$D(\mathbf{r}) = \frac{c\tau(\mathbf{r})^2}{(1-g)d}. \quad (\text{A2})$$

Like in eq. (1), t^a and S denote the absorption time and source of intensity, respectively. The treatment that follows parallels closely the perturbation approach for the radiative transfer equation. We define the Green's function of the diffusion equation $G(\mathbf{r}; \mathbf{r}_0, t)$ as the solution to eq. (A1) with source term $S(\mathbf{r}, t) = \delta(\mathbf{r} - \mathbf{r}_0)\delta(t)$. This Green's function may be used to solve the diffusion equation for a general source term $S(\mathbf{r}, t)$. If the intensity is initially 0, the solution is given by the convolution integral:

$$I(\mathbf{r}, t) = \iint_0^t G(\mathbf{r}; \mathbf{r}_0, t - t')S(\mathbf{r}_0, t') d\mathbf{r}_0 dt', \quad (\text{A3})$$

where the spatial integral is over the full space. Following the perturbative approach, we assume that the diffusion constant and absorption time may be decomposed as follows:

$$D(\mathbf{r}) = D_0 + \delta D(\mathbf{r}), \quad (\text{A4a})$$

$$\frac{1}{t^a(\mathbf{r})} = \frac{1}{t_0^a} + \delta \left(\frac{1}{t^a(\mathbf{r})} \right), \quad (\text{A4b})$$

where the deviations from homogeneity are supposed to be sufficiently small. Introducing the decomposition (A4) into eq. (A1), transferring all perturbative terms to the right-hand side, and applying the representation theorem (A3), we obtain the following integral equation for the Green's function G :

$$\begin{aligned} G(\mathbf{r}, \mathbf{r}_0; t) &= G_0(\mathbf{r}, \mathbf{r}_0; t) - \iint_0^t G_0(\mathbf{r}, \mathbf{r}_1; t - t') \\ &\quad \times \delta \left(\frac{1}{t^a(\mathbf{r}_1)} \right) G(\mathbf{r}_1, \mathbf{r}_0; t') d\mathbf{r}_1 dt' \\ &\quad + \iint_0^t G_0(\mathbf{r}, \mathbf{r}_1; t - t') \nabla_1 \cdot (\delta D(\mathbf{r}_1) \nabla_1 G(\mathbf{r}_1, \mathbf{r}_0; t')) \\ &\quad \times d\mathbf{r}_1 dt'. \end{aligned} \quad (\text{A5})$$

We now assume that the perturbations are sufficiently small so that G may be substituted with G_0 in eq. (A5). Integrating by parts the second term on the right-hand side, the perturbation of intensity in the diffusion approximation may be written as

$$\begin{aligned} \delta I(\mathbf{r}; \mathbf{r}_0, t) &= \int \delta \left(\frac{1}{t^a(\mathbf{r}_1)} \right) K_d^a(\mathbf{r}; \mathbf{r}_1; \mathbf{r}_0, t) d\mathbf{r}_1 \\ &\quad + \int \delta D(\mathbf{r}_1) K_d^{\text{sc}}(\mathbf{r}; \mathbf{r}_1; \mathbf{r}_0, t) d\mathbf{r}_1, \end{aligned} \quad (\text{A6})$$

where the following sensitivity kernels have been introduced:

$$K_d^a(\mathbf{r}; \mathbf{r}_1; \mathbf{r}_0, t) = \int_0^t G_0(\mathbf{r}, \mathbf{r}_1; t - t') G_0(\mathbf{r}_1, \mathbf{r}_0; t') dt', \quad (\text{A7})$$

$$K_d^{\text{sc}}(\mathbf{r}; \mathbf{r}_1; \mathbf{r}_0, t) = - \int_0^t \nabla_1 G_0(\mathbf{r}, \mathbf{r}_1; t - t') \cdot \nabla_1 G_0(\mathbf{r}_1, \mathbf{r}_0; t') dt'. \quad (\text{A8})$$

In eqs (A7)–(A8), the subscript reminds the reader that the results are obtained in the diffusion approximation. The agreement between eqs (20) and (A7) is clear, once one realizes that I and G both stand for the total intensity radiated by a unit point source of intensity. To verify that eqs (21) and (A8) agree, we first note that in the diffusion approximation, the current vector and the intensity are related by Fourier's law (e.g. Akkermans & Montambaux 2007):

$$\nabla_1 G_0(\mathbf{r}_1; \mathbf{r}_0; t) = - \frac{c}{D_0} \mathbf{J}_0(\mathbf{r}_1; \mathbf{r}_0, t), \quad (\text{A9})$$

Next, under the assumption of constant wave velocity and scattering anisotropy, we note the following relation between perturbations of the mean free time and diffusion constant:

$$-c^2 \frac{\delta D}{D^2} = c^2 \delta \left(\frac{1}{D} \right) = d(1 - g) \delta \left(\frac{1}{\tau} \right). \quad (\text{A10})$$

Injecting eq. (A9) into eq. (A8) and taking into account the relation (A10), the asymptotic relation (21) is recovered.

APPENDIX B: CALCULATION OF ANGULAR INTEGRALS

In this section, we provide analytical formulae for the angular integrals which appear in eq. (31). We wish to evaluate:

$$I = \frac{1}{2\pi} \int_{2\pi} \frac{d\hat{\mathbf{s}}}{(\bar{t} - \overline{SR\hat{\mathbf{S}}\hat{\mathbf{R}} \cdot \hat{\mathbf{s}}})(\bar{u} - \hat{\mathbf{R}}_0 \cdot \hat{\mathbf{s}})}. \quad (\text{B1})$$

Introducing the new variable $\bar{v} = \bar{t}/\overline{SR}$, eq. (B1) can be rewritten as

$$\begin{aligned} I &= \frac{1}{2\pi \overline{SR}} \\ &\quad \times \int_0^{2\pi} \frac{d\theta}{(\bar{v} - \cos\theta_1 \cos\theta - \sin\theta_1 \sin\theta)(\bar{u} - \cos\theta_0 \cos\theta - \sin\theta_0 \sin\theta)}, \end{aligned} \quad (\text{B2})$$

where $\hat{\mathbf{s}} = (\cos\theta, \sin\theta)$, $\hat{\mathbf{R}}_0 = (\cos\theta_0, \sin\theta_0)$ and $\hat{\mathbf{S}}\hat{\mathbf{R}} = (\cos\theta_1, \sin\theta_1)$ in a Cartesian system of coordinate such as the one shown in Fig. 1 (note that $\theta_1 = 0$ in this case). Introducing the complex numbers $z = e^{i\theta}$, $z_1 = e^{i\theta_1}$ and $z_0 = e^{i\theta_0}$, we rewrite eq. (B1) as a contour integral in the complex plane over the unit circle:

$$\begin{aligned} I &= \frac{1}{i2\pi \overline{SR}z} \\ &\quad \times \oint_{|z|=1} \frac{dz}{(\bar{v} - (z_1 + 1/z_1)(z + 1/z)/4 + (z_1 - 1/z_1)(z - 1/z)/4)(\bar{u} - \dots)}, \end{aligned} \quad (\text{B3})$$

where the dots indicate that one obtains the terms inside the second parenthesis from the first by substitution ($z_1 \rightarrow z_0$). In eq. (B2), the integrand has four poles in the complex plane:

$$r_{0\pm} = (\bar{u} \pm \sqrt{\bar{u}^2 - 1})z_0, \quad (\text{B4})$$

$$r_{1\pm} = (\bar{v} \pm \sqrt{\bar{v}^2 - 1})z_1. \quad (\text{B5})$$

One easily checks that only r_{0-} and r_{1-} lie inside the contour. Application of the residue theorem then yields:

$$\begin{aligned} I &= \frac{4z_1z_0}{\overline{SR}(r_{1-} - r_{0-})} \left(\frac{r_{1-}}{(r_{1-} - r_{1+})(r_{1-} - r_{0+})} \right. \\ &\quad \left. - \frac{r_{0-}}{(r_{0-} - r_{1+})(r_{0-} - r_{0+})} \right). \end{aligned} \quad (\text{B6})$$

In the case where the two poles coalesce, the limit is given by

$$I = \frac{4z_1^2(r_{1-} + r_{1+})}{(r_{1+} - r_{1-})^3}. \quad (\text{B7})$$



Date: 26 May 2014

Review on the report:

« Spatial variations of seismic attenuation in metropolitan France from observation and modeling of the seismic coda »

By J. Mayor, L. Margerin and M. Calvet

Review by Thierry Camelbeeck

The purpose of this note is to briefly review the report by J. Mayor, L. Margerin and M. Calvet on the PhD-work supported by SIGMA and dedicated to the evaluation of the seismic attenuation spatial variations in France from the observation and modeling of the seismic coda of local and near earthquakes.

Studying the absorption and scattering quality factors and evaluating their regional variations is important in the understanding of the degradation of shear wave elastic field from the seismic source to the surrounding crustal structures. As such, it provides information to better assess earthquake source characteristics and to model ground motion from the elastodynamic equation. This is a very interesting project and the presented results are promising.

METHODOLOGIES

The work is based on classical theories of coda waves, including the most recent works. Its promoters and their research group are leading specialist in this field of investigation. In a large sense, there is no doubt about the high quality of the work even if some questions stay open and some part of the work should be better explained.

(1) As it is explained (see also Figure 2) in the text, Q_c depends more on scattering-Q and anisotropy for short lapse time and intrinsic-Q dominates for long lapse time due to the fact that the coda evolves with time from a single scattering to a multiple scattering and finally a diffusive regime. Clearly, the choice of the studied part of the coda suggests that this work intends to evaluate intrinsic-Q.

Q1: In figure 12, the long lapse time plateau in the 4-8 Hz frequency band for the considered dataset is identified when $L_w(s)$ is greater than 70 s and a coda onset of 50 s. The way to estimate the plateau Q-value is considered as independent of the frequency in the text. For the reader to assess the validity of this assumption, it would be interesting to know if the observation is similar in the three other considered frequency ranges.

Q2: The explanations given from figure 13 to evaluate the maximal epicentral giving the best compromise to measure Q_c with these defined $L_w(s)$ and t_w are not very clear from the document. How can we see that 180 km is this critical distance with a plot reporting the distances only up to 200 km? Is there any statistical analysis supporting this conclusion? What about the distances of less than 50 – 60 km?

(2) The wave field generated by a seismic source results from the convolution of different effects, including source, path and site contributions. The seismic coda includes contribution from these different effects, but the study only considered the path

properties without explaining how the possible influence of the other contributions can affect the Q_c evaluation.

Q1: Concerning the source contribution, it is important to have in mind that few earthquakes in the dataset [see my comment on the data presentation] have a corner frequency between 1 and 2 Hz, and even 2 and 4 Hz. How did you test if the energetic content of the source in the studied time series is sufficiently large to evaluate Q_c at those “low” frequencies? Was the test (2) page 20 on the S/N ratio done by frequency range or not?

Q2: The local geological conditions of the recording stations can have a strong influence on the coda signal in some frequency bands. This effect certainly contributes to the observed variation of ± 200 in Q_c in the Alps. To validate the presented regional Q_c variations, I recommend evaluating the influence of these local soil conditions, at least for a few stations with specific soil characteristics.

- (3) Concerning the evaluation of Q_c from the recordings, I noted the large uncertainties reported on figures 5 and 6 for some of the spectral ratios and also the fact that the Q power law is determined from a least square fit of the frequency dependent amplitude spectral ratios.

Q1: Did you consider these largely uncertain values in the fit?

- (4) In the mapping, you considered squares of 50 km x 50 km and supposed that the Q_c coda represents the value along the direct ray path between the source and the station. The validity of the approach is confirmed by the very interesting sensitivity study done in paragraph 4.

Q1: It is difficult from the document to evaluate the variability of Q , because there is no discussion on the way uncertainties can be evaluated for the different pixels. It would be interesting to present some examples from the Q distribution in different pixels.

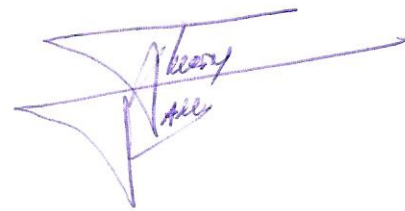
Q2: Do you think that retaining the pixels with only 4 ray paths (page 22) is sufficient to obtain a confident Q_c value, and with what uncertainty? Enlarging the dimension of the pixels could probably enhance the quality of the evaluation. What is the criteria adopted to choose the 50 km x 50 km dimension?

PRESENTATION OF THE DATA

There is a lack of information about the dataset. The document should at least include diagrams reporting the range of magnitudes and focal depths of the studied earthquakes and the number of recordings by range of epicentral distance in each range of magnitude [3-4, 4-5 and >5].

Additional comments:

- Figure 12: discrepancy between the text in the legend and in the figure: $t_w=30$ s and 50 s?
- Figure 13: L_w should also be indicated in the figure.



Review of the SIGMA Deliverable D2.113

"Spatial variations of seismic attenuation in metropolitan France from observation and modeling of the seismic coda"

(Authors : J. Mayor, L. Margerin & M. Calvet, 06/05/2014)

I apologize for the extreme delay in sending this review.

As indicated in the title, the time decay of coda waves is used to provide quantitative characteristics of crustal attenuation in different frequency bands, and analyze their spatial variations at the smallest possible scale. There is a focus on SouthEastern France, but the used data set allows to extend the results to a broader area, from Pyrénées and Massif Central to the West, Rhine graben to the North, Po Plain and even Eastern Alps to the East, and northern Appennines to the South-East.

The report starts with a discussion of the two main origins of attenuation of seismic wave amplitude (intrinsic and scattering, quantified through quality factors Q_i and Q_{sc}) and their respective influence of the early and late coda. The second section presents three various techniques proposed in the literature to derive a frequency-dependent quality factor " Q_{coda} " (i.e. a mixture of Q_i and Q_{sc}) and selects one of them on the basis of a comparison test on 4 alpine seismograms. The third section then applies the selected one on a data set allowing to analyze the spatial variations of Q_c in SE France and surroundings, which are found to be significant at a typical scale of 100 km; it also includes a short review of previous studies, and a parameter study to justify the choice of the optimal coda windows. Finally, the last section sets the theoretical background (radiative transfer equation) in 2 dimensions to derive the spatial variations of Q_i and Q_{sc} from those of Q_{coda} through the use of (2D) "sensitivity kernels" for absorption and scattering, respectively; this however requires a spatio-temporal analysis of the energy in the coda, which is yet to be done. The conclusion summarizes the main findings and presents the next work, including the improvement / increase of the data set (new stations, broader frequency range towards higher frequencies) and investigations on the lapse time dependency of Q_{coda} , and new theoretical developments to recover Q_i and Q_{sc} from the lapse time dependence of Q_{coda} , with due accounting of possible perturbations such as scattering anisotropy. The main report is complemented by three appendixes, with two conference presentations (poster and abstract), and a recently published paper detailing the theoretical developments of section 4.

All this corresponds to a very good and careful work, with very solid theoretical background. The report is clearly written and easy to follow. I have no basic criticism – especially as I personally know much less about coda waves and background theory than the authors !

I only have a few questions about the data and the end use of such investigations:

Data set

The waveforms used for this report (p.19-20) are a mixture of short period recordings (RENASS and SISMALP), accelerometric recordings (RAP) and ORFEUS broadband recordings from Belgium, Germany, Switzerland, Austria, Slovenia and Italy (+ very few from France), with epicentral distance less than 200 km. The corresponding total set of 88000 waveforms was decreased to 41000 waveforms with criteria based predominantly on record and coda durations.

It would be interesting to be shown the dispatching of these selected waveforms amongst the various kinds of networks. In particular, how many accelerometric recordings could be used, and did this proportion increase when the RAP network was progressively shifted from trigger to continuous recording. Are there some recommendations for RESIF to optimize the use of coda information ?

Frequency dependence of Q_{coda}

The technique selected to derive Q_{coda} in various frequency bands does not rely on any a priori assumption on the frequency dependence of Q . Do the available results (4 frequency bands) support the "classical" power law type $Q(f) = Q_0 f^\alpha$, and could the planned investigations on broader frequency ranges regionalize Q_0 and α : apparently, from Figure 14 p.23, northern French Alps have low Q at 1-2 Hz, and high Q at 8-16 Hz (comparatively to surrounding areas), which suggest a larger α : is it true or just a matter of color code ? Do the authors expect similar frequency dependence for Q_i and Q_{sc} ?

End use of these results

It is mentioned in the executive summary that these results will be helpful for ground motion prediction, from delimitation of source zones to GMPEs and stochastic models.

How could the spatial variations of Q_{coda} (and later Q_i and Q_{sc}) be introduced in GMPEs, especially as most of the GMPEs presently considered in PSHA studies fro SE France are not based on local data ?

Their use in stochastic models seem more straightforward, at least within relatively short epicentral distances, but requires to specifically tune the stochastic models at a "subregional" scale of 50-100. Would this be easy to implement in present PSHA codes ? And what would be the strategy for intermediate distances (50 – 200 km) – which however are not so important for strong shaking in metropolitan France - ? Last, could these Q_{coda} estimates significantly affect the estimates of moment magnitude and stress drops, to be also included in stochastic models ?

Miscellaneous

Equation (12) p. 14 : could there be an error with mixing of indexes " $i + 1$ " for τ and " $i + Nr$ " for $\langle A \rangle$?

Cadarache, 04/06/2014

Pierre-Yves BARD